EXPERIMENTAL EXPLORATION OF THE MICROBIOME IN THE INTERVERTEBRAL DISC

Andrea Nüesch

A thesis submitted in fulfilment of the requirements of University of Sheffield for the degree of Doctor of Philosophy.

Clinical Medicine, School of Medicine, and Population Health

Medical School

The University of Sheffield

2024

DEDICATION

Für mis Omi.

ACKNOWLEDGEMENTS

I would like to extend my heartfelt thanks to everyone who has supported me throughout my PhD journey. My deepest gratitude goes to Christine for her dedication to spine research, her vast knowledge, and the passion she has always shared. Her encouragement and unwavering support throughout this thesis have been invaluable. To Mel, who offered constant encouragement and helped me blend my scientific work with art, making this experience even more meaningful—thank you.

I am also grateful to Disc4All and everyone involved in the project for making this journey special and giving me the opportunity to pursue a PhD within such a dynamic consortium. My sincere thanks to Joseph and Grace for the coffee breaks and support in the lab, and to Muna for being there for both coffee and panic talks. Special thanks to Lucy for the dance battles and hugs that brightened my days, and to Hector for being like a brother away from home. To Bobo, the kindest and most helpful colleague, your support has been a true blessing.

To Katherine, Paola, and Mapo, thank you for the phone calls, school breakfasts, and your steady support. Roger, your thoughtful conversations and unforgettable raves have added richness to this journey. I am also grateful for the friendship of Mic, Alina, Annina, Sufi, Romy, and Teresa whose presence brought so much joy and laughter as well as encouragement when things went wrong.

My thanks to Claudia for her scientific guidance and emotional support, both of which have been invaluable. I am endlessly grateful to my parents for their unwavering belief in my education, and to my siblings Martina, Reto, Mark, and Flurin for always being there. Finally, to Dorothy, my family away from home, thank you for the movie nights and wine, helping me unwind when I needed it most.

To each of you, thank you for making this work possible through your kindness, support, and friendship.

ABSTRACT

The intervertebral disc (IVD) is traditionally viewed as an aseptic structure due to its avascular nature, yet recent studies challenge this assumption, revealing possible bacterial colonisation within disc tissue. This discovery has spurred great interest in understanding the role of bacteria, such as *Cutibacterium acnes*, in IVD degeneration and related pathologies. This thesis investigated the presence and role of bacteria in IVD tissue, distinguishing between perioperative contamination and true *in vivo* bacterial colonisation. The introduction summarises existing literature suggesting a microbiome within the IVD and highlights the need for further exploration into bacterial colonisation. A semi-automatic quantification method was developed for analysing immunohistochemically stained low-cellularity tissues to enhance accuracy and inter-rater reliability. Immunohistochemical evidence presented in this thesis confirmed the presence of *C. acnes* and *Staphylococcus aureus* in IVD tissue, with significant correlations identified between *C. acnes* and nucleotide-binding oligomerisation domain 2 (NOD2), matrix metallo-proteinase 3 (MMP3), and gasdermin-D (GSDMD). Experimental inhibition studies suggested that toll-like receptors may not be the primary receptors involved in bacterial recognition, indicating that other pattern recognition receptors, such as nucleotide-binding oligomerisation domain-like receptors 3 (NLRP3), may play a key role.

Further results demonstrated that both human and bovine IVDs harbour bacteria, with regional distribution differences noted within the bovine discs. The findings support the hypothesis that bacterial invasion may occur through the endplates and annulus fibrosus. Additionally, the impact of the microbiome on Modic changes and disc degeneration is discussed, highlighting the complex interplay between bacterial presence and disc pathology. The thesis emphasises the need for more targeted research into the disc microbiome and its implications for treatment approaches, particularly regarding the cautious use of antibiotics, which may disrupt beneficial microbial communities. Overall, this thesis provides compelling evidence for the presence of a disc microbiome and underscores the need for further investigation into its role in disc health and disease.

Contents

LIST OF FIGURES

LIST OF TABLES

LIST OF APPENDICES

ABBREVIATIONS

AA	L-Ascorbic Acid 2-Phosphate
ABC	Avidin-Biotin-Complex
ADAMTS	A Disintegrin and Metalloproteinase with Thrombospondin Motifs
AF	Annulus Fibrosus
AIM-2	Absent in Melanoma-2
ALR	Absent in Melanoma-2-Like Receptor
AP-1	Activator Protein-1
BIF	Bio-Format Image File
BNB	Blood-NP Barrier
BSA	Bovine Serum Albumin
CCL17	C-C Motif Chemokine Ligand 17
CCL19	C-C Motif Chemokine Ligand 19
CCL2	C-C Motif Chemokine Ligand 2
CCL20	C-C Motif Chemokine Ligand 20
CCL22	C-C Motif Chemokine Ligand 22
CCL3	C-C Motif Chemokine Ligand 3
CCL4	C-C Motif Chemokine Ligand 4
CCL7	C-C Motif Chemokine Ligand 7
CFU	Colony Forming Unit
CLR	C-type Lectin Receptors
CNTF	Ciliary Neurotrophic Factor
CPU	Central Processing Unit
CSF	Colony Stimulating Factor
CTACK	C-C Motif Chemokine Ligand 27
CXCL	C-X-C Motif
CXCL11	C-X-C Motif Chemokine Ligand 11
CXCL12	C-X-C Motif Chemokine Ligand 12
CXCL13	C-X-C Motif Chemokine Ligand 13
CXCL16	C-X-C Motif Chemokine Ligand 16
CXCL9	C-X-C Motif Chemokine Ligand 9
CZI	Carl Zeiss Image
DEFB	Defensin Beta
DMEM	Dulbecco’s Modified Eagle Medium

DNA	Deoxyribonucleic Acid
EDTA	Ethylendiaminetertraacetid Acid
Eotaxin	C-C Motif Chemokine Ligand 11
ERK	Extracellular Signal-Regulated Kinase
FCS	Foetal Calf Serum
FGF	Fibroblast Growth Factor
FGF Basic	Fibroblast Growth Factor 2
FST	Follistatin
G-CSF	Colony Stimulation Factor 3
GM-CSF	Colony Stimulation Factor 2
GROA	C-X-C Motif Chemokine Ligand 1
GSDMD	Gasdermin-D
H-DAB	Haematoxylin-DAB
HG	High Glucose
HG-DMEM	High Glucose Dulbecco's Modified Eagle Medium
iAF	Inner Annulus Fibrosus
ICAM	Intercellular Adhesion Molecule
ICAM1	Intercellular Adhesion Molecule 1
ICC	Intraclass Correlation Coefficient
IHC	Immunohistochemistry
IL-10	Interleukin 10
IL-11	Interleukin 11
IL-12	Interleukin 12
IL-13	Interleukin 13
IL-15	Interleukin 15
IL-16	Interleukin 16
IL-17A	Interleukin 17A
IL-17F	Interleukin 17F
IL-18	Interleukin 18
IL-19	Interleukin 19
IL-1A	Interleukin 1A
IL-1B	Interleukin 1B
IL-1Ra	Interleukin 1RA
IL-20	Interleukin 20
IL-22	Interleukin 22

IL-2Ra	Interleukin 2RA
IL4	Interleukin 4
IL5	Interleukin 5
IL6	Interleukin 6
IL7	Interleukin 7
IL8	Interleukin 8
IL9	Interleukin 9
IMS	Industrial Methylated Spirt
IP10	C-X-C Motif Chemokine Ligand 10
ITS-x	Insulin Transferrin Selenium-x
IVD	Intervertebral Disc
JNK	c-Jun-N-terminal Kinase
LBP	Low Back Pain
LG	Low Glucose
LIF	LIF Interleukin 6 Family Cytokine
LPS	Lipopolysaccharide
LTA	Lipoteichoic Acid
M-CSF	Colony Stimulating Factor 1
MDP	Muramyl Dipeptide
MIF	Macrophage Migration Inhibitory Factor
MMP	Matrix Metalloproteinase
MMP1	Matrix Metallopeptidase 1
MMP13	Matrix Metallopeptidase 13
MMP2	Matrix Metallopeptidase 2
MMP7	Matrix Metallopeptidase 7
MMP9	Matrix Metallopeptidase 9
MOI	Multiplicity of Infection
MRXS	Mirax Scan
MyD88	Myeloid Differentiation Primary Response Protein 88
NDPI	Nano Zoomer Digital Pathology Image
NFkB	Nuclear Factor Kappa B
NGF	Neural Growth Factor
NLR	Nucleotide-Binding Oligomerisation Domain-Like Receptors
NLRC4	NLR Family CARD Domain-Containing 4
NLRP3	NLR Family Pyrin Domain-Containing 3

NOD	Nucleotide-Binding Oligomerisation Domain
NP	Nucleus Pulposus
NRG1	Neuregulin 1
oAF	Outer Annulus Fibrosus
P/S	Penicillin/ Streptomycin
p38 MAPK	p38 Mitogen-Activated Protein Kinase
PAI1	Serpin Family E Member 1
PBS	Phosphate Buffer Saline
PGN	Peptidoglycan
PROK1	Prokineticin1
PRR	Pattern Recognition Receptor
RAM	Random-Access Memory
RANTES	C-C Motif Chemokine Ligand 5
RETN	Resistin
RGB	Red-Green-Blue
RIG-I	Retinoic Acid-Inducible Gene-I
RLR	Retinoic Acid-Inducible Gene-I-Like Receptor
S100AB	S100 calcium-binding protein A8
SCF	Stem Cell Factor
SCF	Stem Cell Factor
sRANK-L	Receptor Activator of NF-kB
ST2	Suppression Of Tumorigenicity 2
T1WI	T1-Weighted Imaging
T2WI	T2-Weighted Imaging
TBS	Tris-Buffer Saline
TGFb	Transforming Growth Factor Beta1
TIMP1	TIMP Metallopeptidase Inhibitor 2
TIR	Toll/Interleukin-1 Receptor
TLR	Toll Like Receptor
TNF	Tumour Necrosis Factor
TNF10	Tumour Necrosis Factor Member 10
TNFRF9	TNF Receptor superfamily member 9
TRIF	Toll/Interleukin-1 Receptor Domain-Containing Adaptor Inducing Interferon-β
TWEAK	TNF Superfamily Member 12

VCAM1	Vascular Cell Adhesion Molecule 1
VEGF	Vascular Endothelial Growth Factor A

DISSEMINATION: SCIENTIFIC PUBLICATION

PUBLISHED

Bermudez-Lekerika P, Crump KB, Tseranidou S, **Nüesch A**, Kanelis E, Alminnawi A, Baumgartner L, Muñoz-Moya E, Compte R, Gualdi F, Alexopoulos LG, Geris L, Wuertz-Kozak K, Le Maitre CL, Noailly J, Gantenbein B.' IMMUNO-MODULATORY EFFECTS OF INTERVERTEBRAL DISC CELLS'. Front Cell Dev Biol. 2022 Jun 29;10:924692. doi: 10.3389/fcell.2022.924692. PMID: 35846355; PMCID: PMC9277224.

Crump KB, Alminnawi A, Bermudez-Lekerika P, Compte R, Gualdi F, McSweeney T, Muñoz-Moya E, **Nüesch A**, Geris L, Dudli S, Karppinen J, Noailly J, Le Maitre CL, Gantenbein B. 'CARTILAGINOUS ENDPLATES: A COMPREHENSIVE REVIEW ON A NEGLECTED STRUCTURE IN INTERVERTEBRAL DISC RESEARCH'. JOR Spine. 2023 Oct 21;6(4):e1294. doi: 10.1002/jsp2.1294. PMID: 38156054; PMCID: PMC10751983.

Megnis T, Bernhard L, **Nüesch A**, Heggli I, Herger N, Devan J, Marcus R, Laux CJ, Brunner F, Farshad M, Distler O, Le Maitre CL, Dudli S. 'EXPRESSION OF TOLL-LIKE RECEPTORS IN CARTILAGE ENDPLATE CELLS: A ROLE OF TOLL LIKE RECEPTOR 2 IN PRO-INFLAMMATORY AND CATABOLIC GENE EXPRESSION' Cells. 2024 Aug 23;13(17):1402. doi: 10.3390/cells13171402. PMID: 39272974; PMCID: PMC11394474.

SUBMITTED

14-Oct-2024, JOR Spine

Nüesch A*, Ferri MP*, Le Matire CL. 'APPLICATION AND VALIDATION OF SEMI-AUTOMATIC QUANTIFICATION OF IMMUNOHISTOCHEMICALLY STAINED SLIDES FOR LOW CELLULAR TISSUE SUCH AS INTERVERTEBRAL DISC USING QUPATH'

*Authors contributed equally

IN PREPARATION

Nüesch A, Kanelis E, Alexopoulos LG, Gantebein B, Lacey M, Le Maitre CL. 'INTRACELLULAR DETECTION OF *C. ACNES* AND *S. AUREUS* IN NON-HERNIATED HUMAN INTERVERTEBRAL DISCS: IMPLICATIONS FOR CATABOLIC SIGNALLING PATHWAYS'

DISSEMINATION: CONFERENCE ABSTRACTS

PODIUM PRESENTATIONS

Society of Back Pain Research, Warwick, UK, 30th June- 7th July 2022. 'GRAM POSITIVE BACTERIA ARE INTERNALIZED BY DISC CELLS: WHAT IS THEIR INFLUENCE?'

International Combined Orthopaedic Research Society, Edinburgh, UK. 7th-9th September 2022. 'INTERVERTEBRAL DISC CELLS *IN VIVO* INTERNALIZE GRAM POSITIVE BACTERIA: IMPLICATIONS FOR INTERVERTEBRAL DISC DEGENERATION.'

Orthopaedic Research Society, The Philadelphia Spine Research Society, Philadelphia, USA. 6th-10th November 2022. 'GRAM POSITIVE BACTERIA WITHIN THE DISC AND THEIR POTENTIAL INFLUENCE ON NUCLEUS PULPOSUS CELLS'

Britspine, Glasgow, UK, 18th-20th April 2023. 'GRAM POSITIVE BACTERIA ARE PRESENT WITHIN NON-HERNIATED HUMAN DISCS; WHAT IS THEIR INFLUENCE?'

The International Society for the Study of the Lumbar Spine, Milano, Italy, 27th -31st May, 2024 'CUTIBACTERIUM ACNES IS PRESENT IN NON-HERNIATED HUMAN DISCS; ITS POSITIVITY RATE CORRELATES WITH THE PATIENT'S AGE'

Society of Back Pain Research, Aberdeen, UK, 30th June- 7th July 2024. 'GRAM POSITIVE BACTERIA WITHIN THE INTERVERTEBRAL DISC AND THEIR POTENTIAL INFLUENCE'

PGR Symposium, University of Sheffield, Sheffield, 04 July 2024. 'THE EXPERIMENTAL EXPLORATION OF THE MICROBIOME IN DEGERENATED INTERVERTEBRAL DISCS'

INVITED SPEAKER

The human digital twin summer school Barcelona, Barcelona Spain, 3rd-7th of June 2024 'THE EXPERIMENTAL EXPLORATION OF THE MICROBIOME IN THE INTERVERTEBRAL DISC'

POSTER PRESENTATIONS

Mellanby Centre Research Day, University of Sheffield, Sheffield, 25th March 2022, 'ARE THERE BACTERIA FOUND WITHIN THE DISC AND WHAT IS THEIR POTENTIAL INFLUENCE?'

Mellanby Centre Research Day, University of Sheffield, Sheffield, 24th of March 2023, '*C. ACNES* IS PRESENT IN HUMAN INTERVERTEBRAL DISCS; WHAT IS THEIR PITENTIAL INFLUENCE'

POSTERS

Virtual Physiological Human (VPH) Summer school, Barcelona, Spain, 23rd-27th May 2022. 'BACTERIA IN THE INTERVERTEBRAL DISC: WHAT IS THEIR INFLUENCE ON HUMAN NUCLEUS PULPOSUS CELLS?'

European Cells and Materials (eCM) Conference, AO Research Institute, Davos, Switzerland, 15th-18th June 2022. 'INTERVERTEBRAL DISC CELLS IN VIVO INTERNALIZE BACTERIA: WHAT IS THEIR POTENTIAL INFLUENCE**?**'

AWARDS

POSTER AWARDS

Virtual Physiological Human (VPH) Summer school, Barcelona, Spain, 5th – 9th June 2023. **'**THE PRESENCE OF GRAM-POSITIVE BACTERIA WITHIN INTERVERTEBRAL DISC TISSUE AND THEIR POTENTIAL INFLUENCE'

BEST ORAL PRESENTATION

Mellanby Centre Research Day, University of Sheffield, Sheffield, UK, 15th March 2024. 'CUTIBACTERIUM ACNES IS PRESENT IN NON-HERNIATED HUMAN DISCS'

ARI Orthopaedic 2024 Orthopaedic Infection, Davos, Switzerland, 24th-26th June 2024 'EXPLORING GRAM-POSITIVE BACTERIA WITHIN THE INTERVERTEBRAL DISC: WHAT IS THEIR POTENTIAL INFLUENCE?'

CHAPTER 1

INTRODUCTION

INTRODUCTION

AUTHOR CONTRIBUTIONS

I have written the paragraphs for the introduction and have created the figures included unless stated differently. The paragraph 'cross-talk between the immune system and IVD' was previously written by myself together with Christine Le Maitre for the review article: Immuno-Modulatory Effects of Intervertebral Disc Cells by Bermudez-Lekerika *et al.* published in front Cell Dev Biol. 2022 [1].

Low back pain (LBP) stands as the primary cause of morbidity globally, impacting roughly 80% of individuals in Western nations throughout their lives and resulting in 5 million disability-adjusted life-years among young adults [2]. The prevalence of intervertebral disc (IVD) degeneration increases progressively with age but is also prevalent in individuals younger than 30, indicating the involvement of various factors such as age, abnormal physical loading [3], environmental influences [4], endocrine effects [5] and hereditary factors [6–8]. Given the intricate and multifaceted nature of IVD degeneration, understanding the initiating and risk factors remains limited, significantly impeding effective LBP patient stratification.

1.1 THE STRUCTURE OF THE INTERVERTEBRAL DISC (IVD)

IVDs are located between the vertebral bodies of the spine. The IVDs are part of a "three-joint complex" that includes the two posterior articulations of the diarthrodial facet joints, along with the soft tissues of the IVD between the two adjacent vertebral bodies [9]. Their function is to absorb and transfer high loading forces from body weight and muscular activity, as well as to provide flexibility to the human spine [10]. A total of 25 IVDs are part of the human spine. Based on their anatomical location they can be subdivided into 7 cervical, 12 thoracic, 5 lumbar and one between the lumbar and sacrum. The IVD is the largest avascular organ within the human body. Blood vessels are solely found in the

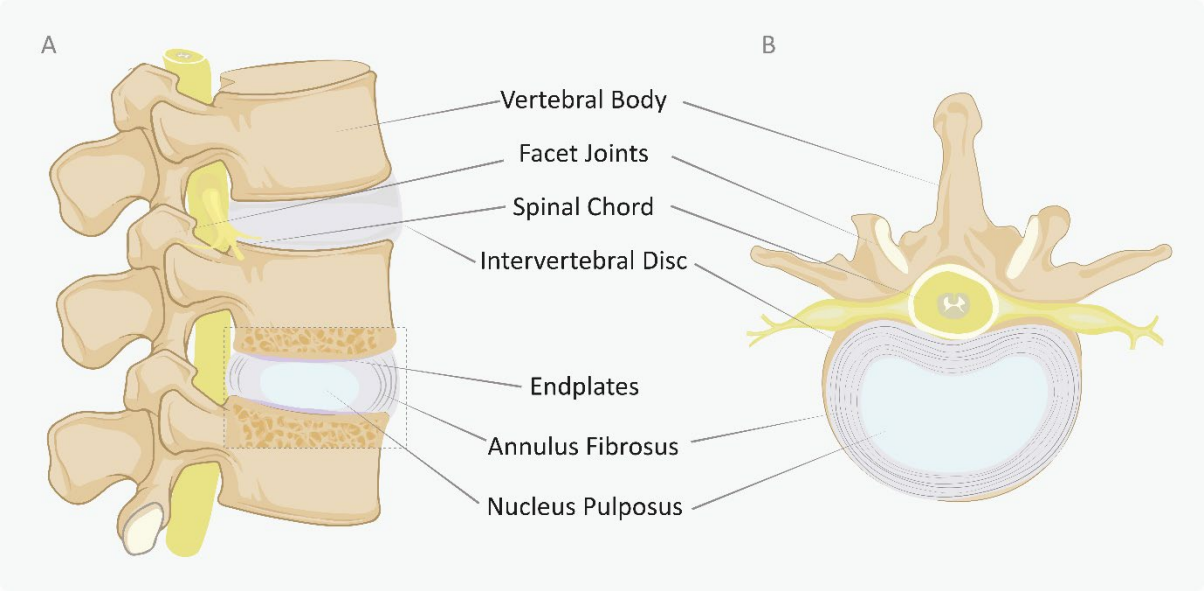

Figure 1.1 | Anatomy of the human lumbar intervertebral disc (IVD)

A Two motion segment of the lumbar spine comprised of 2 adjacent vertebrae separated by the IVD. The sagittal view of the IVD shows its different regions, the annulus fibrosus, the cartilaginous endplates and the central nucleus pulposus. **B** Transverse view of the IVD showing its composition. The outer annulus fibrosus with lamellar fibrocartilaginous structure and the inner gelatinous nucleus pulposus.

outer annulus fibrosus (AF) and bony endplates which protrude into the edge of the cartilaginous endplates. All exchange of nutrients and waste products occurs through diffusion across the extracellular matrix (ECM) of the IVD [11]. Due to the avascularity of the tissue, the environment is hypoxic with an oxygen tension within the IVD considered between 1 and 5% [12]. The IVD comprises three anatomic regions (Figure 1.1): a gelatinous core, the nucleus pulposus (NP); the AF, which is a fibrocartilage ring that confines the NP laterally; and two cartilaginous endplates (CEP) [10].

1.1.1 CARTILAGINOUS ENDPLATES

Both the superior and inferior ends of the IVD are covered by a thin layer of hyaline cartilage layers, known as the CEPs. The CEP is a unique tissue, distinct from other cartilaginous tissues in terms of morphology, gene expression, mechanical function, and transport properties [13,14]. Its thickness varies significantly, even within healthy IVDs, ranging from 0.1 to 1.6 mm, depending on factors such as age, disc level, position within the IVD (cranial vs. caudal), and location within the tissue (central vs. peripheral) [15]. Over the course of life, the composition and structure of the CEP undergo continuous change. At birth, the human CEP is thicker, occupying approximately 50% of the intervertebral space; by adulthood, this is reduced to around 5% [16]. Additionally, blood vessels present in the CEP during early life are progressively replaced by cartilaginous extracellular matrix, eventually disappearing almost entirely by skeletal maturity [16–18]. In contrast to other animals, such as sheep or cattle, the CEP in humans serves as a growth plate for the vertebrae until the teenage years, after which only a thin layer of hyaline cartilage remains [16,17]. Ossification of the vertebral body begins early in life, including the vertebral side of the endplate, forming the bony endplate (BEP) [18]. This results in a porous layer of merged trabecular bone with pockets of vascularised bone marrow, allowing bidirectional transport of nutrients and metabolic waste [19]. While the vertebral side of the endplate ossifies, the disc-facing side remains cartilaginous, forming the CEP, which is rich in type II collagen, proteoglycans, and water [20] and serves both mechanical and biochemical roles. In adults, the CEP becomes avascular, but a dense network of capillaries at its base, formed by terminal branches of arteries, persists [21] (Figure 1.2). The CEP plays a crucial role in nutrient diffusion from peripheral blood vessels into the IVD and facilitates the removal of waste from the avascular disc. Its transport properties are influenced by its porosity and matrix composition [22], whilst solute transport into and out the IVD depends on solute size [23], shape, weight, and ionic charge [24]. Mechanical forces are essential for cartilage homeostasis, as the chondrocytes and chondrocyte-like cells within the CEP respond to mechanical stimuli, helping regulate mechanical loading [25] . Compressive, tensile, and shear forces, along with fluid movement, are vital for CEP function [26]. While physiological loading supports disc health, excessive loading can cause vertebral endplate fractures or other injuries [27]. Moreover, dynamic loading enhances both small

and large solute transport through the CEP, particularly in discs with low porosity, where osmosis and diffusion are less efficient [28].

1.1.2 ANNULUS FIBROSUS

The AF constitutes the peripheral portion of the IVD providing a fibrous matrix binding together the outer rims of adjacent vertebra and attaches to the end plate. It can be categorised into two regions: the outer and inner AF [29,30]. The outer AF consists of highly organised type I collagen fibre bundles forming concentric lamellae (Figure 1.2). The fibres of adjacent lamellae are oriented in opposite directions, crossing each other obliquely at angles of around 60° [10]. The orientation of the lamellae provides the outer AF resilience against tensile forces incurred from spinal bending and twisting [29]. The thickness of each lamella ranges from 100 to 500 μm, in which the peripheral lamellae are thicker than the central lamellae [31]. Each lamella is separated by an interlamellar tissue containing a proteoglycan rich matrix, elastic fibres, and cells, possibly providing mechanical integrity of the AF [32]. The collagen fibres within the outer AF are anchored to the vertebral body connecting one vertebra with the adjacent one [33].

The inner AF serves as a transitional zone between the highly organised outer AF and the gelatinous NP. It expresses characteristics of both tissues. A morphological feature of the transitional zone is the reduction of the structured lamellae of type I collagen and the increase in irregularly oriented type II collagen fibres. Whilst the outer AF is directly connected with the vertebra the inner AF is linked with the CEP and presents in an intact disc a fully avascular structure [34].

1.1.3 NUCLEUS PULPOSUS

The central NP lies between the cranial and caudal CEPs and laterally confined by the surrounding, fibre-reinforced AF. The NP consists primarily of water (70–80%), with randomly arranged type II collagen fibres, radially organised elastin, and smaller amounts of collagen types IV, VI, IX, and XI [35]. These elements are embedded within a proteoglycan-rich matrix, where aggrecan serves as the main proteoglycan component, linking to hyaluronan to anchor within the tissue [36,37]. Proteoglycans, with their negatively charged glycosaminoglycan (GAG) side chains—such as chondroitin sulphate and keratan sulphate—attract water and cations through osmosis, generating high osmotic and hydrostatic pressure in the NP [37] (Figure 1.2). This pressure endows the NP with viscoelasticity and resistance to compression. Due to the very low oxygen tension in the NP, NP cells predominantly rely on the glycolytic pathway for energy metabolism [38].

The cell population of the early postnatal NP mainly consists of notochordal cells that are commonly arranged in clusters. In humans, mature NP cells replace the notochordal cells during the first decade of life [39]. Phenotypical features of mature NP cells have been shown to differ from other chondrocyte-like cells and reflect their adaption to the hypoxic, acidic, nutrition deprived micro-environment of the nucleus pulposus, and their differential embryonic origin. The cell density of NP cells is around $4x10^6$ cells/cm^3 [40] lower than in articular cartilage which is estimated to consist of $5\text{-}20x10^6$ cells/cm^3 depending on the zone [41].

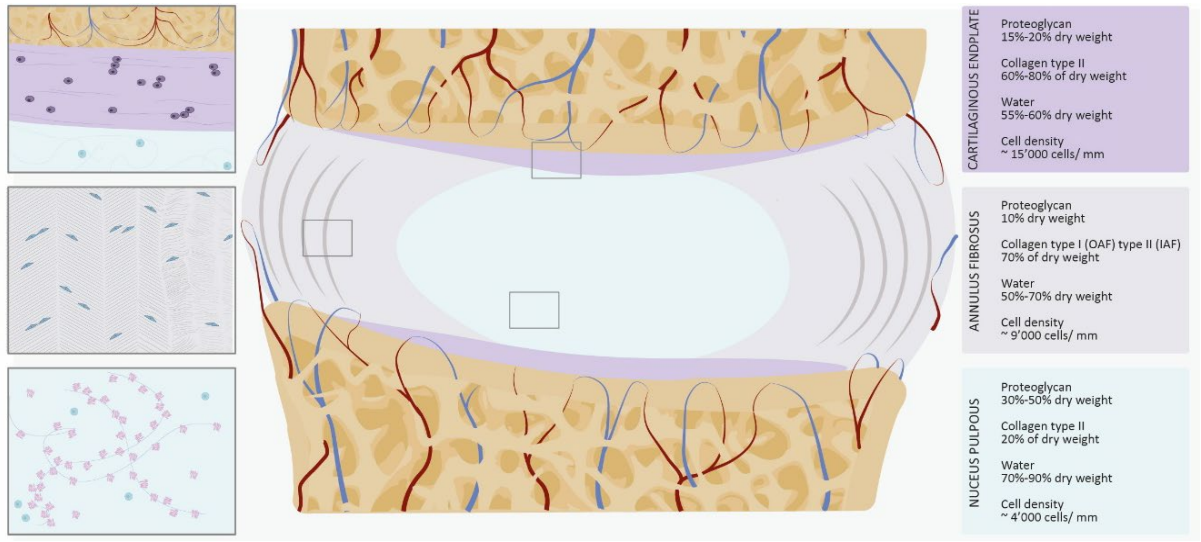

Figure 1.2 | Structure and composition of IVD components

The middle image represents a sagittal IVD section, showing the blood supply and the different components CEP, AF and NP. On the left side are zoomed in regions, showing the matrix and cell composition. The right side lists the components of each IVD tissue type.

1.2 DEVELOPMENT OF THE IVD

IVDs derive from two embryonic structures, the notochord, and the sclerotome. The NP is derived from the notochord while all other connective tissues of the spine including the AF, the vertebral bodies, the CEPs as well as all tendons and ligaments are derived from the sclerotome [42]. The notochord is a defining structure of chordates, forming a central, rod-like axis within the embryo [43]. During embryonic development, it acts as both a supportive structure and a signalling centre, guiding the formation and differentiation of surrounding tissues, including the neural tube [44,45] and sclerotome [46] by releasing growth factors and morphogens [47]. The sclerotome originates from somites, temporary structures positioned next to the notochord and neural tube during vertebrate development [48]. Lead by wingless-related integration site (WNT) signalling from the notochord and sonic hedgehog (SHH)

signalling from the ectoderm, the somites undergo compartmentalisation [44]. This development is marked by the division of somites into ventral, lateral, and dorsal sub-compartments, with the dermomyotome forming to produce connective tissue for the axial skeleton [49]. The ventral sub-compartment produces the vertebral bodies, the AF and the CEPs of the IVD [50].

As the vertebrae, AF, and CEP develop, the notochord retracts from the vertebral bodies. Notochordal cells are displaced from these regions and become concentrated at the centre of the forming IVD, which then expands to generate the NP [42]. The notochordal sheath encloses the retreating notochord and maintains internal hydrostatic pressure, which is crucial for notochordal expansion and subsequent NP formation [42]. In humans, the number of notochordal cells within the notochord and eventually the NP starts to decline during maturation, even in early embryonic development [39]. This decline continues until notochordal cells are nearly absent within the NP after the first decade of life in humans [51].

1.3 INTERVERTEBRAL DISC DEGENERATION

Disc degeneration is a complex, progressive condition that inevitably occurs with aging, but occurs at an accelerated rate in some individuals [52]. Although the initial factors driving the degeneration process are still not fully understood, multiple contributors such as genetics and epigenetics [53], altered biomechanics [54], the microenvironment [55], bacterial involvement [56] , as well as factors such as smoking and obesity, can all play a role in disc degeneration (Figure 1.3). Disc degeneration is marked by increased levels of catabolic cytokines, which accelerate the breakdown of aggrecan and collagen, leading to changes in disc structure and function [16]. Morphologically, it becomes more difficult to distinguish between the NP and AF as the NP transitions from a gel-like consistency to a more fibrotic state [57]. Degeneration also results in a reduction of water-attracting proteoglycans in the NP [58], impairing the osmotic resistance of the IVD and reducing its ability to withstand compressive forces [59]. The loss of hydrophilic matrix components leads to structural changes, which are the primary causes of disc herniation and sciatica resulting from nerve root compression [16]. Degeneration also compromises the integrity of the CEP and BEP, altering the mechanical and nutritional balance within the IVD, further accelerating degeneration [60]. As degeneration progresses, the reduced permeability of the CEP limits nutrient transport, hindering oxygen supply to the disc [61], which in turn reduces cell viability and activity [22].

1.4 THE SHIFT FROM ANABOLISM TO CATABOLISM

During disc degeneration, the balance between anabolism (matrix synthesis) and catabolism (matrix breakdown) becomes dysregulated. Disc cells show increased expression of proinflammatory and catabolic cytokines as degeneration progresses [62]. Key cytokines secreted during this process include Interleukin (IL)-1, IL-6, IL-17, IL-8, interferon-gamma (IFN-γ), and tumour necrosis factor (TNF), with IL-1 and TNF being the most studied, both strongly implicated in the pathogenesis of IVD degeneration [63–65]. In healthy, non-degenerated discs, IL-1 receptor I (IL-1RI), IL-1 (α&β), and their inhibitor IL-1 receptor antagonist (IL-1Ra) are expressed, maintaining matrix homeostasis through the balance of IL-1 agonists and IL-1Ra. However, in degenerated discs, immunohistochemical staining reveals an increase in IL-1 agonists and IL-1RI without a corresponding rise in IL-1Ra, disrupting the balance and triggering catabolic activity [63]. TNF expression also increases during degeneration, though its receptor TNF-RI does not. Hoyland et al. found that inhibiting TNF did not affect matrix degradation, while inhibiting IL-1 fully blocked matrix degradation, emphasising IL-1's central role in disc degeneration over TNF [66]. In contrast, Andrade et al. reported an increase in both TNF receptors (TNF-RI, TNF-RII) in herniated discs, correlating with pain levels on the visual analogue scale, suggesting TNF plays a role at least following herniation and during pain manifestation [67]. Additionally, IL-6 levels rise in herniated discs [68], and Studer *et al*. demonstrated that IL-6 enhances IL-1 and TNF-induced upregulation of matrix-degrading factors in NP cells [69]. IL-6, in conjunction with TNF, also contributes to the development of neuropathic pain, exacerbating sciatica symptoms [70,71].

In response to this catabolic environment, disc cells produce several matrix-degrading enzymes, such as a disintegrin and metalloproteinase with thrombospondin motifs (ADAMTS) especially ADAMTS-4, -5, and matrix metalloproteinases (MMPs) 1, 2, 3, 9, and 13 (Figure 1.3) [72]. These enzymes promote the breakdown of key extracellular matrix components like aggrecan and collagen type II, leading to altered IVD structure and function [73]. Continuous matrix degradation results in mechanical instability and annular tears. In addition, neurotrophic and angiogenic factors, such as nerve growth factor (NGF), brain-derived neurotrophic factor (BDNF), substance P (SP), and vascular endothelial growth factor (VEGF), are elevated in degenerating discs [74–76]. Annular tears and fissures in the AF allow for blood vessels and nerve growth into the disc, with higher Pfirman grades (indicating advanced degeneration) correlating with increased blood vessel ingrowth [77]. This vascular ingrowth is accompanied by immune cell migration, further amplifying cytokine and chemokine production within the disc [78]. This creates a vicious cycle of inflammation-driven catabolism, working in synergy with native IVD cells to accelerate extracellular matrix breakdown [65].

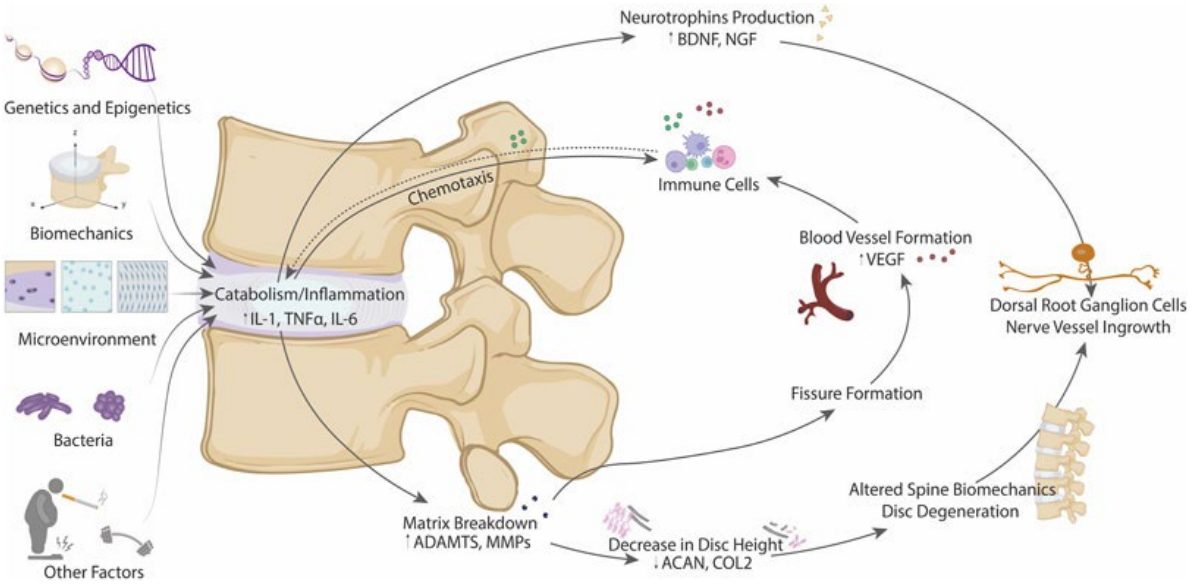

Figure 1.3 | Schema of Factors involved in Disc Degeneration

A schematic representation illustrating the various factors contributing to the metabolic shift from anabolism to catabolism in disc degeneration, including genetic and epigenetic influences, biomechanical forces, the microenvironment, bacterial presence, and additional elements. These contributors collectively trigger downstream biochemical processes, such as matrix degradation and neurotrophin production, which result in structural and biomechanical changes, nerve infiltration, and blood vessel formation. Consequently, the immune system becomes involved through chemotaxis, disrupting the immune-privileged state of the intervertebral disc. Created by Andrea Nüesch for review on immuno-modulatory effects of IVD cells [1].

1.5 MODIC CHANGES

Modic changes (MC) are vertebral bone marrow lesions visible on MRI scans as signal intensity changes in the vertebral bone marrow around a degenerated IVD [79,80] (Figure 1.4). Three variations of MC have been characterised according to their appearance in T1-weighted (T1w) and T2-weighted (T2w) images [56]. Modic type 1 changes (MC1) appear as hypointense regions on T1w images and hyperintense regions on T2w images, indicating the presence of oedema, fibrovascular granulation tissue, immune cell infiltration, and an increase in profibrotic stromal cells [81] (Figure 1.4). Modic type 2 changes (MC2) are characterised by hyperintensity on both T1w and T2w images, reflecting fatty marrow conversion along with fibrotic tissue [81] (Figure 1.4). Modic type 3 changes (MC3) appear as hypointense regions on both T1- and T2-weighted images and are associated with sclerotic alterations [82]. MC1 and MC2 are convertible over time and can eventually convert to MC3 [83,84]. Around 20% of MCs occur as a mixed type MC1/2 or MC2/3 [85]. Modic changes typically start adjacent to a degenerate disc, at the endplate [86,87]. The bigger the MC region the more likely the IVD is degenerated, and the patient suffers from LBP [88]. Karchevsky *et al*. showed in a systematic review that the prevalence of MC in LBP patients is about

seven times higher than in the non-clinical population [89] underlining the association between MC, especially MC1 and chronic LBP [90,91]. Despite the high specificity of MC for degenerate discs, the low sensitivity indicates that disc degeneration alone is not sufficient to trigger MC in most cases [86]. Määttä *et al.* found in large population-based study a strong and independent association of endplate defects with disc degeneration and MC [92]. Damage to the endplate triggers a cascade of degenerative changes in both the vertebrae and the disc, and in cases of severe endplate damage, chronic LBP is more likely, suggesting a sustained stimulus and prolonged inflammation [93]. The inability to eliminate the inflammatory trigger results in chronic inflammation accompanied by fibrosis and granulation tissue, leading to cumulative damage marked by persistent inflammation, fibrosis, and increased bone turnover [56]. Two aetiologies, both presupposing structural disc damage as herniation or endplate damage, have been suggested for MC1; (1) an auto immune reaction of the bone marrow to the disc cells, and their secreted factors; (2) occult discitis [94].

The aetiology of MC may involve autoimmunity. After the disc's embryologic development, the NP is isolated from systemic circulation, maintaining immune privilege [95]. Damage to the endplate can expose the NP to bone marrow leukocytes, leading to an adaptive immune response. Peripheral disc damage may expose the NP to the immune system, triggering an autoimmune response [96–98]. This

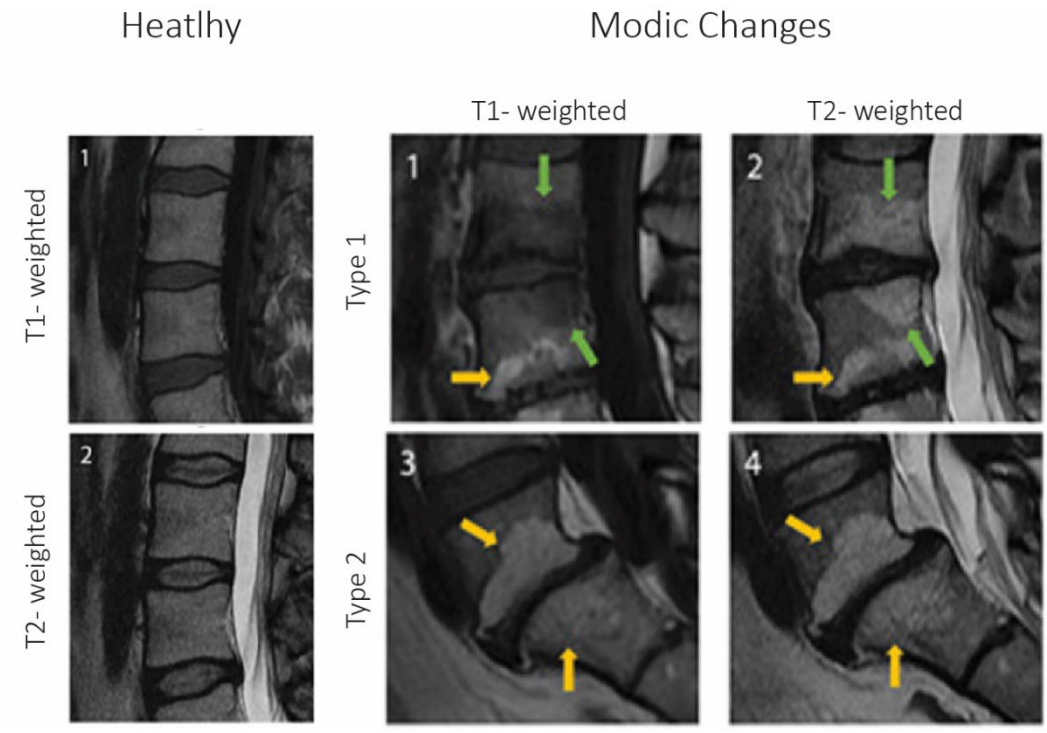

Figure 1.4 | Modic changes

Examples of cartilaginous endplate (CEP) and bony endplate (BEP) appearance in standard of care MRI from a healthy patient (left). Modic changes (MC) type 1 and type 2 in T1- and T2 weighted image. (MC1) In type 1 MCs extending from L3-L4 IVD, the green arrows indicate the cranial and caudal BEP. A type 2 MC also visible in the L4 vertebral body indicated with the arrow in orange. (MC2) Type 2 MC extending from L5-S1 IVD indicating the cranial and caudal BEP with orange arrows. Adapted from Crump et al.

aligns with findings in herniated and degenerated discs [99]. Additionally, disc ECM and proteoglycans are linked to immune responses, potentially prolonging clinical symptoms in LBP patients [100].

An infective aetiology is supported by the disc's anaerobic environment, susceptibility to damage, and limited repair capacity. Peripheral disc damage may allow low-virulence bacteria such as *Cutibacterium acnes* (Moore *et al.* 1963)[101] to enter through the circulatory system through everyday activities [102,103]. While immune surveillance and the aerobic environment in the blood limit systemic infection, the disc's low oxygen environment (1-5% O_2, 5-21 mmHg [104]) is ideal for anaerobic bacterial growth. Heggli *et al*. suggests the existence of two different biological MC1 types, one having a low copy number of *C. acnes*, whilst the other has a high copy number of *C. acnes* having an increased adaptive immune cell signature [105].

While disc or endplate damage, infection, and autoimmunity are plausible explanations for the aetiology of MC, they do not explain why some patients with disc and/or endplate damage develop MC, while others do not. This suggests that the likelihood of developing MC may depend on the intensity and persistence of the inflammatory stimuli, as well as the composition and metabolic state of the bone marrow [56].

1.6 CROSS-TALK BETWEEN THE IMMUNE SYSTEM AND IVD

As mentioned, the IVD is the largest avascular organ with blood vessels only present in the outer AF and bony endplates, so all metabolite exchange takes place via diffusion through the dense ECM of the IVD. The dense ECM of the IVD inhibits blood vessel ingrowth both mechanically by having a high physical pressure, and chemically through high proteoglycan concentration [106,107], which combined with secretory inhibitors prevents nerve and blood vessel ingrowth in non-degenerate discs [108,109]. The AF and the CEP, along with the secretory inhibitors of angiogenesis, are defined as the blood-NP barrier (BNB), which strongly isolates the NP from the circulation and thus the host immune system [110].

Where both AF and CEP are intact, the IVD has been described as an immuno-privileged tissue [110] with a lack of immune cells. However, this is often confused as the native cells of the disc (i.e., the NP, AF and CEP cells) have been shown to take on roles and markers classically expressed by immune cells [63,65,111,112] as a result, some authors have described this as an immune response or inflammation. However, the activity of native IVD cells does not represent true inflammation. Therefore, it is crucial to distinguish which cases of IVD degeneration involve an immune response, as this would necessitate different clinical interventions and treatments. Native disc cells produce a variety of cytokines and chemokines that become upregulated during disc degeneration, driving numerous catabolic processes

within the IVD.[63,66,112–114]. A shift to catabolism is at least in part driven by the increased production of cytokines in the disc by the native cells (in an intact disc) and a combination of inflammatory cells and native disc cells following CEP and AF rupture. Phillips *et al.* (2015) [113] demonstrated that NP cells express a number of cytokine and chemokine receptors and are thus able to respond in a paracrine and autocrine manner (Figure 1.3). Caused by different, yet not fully understood mechanisms, disc cells upregulate the expression of inflammatory cytokines such as IL-1α&β, TNF, IL-6, IL-8 and IL-17 amongst others creating a cytokine rich catabolic environment. IL-1 has been shown to drive the catabolic events during disc degeneration [63,66,112–114]. Whilst other cytokines and chemokines (e.g., MCP-1, TNF, IL-8) produced in the disc appeared to have limited effects on the native disc cells due to lack of receptor expression *in vivo* [62,113], they undoubtedly diffuse to the surrounding tissues leading to increased inflammation in local tissues and drive cellular infiltration following AF and CEP rupture and increased sensitisation of nerves [115]. Cytokines such as IL-1 can stimulate specific intracellular signalling pathways that further enhance the degenerative process [116,117] and upregulate matrix-degrading enzymes known as MMPs and ADAMTS, particularly MMP- 1, 2, 3, 9, 13 and ADAMTS-4, 5 [118]. In later phases of IVD degeneration, these cytokines can upregulate neurotrophic and angiogenic factors, which could lead to further nerve and blood vessel ingrowth [74,76,119] (Figure 1.3).

Remarkably, some of these cytokines, such as IL-1, have also been shown to be expressed in cells from non-degenerate discs and display roles in maintaining normal homeostasis [63,113]. Indeed, if the IL-1 agonists are knocked out during development, IVD degeneration can be induced [63,120]. Thus, IL-1 plays a role as a normal regulatory mechanism during IVD homeostasis, which becomes imbalanced during IVD degeneration [63] (Figure 1.3). Native NP cells have also been shown to take on other roles normally associated with immune cells such as phagocytosis, for example Jones *et al*. (2008) [111] observed the capacity of bovine NP cells to ingest latex beads at least as efficiently as phagocytic cells and ingested apoptotic cells. This capability could be of great physiological relevance to maintain a healthy disc, as it may prevent inflammation triggered by the release of toxic or immunogenic intracellular content by apoptotic cells [121]. Clearly, the suggestion from some reviews that cytokine production within the disc is solely from immune cells is inaccurate [115]. However, when the AF or CEP becomes ruptured, or fissures occur during injury or disc degeneration this provides a route for blood vessel ingrowth and migration of immune cells into the intervertebral disc. Within these “non-intact” IVDs, immune cells will migrate including T cells ($CD4^+$, $CD8^+$), B cells, macrophages, neutrophils and mast cells [65] (Figure 1.3).

These immune cells then contribute to an inflamed environment in the disc, leading to further increases in cytokine and chemokine expression [113]. This leads to a viscous circle of inflammatory driven catabolism which acts synergistically with the native IVD cells to cause accelerated ECM

breakdown [65] (Figure 1.3). These cytokines and chemokines play several roles within the disc, including direct actions on NP, AF and CEP cells where their receptors are present [62,63,113]. They will also likely diffuse out of the IVD leading to increased cellular migration to the disc [122], or sensitisation of local nerve roots [123,124].

1.7 BACTERIAL PRESENCE WITHIN THE DISC

In 2001, Stirling *et al*. were the first to report the presence of anaerobic bacteria, particularly *C. acnes*, in herniated disc tissue of 43 out of 140 patients with sciatica [102]. Building on this pioneering work, Alberts *et al*. [125] and later Capoor *et al*. [126,127] confirmed that herniated discs harbour bacteria, primarily opportunistic anaerobic or facultative anaerobic species such as *C. acnes* and coagulase-negative *Staphylococci*. Since these initial findings, the concept of disc infection and the potential existence of a disc microbiome has sparked considerable debate in the spine research field, challenging the long-held view that the IVD is sterile [128–130].

Subsequent studies have attempted to replicate these bacterial findings using a variety of laboratory techniques. Methods employed to detect bacteria included selective microbial cultures and targeted PCR, though only a few more recent studies used universal PCR or genome-wide sequencing [130–134]. Microbial culture methods are inherently limited by the conditions selected for cultivation; for example, *C. acnes* is a slow growing, aerotolerant anaerobic Gram-positive bacterium that requires specific anaerobic conditions and extended incubation periods to grow on solid media [135]. Both microbial culture and sequencing techniques face the challenge of differentiating true bacterial presence from perioperative contamination, highlighting the need for contamination control samples in such studies. Furthermore, use of various methodologies and the absence of standardised protocols have led to inconsistent results across studies.

In recent years, 16S rRNA sequencing has enabled the unbiased identification and quantification of disc bacteria, even from low-biomass samples. Rajasekaran *et al*. utilised 16S rRNA sequencing and identified a diverse microbiome in healthy, degenerate, MC, and herniated IVDs, linking various pathologies with dysbiosis [136,137]. Mengis *et al*. supported Rajasekaran's findings by providing further evidence that the disc harbours its own microbiome, as well as highlighting differences in the detection and abundance of microbes across various pathological groups [138]. Although both studies reached similar conclusions, they reported notable differences in the types of bacteria detected. These discrepancies may reflect true biological variations, as the studies were conducted on different

continents, or they may arise from differences in sample preparation or bioinformatic analysis [138]. This underscores the need for standardised protocols for sample preparation and bioinformatic analysis.

As a result, current 16S rRNA sequencing datasets from disc samples vary, and it remains unclear which bacterial species are part of a healthy disc, and which are associated with pathological conditions. With emerging evidence suggesting the presence of bacteria within the disc, clinical trials of oral antibiotics targeting MC1 pathogenesis have been conducted, however studies show mixed results with only a subset of patients responding with benefits to antibiotic treatment compared to placebo [139–142] .

Inoculating *C. acnes* into caudal IVDs has been shown to induce disc degeneration, leading to endplate resorption and MRI changes resembling MC1 in both rats [143,144] and rabbits [145,146]. Although these findings suggest that *C. acnes* may be pathogenic, they do not account for the possibility that the IVD itself might already harbour a microbiome. Additionally, *C. acnes* has been detected in healthy human IVDs [147], which, raises the question: which bacteria in the disc are pathogenic, which are commensal, and how disc cells regulate their responses to bacterial presence?

1.8 PATTERN RECOGNITION RECEPTORS

Pattern recognition receptors (PRRs) are a group of receptors originally identified in the innate immune system, capable of recognising specific molecular patterns present on pathogens, termed pathogen-associated molecular patters (PAMPs) as well as on apoptotic and damaged senescent cells, termed damage associated molecular patterns (DAMPs). These receptors trigger immune-protective responses and play a critical role in initiating and mediating specific immune reactions [148]. PRRs are classified into five types based on their protein domain structure: toll-like receptors (TLRs), nucleotide-binding oligomerisation domain (NOD)-like receptors (NLRs), retinoic acid-inducible gene-I (RIG-I)-like receptors (RLRs), C-type lectin receptors (CLRs), and absent in melanoma-2 (AIM2)-like receptors (ALRs).

The most extensively studied class of PRRs are the TLRs, a family of type I transmembrane receptors. To date, 10 TLRs have been identified in humans, each recognising distinct PAMPs derived from various microbial pathogens, including viruses, bacteria, fungi, and protozoa [149]. In human IVD cells, the expression of TLR1, 2, 3, 4, 5, 6, 9, and 10 has been reported [150,151]. TLRs 1, 2, 4, 5, 6, and 10 are located on the cell surface, while TLRs 3 and 9 are found within endosomal compartments [152]. Among these, TLR2, which partners with TLR1 or TLR6, and TLR4, which can form homodimers, have been extensively studied. TLR2 primarily recognises components of bacteria in general such as peptidoglycans (PGN) or lipoteichoic acid (LTA) of Gram-positive bacteria, while TLR4 is activated by lipopolysaccharides (LPS)

from Gram-negative bacteria (Figure 1.5) [153]. Although the downstream signalling pathways of these receptors are not yet fully understood, current research suggests that different adaptor molecules, such as myeloid differentiation primary response protein 88 (MyD88) and toll/interleukin-1 receptor (TIR) domain-containing adaptor inducing interferon-β (TRIF), mediate distinct signalling cascades. For example, TLR4 activation can initiate both MyD88-dependent and TRIF-dependent pathways. Tenascin-C, an extracellular matrix glycoprotein, expressed at areas of inflammation and tissue damage acts as a TLR4 agonist, exclusively triggering the MyD88 pathway, while matrix component biglycan fragments activate both TLR2 and TLR4 in a MyD88-dependent manner [154,155]. Ultimately, TLR signalling leads to the activation of transcription factors such as nuclear factor kappa-light-chain-enhancer of activated B cells (NFkB) and activator protein-1 (AP-1), which regulate gene expression and promotes the production of catabolic cytokines [154].

NLRs are cytosolic pattern recognition receptors found in various cell types, including B cells [156], macrophages [157], dendritic cells [158], intestinal epithelial cells [159], monocytes, and keratinocytes [160]. These receptors play a crucial role in detecting invading pathogens and initiating the innate immune response but have not yet been investigated in the IVD. NOD1 and NOD2 are two well-characterised members of the NLR family that recognise specific structural motifs derived from bacterial PGNs such as muramyl dipeptide (MDP) (Figure 1.5) [161–164]. Upon activation, NOD1 and NOD2 oligomerise and recruit signalling molecules, leading to the activation of NFkB and AP-1, which drive the expression of catabolic cytokines. Additionally, upon viral stimulation they regulate IRF3- and IRF7-dependent expression of type I interferons [165]. Other well-researched NLRs include NLR family pyrin domain-containing 1 (NLRP1), NLRP3, and NLR family CARD domain containing 4 (NLRC4) [166]. Upon activation, these NLRs oligomerise to form multiprotein inflammasome complexes, leading to the cleavage and activation of caspase-1, which promotes the secretion of IL-1β and IL-18 [167] and triggers inflammatory cell death through pyroptosis. Among these, NLRP3 is the only NLR that has been studied in relation to IVDs and has been linked to IVD degeneration [168]. Intracellular oxidative stress, mitochondrial dysfunction, endoplasmic reticulum stress, and lysosomal rupture, caused by various stimuli are all implicated in the activation of the NLRP3 inflammasome in IVDs (Figure 1.5) [169]. Moreover, recent studies suggest that *C. acnes* accelerate IVD degeneration by inducing pyroptosis in NP cells via the ROS-NLRP3 pathway [168].

CLRs are a diverse family of soluble and transmembrane proteins, with multiple members functioning as PRRs involved in antifungal, antiviral, and antibacterial immunity. CLRs are primarily expressed on antigen-presenting cells such as macrophages and dendritic cells; however, their presence and role within the IVD have not yet been investigated [170]. RLRs are another subset of cytosolic PRRs that detect viral RNA [171], leading to the upregulation of catabolic cytokines. Additionally, ALRs have been

implicated in the recognition of cytosolic DNA and are thought to play a role in inflammasome pathways, though their precise function is not fully understood [172]. To date, none of these receptor families—CLRs, RLRs, or ALRs—have been explored in the context of the IVD.

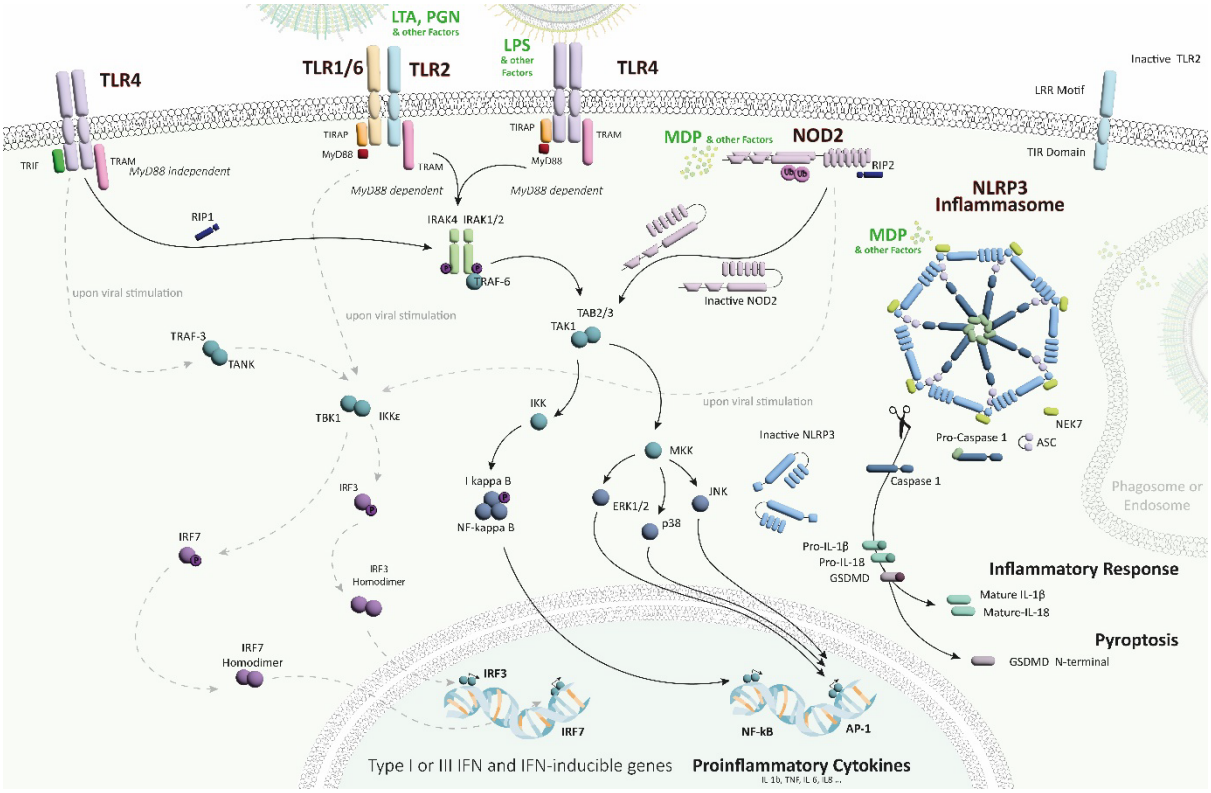

Figure 1.5 | Overview of TLR2, TLR4, NOD2 and NLRP3 inflammasome signalling

TLR4 homodimers and **TLR2** heterodimers (TLR2-TLR1 or TLR2-TLR6) recognise pathogen-associated membrane components on the cell surface. While TLR4 is located at the plasma membrane, its activation triggers endocytosis into the endosome. Upon binding to their respective ligands, TLR signalling is initiated through receptor dimerization, which allows the TIR domains of the TLRs to interact with adaptor proteins like TIRAP and MyD88 or TRAM and TRIF. MyD88 engagement leads to the recruitment of downstream signalling molecules, ultimately activating the transcription factors NFκB and AP-1**. NOD2**, found in the cytosol, oligomerises upon activation and recruits signalling molecules, also resulting in NFκB and AP-1 activation, driving the expression of catabolic cytokines. Additionally, in response to viral stimulation, the TLR4 homodimer, TLR2-TLR1 or TLR2-TLR6 heterodimers, and NOD2 regulate IRF3- and IRF7-dependent expression of type I interferons. Activation of the **NLRP3** inflammasome involves the recruitment of pro-caspase-1, ASC, and NEK7, leading to the cleavage of pro-IL-1β and pro-IL-18 into their active forms, as well as cleaving GSDMD, triggering pyroptosis.

This figure represents a compilation of various signalling pathways in immune cells; however, whether these mechanisms apply to the intervertebral disc remains to be determined through further investigation.

1.9 AIMS AND OBJECTIVES

The presence of bacteria within the IVD and their role in disc degeneration remain controversial topics. Numerous studies have identified *C. acnes* and other microbes using 16S rDNA sequencing and microbial cultures. However, these studies do not clarify whether the detected bacteria are true *in vivo* residents of the disc or simply perioperative contaminants. The overall aim of this PhD was to determine the presence of a microbiome in the intervertebral disc and investigate its potential influence on disc cells.

SPECIFIC OBJECTIVES

1. Establishment of a methodology for immunohistochemical analysis of tissues with low cellularity that ensures reproducible immunopositivity rates with high accuracy, reduces evaluation time, and maintains transparency minimising variability between individuals and laboratories (Chapter 2).

2. Investigate the presence of bacteria in non-herniated IVD tissue using immunohistochemistry, with a focus on distinguishing perioperative contamination from true *in vivo* bacterial colonisation (Chapter 3).

3. Assess bacterial growth and survival under conditions that mimic the IVD microenvironment (Chapter 3).

4. Examine correlations between PRRs, catabolic factors, and bacterial presence, and investigate the effects of bacterial exposure on human disc cells, with particular emphasis on the signalling pathways activated in response to such exposure (Chapter 3).

5. Investigate bacterial presence in intact bovine discs and examine the correlation between bacterial presence, TLRs, and catabolic factors (Chapter 4).

6. Explore potential mechanisms by which bacteria may invade intact discs using a healthy bovine whole organ co-culture model (Chapter 4).

CHAPTER 2

APPLICATION AND VALIDATION OF SEMI-AUTOMATIC QUANTIFICATION OF IMMUNOHISTOCHEMICALLY STAINED SLIDES FOR LOW CELLULAR TISSUE SUCH AS INTERVERTEBRAL DISC USING QUPATH

APPLICATION AND VALIDATION OF SEMI-AUTOMATIC QUANTIFICATION OF IMMUNOHISTOCHEMICALLY STAINED SLIDES FOR LOW CELLULAR TISSUE SUCH AS INTERVERTEBRAL DISC USING QUPATH

Andrea Nüesch[1*], Maria Paola Ferri [2,3*], Christine L Le Maitre[1]

[*]These two authors contributed equally to this work
[1]Division of Clinical Medicine, School of Medicine and Population Health, University of Sheffield, Sheffield, UK , [2] Barcelona Supercomputing Center, Barcelona, Spain , [3]Universitat de Barcelona, Barcelona, Spain

This manuscript has been submitted on the 14-Oct-2024 to JOR Spine.

AUTHOR CONTRIBUTIONS

AN, MPF, CLLM contributed to conception of the study and the study design. AN created the scripts for the QuPath part as well as the additional step-by-step guide for it on QuPath. MPF created the python scripts to calculate the final positivity rate as well as to perform further analysis. MPF created the GitBook pages explaining the execution of the processing scanning data. CLLM was the initial evaluator of the GitBook enhancing its clarity. AN sent out a survey and further analysed it and performed methods evaluation. AN, MPF and CLLM drafted the manuscript; All authors critically revised the manuscript for intellectual content; All authors approve the final version and agree to be accountable for all aspects of the work

DETAILED AUTHOR CONTRIBUTION

I wrote the abstract, parts of the introduction, the study design, sample preparation and digitisation, the image processing in QuPath, the methods evaluation, the results section, parts of the discussion, and the conclusion. I also created the QuPath section on GitBook, contributed to parts of the general pipeline, and developed the QuPath script. All visuals were created by me. In addition, I performed data analysis to evaluate the method and communicated with GitBook evaluators to improve the clarity of the guide.

Maria Paola Ferri contributed to sections of the introduction, the Python package for processing and scanning data, and parts of the discussion. She also developed the Python scripts and authored the guide on how to use them, available on GitBook and GitHub. Christine Le Maitre reviewed the manuscript, provided valuable feedback, tested the step-by-step GitBook guide, and conducted analysis on slides used for method evaluation.

No conflicts of interests

ABSTRACT

Immunohistochemistry (IHC) is a widely used method for localising and semi-quantifying proteins in tissue samples. Traditional IHC analysis often relies on manually counting 200 cells within a designated area, a time-intensive and subjective process that can compromise reproducibility and accuracy. Advances in digital scanning and bioimage analysis tools, such as the open-source software QuPath, enable semi-automated cell counting, reducing subjectivity and increasing efficiency. This project developed a QuPath-based script and detailed guide for semi-automatic cell counting, specifically for tissues with low cellularity, such as intervertebral discs and cartilage. The methodology was validated by demonstrating and no significant differences ($p=0.783$, $p=0.386$) between the manual counting and the semi-automatic quantification while showing a strong correlation of the methods for both collagen type II staining ($r=0.09602$, $p<0.0001$) and N-cadherin staining ($r= 0.9044$, $p=0.0001$). Furthermore a strong correlation (ICC single raters = 0.853) between 3 individual raters with varying academic rank and experience in IHC analysis was shown using the semi-automatic quantification method. The approach ensures high reproducibility and accuracy, with reduced variability between raters and laboratories. This semi-automated method is particularly suited for tissues with a high extracellular matrix to cell ratio and low cellularity. By minimising subjectivity and evaluation time, it provides a robust alternative to manual counting, making it ideal for applications where reproducibility and standardisation are critical. While the methodology was effective in low-cellularity tissues, its application in other tissue types warrants further exploration. These findings underscore the potential of QuPath to streamline IHC analysis and enhance inter-laboratory comparability.

2.1 INTRODUCTION

Immunohistochemistry (IHC) is a standard technique used for the localization and semi quantification for protein detection [173]. IHC is extremely useful because it does not only preserve cell morphology and the tissue architecture, but is also highly sensitive, enabling the characterisation of certain biomolecules at protein level within the tissue [173]. The process involves applying a primary antibody that binds to a specific target protein. A secondary antibody, conjugated with either a fluorophore, enzyme, or biotin, then binds to the primary antibody, allowing for colorimetric analysis through substrate conversion. This enables the quantification of immunopositive and immunonegative cells [174].

The standard quantification of immunopositivity is to perform semiquantitative analysis by manually counting 200 cells within a region of interest [174]. However, manual scoring can be subjective and prevent reproducible and objective analysis essential for the quantification and correlation of proteins in biological tissue. Furthermore, by only counting 200 cells, regional variability may not be considered. With the advent of the ability to acquire high resolution digital scans of entire microscopic slides, combined with whole slide scanning and the use of new bioimage analysis tools such as QuPath, immunohistochemical analysis can be performed semi-automatically using digital image analysis [175–178].

QuPath is an open-source software for bioimage analysis and is often used for digital pathology. Featuring a user-friendly interface, embedded algorithms for tissue and cell detection, interactive machine learning capabilities, and the option for automated scripting, this offers a robust solution for analysing whole slide images [177]. Even though QuPath has a built-in algorithm for the detection of cells and their classification into immuno-positive and negative cells its accuracy is impacted by cellularity of the tissue, in particular tissues with low cellularity are impeded as tissue artefacts are wrongly detected as cells. Tissues considered to have high extracellular matrix to cell ratio include tendons [179], ligaments [180], cartilage [181] and the components of the intervertebral disc [182].

Additionally, while QuPath facilitates image analysis, it lacks tools for streamlined post-processing of large datasets. Users typically export data manually to platforms like Excel or R for further statistical analysis, a process that is labour-intensive and prone to error. Addressing these limitations is critical for ensuring reproducibility and standardisation in IHC analysis. To address this, within this program of work we developed the ProcessScanningData class, [183] a novel tool designed to automate the post-processing of data from various whole-slide image formats, including MRXS, NDPI, CID, and BIZ. This class integrates scanned image data with inventory metadata, calculates immunopositivity statistics, and produces detailed output files. Additionally, it generates visual outputs such as scatter plots and heatmaps, enabling efficient exploration of relationships between markers [184]. By automating these

processes, the tool significantly reduces the need for manual intervention, improving accuracy and efficiency, especially in the analysis of tissues with low cellularity [185].

The project aimed to create a QuPath-compatible script and an accompanying step-by-step guide tailored for semi-automatic cell counting and classification of H-DAB-stained slides, to specifically enable accurate determination of cellular immunopositivity. The methodology was designed to ensure reproducible immunopositivity rates with high accuracy, minimise inter-rater and inter-laboratory variability, and significantly reduce the time required for sample evaluation. The approach is particularly suited for the analysis of low-cellularity tissues, such as intervertebral discs, cartilage, and bone, where traditional methods fall short.

2.2 METHODS

2.2.1 STUDY DESIGN

In the initial phase of this study, a semi-automatic pipeline for quantifying low-cellularity Haematoxylin-DAB (H-DAB) stained tissue slides was developed. Presented as a two-step tutorial, the H-DAB semi-automatic method is designed to extract immunopositivity rates based on cellular classification in different tissues and compute statistical correlation analysis. The study design consisted of four key components: (1) Development of the QuPath pipeline: Samples were stained and digitised, followed by the creation of QuPath projects (Figure 2.1).

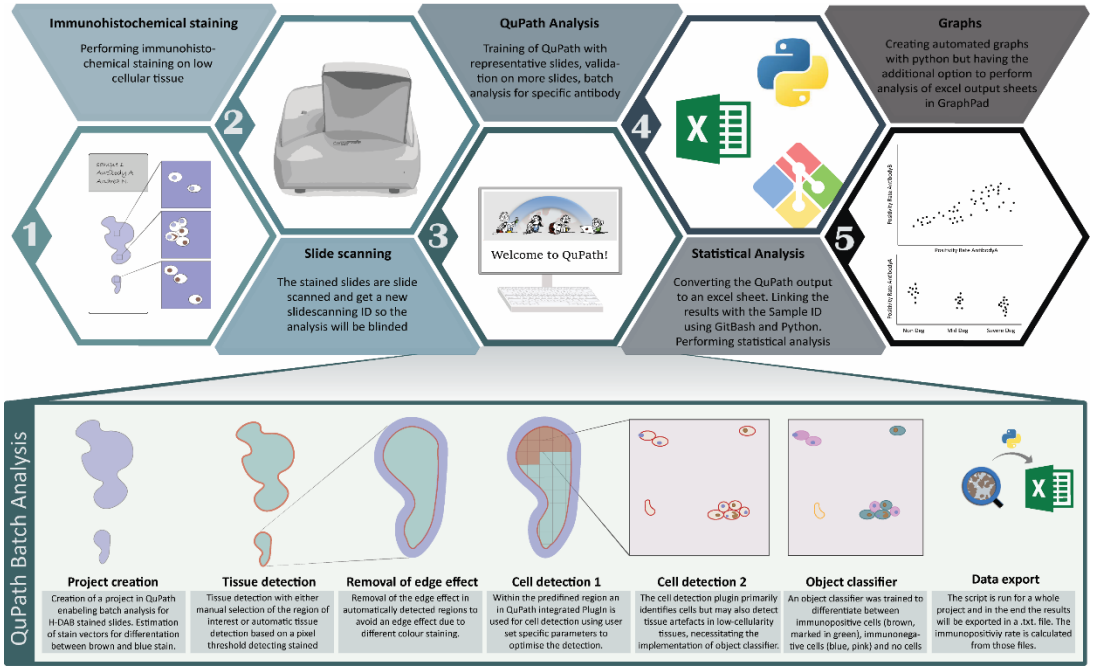

Figure 2.1 | Method pipeline

After immunohistochemical staining, the slides are scanned and analysed using QuPath before proceeding with statistical analysis and graph creation. Prior to running the QuPath batch analysis, the system undergoes training, during which the Cell Detection parameters are defined, an object classifier is trained, and regions of interest are selected (Figure 2). Batch analysis is then performed within a QuPath project based on the pre-defined parameters established during the initial training process During this analysis, cells within the regions of interest are detected according to the pre-set parameters and classified as either "positive cell," "negative cell," or "no cell." The batch process analyses all slides within the project and generates a folder containing text files with the results. In the subsequent step, a Python script consolidates these text files into a single Excel spreadsheet, which provides the positivity rate for each selected region of every slide. This consolidated data is then used for statistical analysis and visual representation.

Within QuPath, parameters such as deconvolution stain and cell detection were optimised before training a specific object classifier to distinguish between immunopositive and negative cells, as well as tissue artefacts (Figure 2.2). Batch analysis was performed in regions of interest to detect and classify cells, generating immunopositivity rates. The second step involved automatic annotation of QuPath results using a Python template workflow, which integrated data from QuPath, computed immunopositivity statistics, and produced visual outputs such as scatter plots and heatmaps for further

analysis. (2) Development of a user guide on GitBook: To ensure the process was accessible and user-friendly, a detailed step-by-step guide was hosted on GitBook [186], outlining how to perform the quantification and calculate the positivity rate for each antibody on the slides. The guide also included troubleshooting tips and best practices for batch analysis. (3) Feedback sessions and survey: The GitBook tutorial was distributed to six testers from four universities with diverse educational backgrounds. Feedback was collected through Zoom calls, where participants shared verbal comments on unclear sections, and through a written survey at the end of the process to gather overall impressions of the pipeline's clarity and usability. (4) Validation: Two evaluations were conducted to validate the pipeline. First, accuracy was validated by comparing semi-automatic quantification results with manual counting, for collagen type II staining and N-Cadherin staining revealing no significant differences ($p=0.783$, $p=0.386$) between the two methods while showing a strong correlation of the methods for both collagen type II staining ($r=0.09602$, $p<0.0001$) and N-cadherin staining ($r= 0.9044$, $p=0.0001$). Second, inter-rater correlation was assessed by having three raters independently analyse the same set of slides, with results demonstrating high consistency (Intraclass Correlation Coefficient, ICC = 0.853).

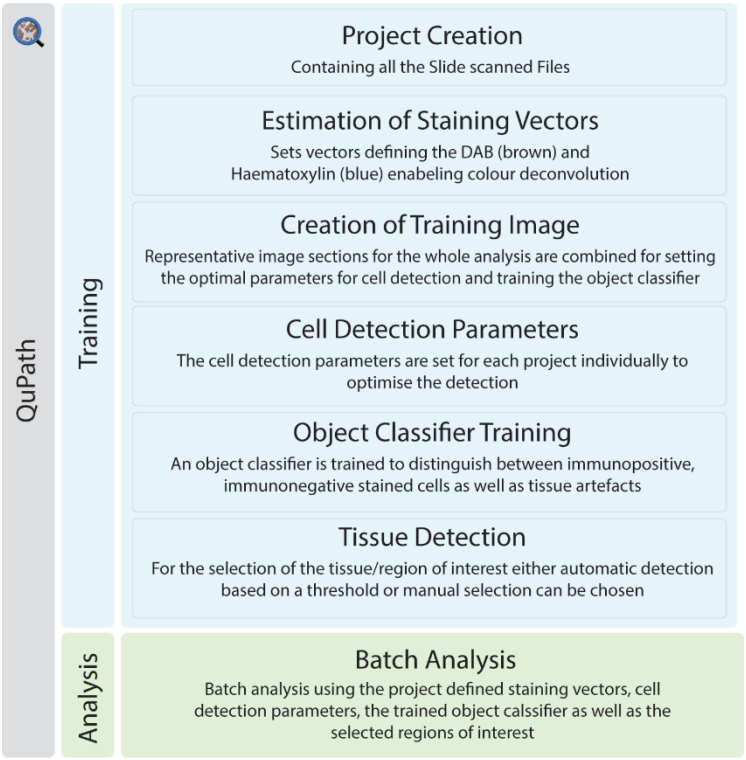

Figure 2.2| QuPath Training

To perform batch analysis with QuPath, the system must first be trained. This involves creating a training project within QuPath that includes all scanned slide files. Staining vectors are then estimated to define the DAB and haematoxylin components, enabling colour deconvolution. A representative training image containing various regions reflective of the entire project is selected for training cell detection and object classification. The QuPath Cell Detection plugin is run, and the parameters are adjusted accordingly. Detected cells are manually classified as "positive," "negative," or "no" cell. In a new project, regions of interest are selected, either manually by drawing or automatically using a pixel thresholding tool. Once the training process is complete, batch analysis is performed by applying the pre-determined parameters and values from the training phase to the batch script. This allows consistent analysis across all slides in the project.

2.2.2 SAMPLE PREPARATION AND DIGITALISATION

Frozen or formalin-fixed paraffin-embedded sections are suitable for immunohistochemical staining. We conducted DAB (3,3-Diaminobenzidine) staining according to the immunohistochemical analysis protocol outlined by Binch et al. [174]. Human Intervertebral disc tissue (IVD, Sheffield Research Ethics Committee, IRAS: 10266) and human cartilage (South Yorkshire and North Derbyshire Musculoskeletal BioBank (SYNDMB) REC: 20/SC/0144, 12182) were collected from Sheffield hospitals). The tissue was fixed in 10% (w/v) formalin (Leica, Milton Keynes, UK), embedded in paraffin wax, sectioned into 4 µm slices using a microtome, and mounted on positively charged slides. The sections were then de-waxed, rehydrated, and endogenous peroxidases were blocked before antigen retrieval. The cartilage samples were stained for the target antigen interleukin (IL)-1β (ab9722, 0.5 mg/mL, heat 1:100, Abcam, Cambridge, UK) whereas disc samples were stained for collagen type II (ab3092, enzyme 1:200, Abcam) and N-Cadherin (ab76011, 0.097 mg/mL, heat 1:100, Abcam). Heat antigen retrieval was performed using 0.05M Tris (pH 9.5), preheated to 60°C, and incubated for 5 minutes in a rice steamer. Enzyme antigen retrieval was performed with 0.1% (w/v) α-chymotrypsin (Sigma Aldrich, Poole, UK) in tris-buffer saline (TBS, 20 mmol/L Tris, 150 mmol/L NaCl, pH 7.5) containing 0.1% (w/v) $CaCl_2$ for 30 minutes at 37°C. Following antigen retrieval washing in TBS, non-specific antibody binding was blocked for 1 hour at room temperature. For IL-1β and N-Cadherin, 1% (w/v) bovine serum albumin (BSA) with 25% (v/v) rabbit serum (Sigma) in TBS was used. For collagen type II 1% (w/v) BSA with 25% (v/v) goat serum in TBS was utilised. Primary antibodies were applied to the slides overnight at 4°C. IL-1β was used diluted in TBS with 1% (w/v) BSA. IgG controls were used at equal protein concentrations to test for non-specific binding of the isotype. After overnight incubation, the sections were washed three times in TBS. Secondary antibodies goat anti rabbit (ab6720, 1:400, Abcam) or rabbit anti-mouse IgG (1:400, ab6727, Abcam) were then applied for 30 minutes at room temperature. Following three washes in TBS, Elite® ABC reagent (Vector Laboratories, Peterborough, UK) was added to the slides for 30 minutes at room temperature. After another three TBS washes, 0.65 mg/mL 3,3'-diaminobenzidine tetrahydrochloride (Sigma-Aldrich) containing 0.08% (v/v) H_2O_2 in TBS was added for 20 minutes. The sections were then washed in running tap water for 5 minutes. Nuclei were counterstained with haematoxylin for 20 seconds and blued under running tap water for 3 minutes. The slides were then dehydrated in graded ethanol, cleared in xylene, and mounted using Pertex® (Leica). Slides were scanned at 20x magnification using a slide scanner (PANNORAMIC® 250 Flash II DX, 3DHistech, Budapest, Hungary). Slide images scanned in MRXS (Mirax Scan) format (3D HISTECH), NDPI (NanoZoomer Digital Pathology Image) format (Hamamatsu, Shizuoka, Japan), CZI (Carl Zeiss Image) format (Zeiss, Oberkochen, Germany), and BIF (Bio-Format Image File) format (Ventana, Arizona US) are compatible with this analysis method. Each sample slide is automatically assigned a name during

the scanning process, referred to as ID_Slidescanning. This ID_Slidescanning remains unchanged throughout the analysis process to ensure unbiased analysis and is later linked to the sample ID in a subsequent step.

2.2.3 IMAGE PROCESSING IN QUPATH

2.2.3.1 Project Creation and Estimating of Staining Vectors.

A project was created for each stain analysed to allow for quantification of the whole project automatically, rather than for each scanned sample itself (Figure 2) [186].The nonspecific binding controls of the isotype were included in the analysis serving as accuracy measurement for the analysis. Staining analysis for each antibody was conducted in batches, accommodating between 1 and 100 samples per batch. The quantity of slides that can be processed in each batch relies on the computer's central processing unit (CPU) and random-access memory (RAM), rather than being determined by the capabilities of QuPath. A separate project is required in QuPath for each antibody and its corresponding regions, containing the relevant images. An algorithm, typically in the form of a simple Plug-in, is executed within QuPath to deconvolute the colour information captured by red-green-blue (RGB) cameras. This process estimates the staining vectors, digitally separating the stains to distinguish between the blue haematoxylin and the brown DAB stain [187]. If multiple regions are analysed within the same project, the staining vectors should be set for each region separately and saved accordingly.

2.2.3.2 Cell Detection and Object Classification

QuPath offers an automatic cell detection tool with adjustable parameters to fine-tune cell detection for each batch [188]. However, in the case of IVD tissue and cartilage, which exhibit a high extracellular matrix to cell ratio, the automatic distinction between positive and negative cells may not be applicable due to the detection of tissue artifacts. To address this issue, an alternative method is described. As a first step, regions within the tissue are selected to create a training image (Figure 2.2) [189] . The higher the number of regions included in the training image creation, the more accurate the training. If different components of a tissue are analysed within one sample, such as the nucleus pulposus and annulus fibrosus within the IVD, training images are created for each component. This is due to anatomical differences, which may result in differences in the optimal parameters for the cell detection. As a next step the cell detection plugin is ran on the training image (Figure 2.3). Parameters such as detection images, requested pixel size, background radius, median filter radius, sigma, minimum area of a nuclei, maximum area of a nuclei, threshold and maximal background intensity should be adjusted and optimised for each cell detection. Complete details of the influence of these parameters and proposed starting settings for different tissue types are provided in the Gitbook [190],

(Table 2.1). As previously mentioned, some tissue artefacts will be recognised within the software as cells. Thus, training an object classifier is required, which enables classifications of artefacts as “NoCell” and exclude them from the analysis. The Object classifier was manually trained to differentiate between immuno-positive cells (“PositiveCell”), immuno-negative cells (“NegativeCell”), and regions devoid of cells (“NoCell”) [191]. Once the precision of the Object classifier was high enough to result in correct measurement of immuno-positive and -negative cells, this was tested on sections and directly corrected, building the accuracy of the Object classifier (Figure 2.3).

Table 2.1 | Parameters for cell detection

Parameters	Description	
Detection images	Haematoxylin Optical Density	Detects nuclei based on the haematoxylin optical density, should only be chosen if DAB staining is not nuclear.
	Optical Density Sum	Detects nuclei based on the optical density sum, enables detection of nuclei that are masked with DAB, resulting not only in blue but also brown nuclei.
Requested pixel size	Under the Image tab, the pixel size of the slides can be checked, the pixel size should be chosen at the highest value still resulting in accurate results. The bigger the chosen value in pixel size the faster the analysis.	
Background radius	The background radius in QuPath represents the area surrounding each pixel that the software evaluates to estimate the local background intensity. This parameter is essential for accurately differentiating between the cells and tissue and the background. It correlates with the Threshold and should be set greater than the largest nuclei or set to 0 to turn it off. If it is turned off, the threshold needs to be increased	
Median filter radius	The median filter radius is a parameter that serves as noise reduction and smoothening tool. If the nuclei are segmented in the detection, it should be increased.	
Sigma	Sigma refers to the standard deviation parameter used in various filters (commonly Gaussian filter) playing a critical role in determining the smoothening extend of an image.	
Area	The minimum and maximum area of a nuclei is depended on the cell type.	
Threshold	Segments the image by separating objects of interest from the background in a binary way. It can help to remove the detection of false nuclei within the tissue. If a high number of cells is not detected, lowering the threshold is suggested.	
Max background intensity	Refers to the highest intensity value considered to be background. Can remove tissue fold and artefacts, as the background is darker than usual. The lower the value the more folds will be ignored. The Default value doesn’t show an effect.	

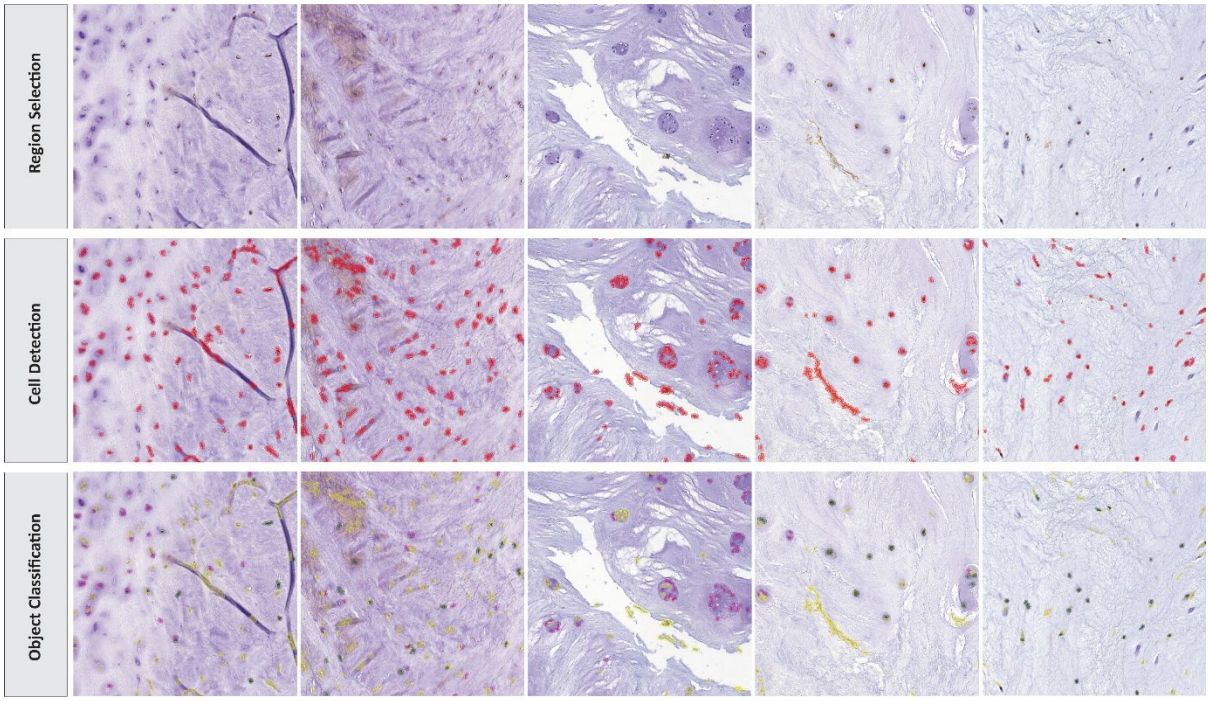

Figure 2.3 | Object classifier.

Three stages completed during object classifier: Region selection, cell detection and the object classification. Once a region of interest is selected the Cell Detection Plugin from QuPath can be run. Shown in red are the detection classified as cells. As the cellularity of the tissue is low and it is quite fibrous, some tissue artefacts are recognised and classified as cells. Once the object classifier, specifically trained for this project is ran the detected cells are classified as "PositiveCell" (green), "NegativeCell" (pink) and "NoCell" (yellow) enabling the calculation of a positivity rate as the ratio between positively stained cells and the total of negatively and positively stained cells.

2.2.3.3 Tissue Detection/Selection

Even though the training of the object classifier and the tissue detection could be run within the same project, we suggest creating a second project as it is easier to make corrections at the end if needed. Under annotations classification for the tissue detection were created, these may include for example nucleus pulposus, annulus fibrosus and cartilaginous endplate within IVD tissues, or cartilage and bone within osteochondral tissues [192]. If your sections contain multiple components the tissue detection needs to be performed manually. To do so the appropriate classification was selected, and regions of interest drawn round to be selected for inclusion in counting. If the whole sample consists of only one tissue type, automatic tissue detection can be used. Therefore, a thresholder was created ignoring all pixels above a certain threshold. If the staining within the project varies it was important to ensure all the slides are checked and adjusted either manually or by altering the thresholder. The thresholder was saved as "TissueDetection". If there were visible tissue folds, they were removed from the detection so that they did not result in false data.

2.2.3.4 Batch analysis

To perform the batch image analysis, a script was written which is freely available and downloadable [193,194]. The parameters for the estimation of the staining vectors and the parameters for the cell

detection were manually replaced for each project, creating a project specific script for each region and antibody of interest. Scripts were then run in a text file and automatically saved in a new results folder within the QuPath project folder. The text file contains information for each of the parent regions, e.g. cartilage, the detected objects and their type, e.g. cells, and the classification of the cells (Positive/Negative).

2.2.4 PROCESS SCANNING DATA - PYTHON PACKAGE

QuPath [177] is the gold standard software used in biological image analysis, even though it falls short in automating data processing. To export the results and represent statistical measurements for each sample, in this step-to-step tutorial it is employed the ProcessScanningData Python class [184],developed as a second step following the generation of files from the scanned images processed through the aforementioned method in QuPath.

The Python class, built up with specific libraries, such as NumPy [195] and MatLab [196], is customizable for MRXS, NDPI, CZI and BIF files. Merging these image-derived data with inventory files, organizing it into output files in either XLSX or CSV, depending on user's preference. Resulting in automatic and precise calculation of positivity rates and producing visualizations for every individual marker [185]. To unveil their potential biological correlation and significance, scatterplots and heatmaps were produced with Python libraries [197] based on standard statistical coefficients between positivity rates for different markers (e.g., Pearson, Spearman, and Kendall correlation coefficients)[198–200]. In the tutorial, rather than using the Python class directly, the focus is on a customizable workflow template tailored to user preferences, for example it is employed for MRXS files in this study. Notably, the dedicated Gitbook section aforementioned [184],provides a guide for users through the entire process, from software installation to the final generation of results.

2.2.4.1 Usage of Process Scanning Data in IHC Data analysis

The project has used the ready-to-use workflow and personalized it for analysing immunopositivity within histological images as defined by the previous method in QuPath. A step-by-step description from inputs to outputs is provided in the section 'Processing' in the tutorial [184].

Each input file is processed to extract detailed cellular and tissue-level metrics, such as object IDs, classifications (e.g., Positive/Negative Cell), region coordinates, and detailed nucleus and cell measurements (e.g., area, perimeter, circularity, and optical density of Haematoxylin and DAB stains), generated from the QuPath analysis. The processed data is then further analysed to calculate each marker's positivity rates. The results are compiled into structured output files (e.g., CSV or XLSX), which

include essential details such as Sample ID, Antibody, Image, Positive/Negative Class, and Positivity Rate. The final output consists of processed data files, or structured files (e.g., CSV or XLSX) containing detailed information on cell metrics, positivity rates, and respective metadata, and correlation analysis files, or visual representations (heatmaps and scatterplots) that illustrate the relationships between different biomarkers, providing a comprehensive and organized dataset that researchers can use for further analysis or publication. An additional merging step can be added to the pipeline, which has the aim to create a final spreadsheet, linking the donor/sample information with the positivity rates of the antibodies within specific regions, to end up with a single comprehensive file for further observation and analysis.

2.2.5 METHOD EVALUATION

2.2.5.1 Manual vs Semi-automatic Counting

A single evaluator assessed 28 IVD samples, 14 stained for Collagen type II and 14 stained for N-Cadherin, both manually and following the semi-automatic guidelines provided by QuPath. The correlation between the results obtained from the two methods was analysed using a paired t-test (p=0.05) in GraphPad Prism (Version 10.3.1 509, Windows, GraphPad Software, Boston, Massachusetts USA).

2.2.5.2 Interrater Variability

Three evaluators from the University of Sheffield conducted an analysis to determine the positivity rate for 17 IL-1β immunohistochemically stained slides, following the same pipeline. The results were analysed using the intraclass correlation coefficient (ICC) for single measures, based on a two-way mixed model with absolute agreement, in SPSS Statistics (IBM Corp. Released 2023. IBM SPSS Statistics for Windows, Version 29.0.2.0 Armonk, NY: IBM Corp). While two of the evaluators had prior experience with the pipeline, the third was performing the analysis and using QuPath for the first time. The evaluators varied in academic rank, comprising a PhD student, a postdoctoral researcher, and a professor.

2.2.5.3 Survey

A survey was conducted to assess the clarity of the GitBook documentation and the level of satisfaction with the results obtained using the semi-automatic QuPath method. Participants were contacted via email, either directly or through their principal investigator, and were provided with an information letter outlining the study and inviting them to participate in the evaluation of the semi-automatic quantification guide. After using the GitBook, participants assessed various aspects of the guide's usability using a Likert scale ranging from 1 (strong dissatisfaction) to 10 (strong satisfaction) (Appendix 1). A total of six participants from the University of Bern (Switzerland), Icahn School of Medicine at Mount Sinai (USA), the University of Arizona College of Medicine (USA), and the University of Sheffield (UK) participated in the survey. The group included two medical students, one PhD student, two postdoctoral researchers, and one professor.

2.3 RESULTS

2.3.1 MANUAL VS. SEMI-AUTOMATIC COUNTING

A two-tailed t-test revealed no significant differences between the semi-automatic QuPath method and manual counting for either collagen type II staining ($p = 0.783$) or N-cadherin staining ($p = 0.386$) (Figure 2.4A). For collagen type II staining, the mean difference between the methods was -0.6042, with a standard deviation (SD) of 8.039 and a 95% confidence interval of -5.245 to 4.038. Similarly, for N-cadherin staining, the mean difference was -2.651, with an SD of 11.02 and a 95% confidence interval of -9.016 to 3.71 (Figure 2.4A). The data pairing was highly effective, as indicated by strong correlation coefficients for both collagen type II ($r = 0.9602$, $p < 0.0001$) and N-cadherin ($r = 0.9044$, $p < 0.0001$), suggesting that the two methods are closely aligned. For both antibodies, the effect size was small ($R^2 = 0.006$ for collagen type II and $R^2 = 0.0586$ for N-cadherin), indicating minimal variability between the semi-automatic QuPath method and manual counting.

2.3.2 INTRACLASS CORRELATION COEFFICIENT BETWEEN 3 RATERS

The ICC for single measures was 0.853, with 95% confidence intervals ranging from 0.706 to 0.939. For average measures, the ICC was 0.946, with a 95% confidence interval between 0.878 and 0.979. The inter-item correlation matrix showed that rater 1 and rater 2 showed a correlation coefficient of 0.781, rater1 and rater3 0.892; rater 2 and rater 3 0.923 (Figure 2.4B). Differences in the positivity rates were traced back to differences in the QuPath training, the manual selection of the tissue but also the quality of the staining (Figure 2.4B). The slides showing bigger inter-rater variability showed a high background/noise staining with DAB, complicating the identification of cells and their classification (Figure 2.5).

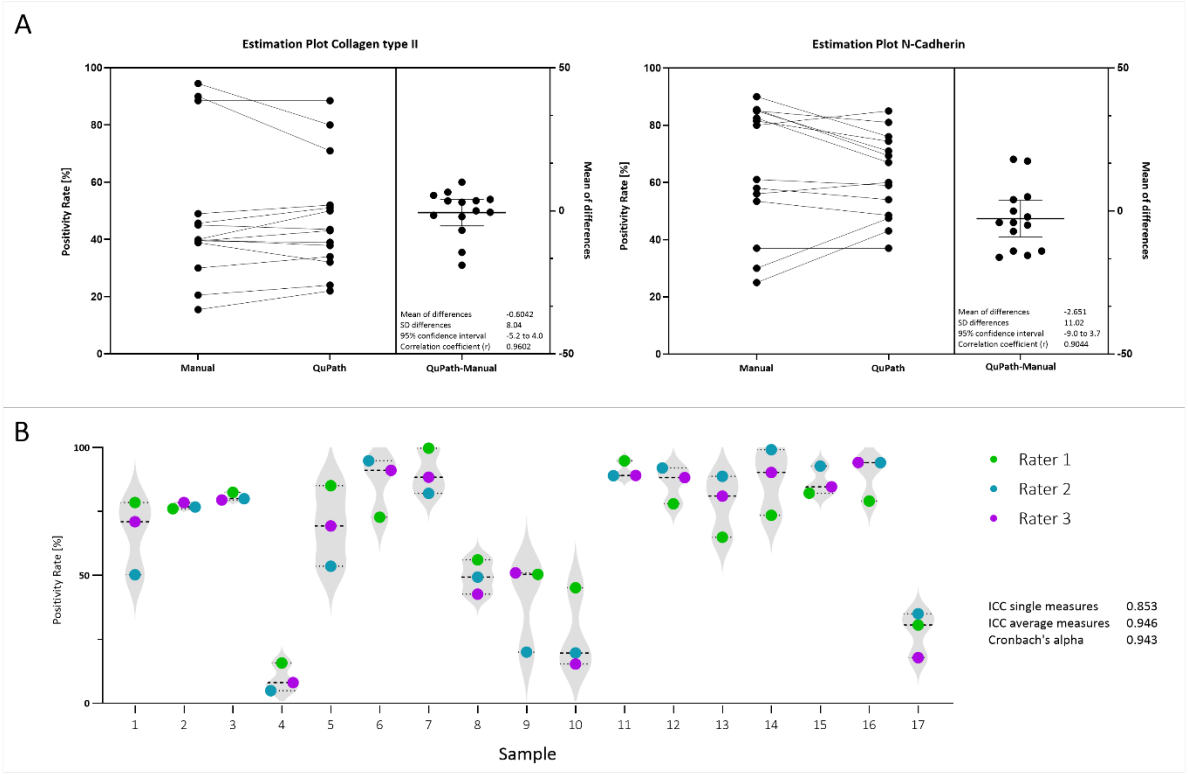

Figure 2.4 | Method evaluation

A Graph showing a paired t-test of the immunopositivity rates for immunohistochemically stained slides for Collagen type II (n=14) and N-Cadherin (n=14) analysed by a single rater manually and with QuPath. For the positivity rate of collagen type II staining the mean of differences between the manual and QuPath quantification was -0.604, with a standard deviation of 8.04. The correlation coefficient between the two methods was 0.960. For the positivity rate of N-Cadherin staining the mean of differences was -2.65 with a standard deviation of 11.02. The correlation coefficient between the manual and semi-automatic QuPath based quantification was 0.904. **B** Graph displaying the positivity rates obtained in 17 slides by 3 different Raters indicated by different colours. The positivity rates differed between the rates with a maximal standard deviation of 14.5 and a minimal standard deviation of 1. The Intraclass correlation for single measures was 0.853 and for average measures 0.946. Cronbach's alpha 0.943.

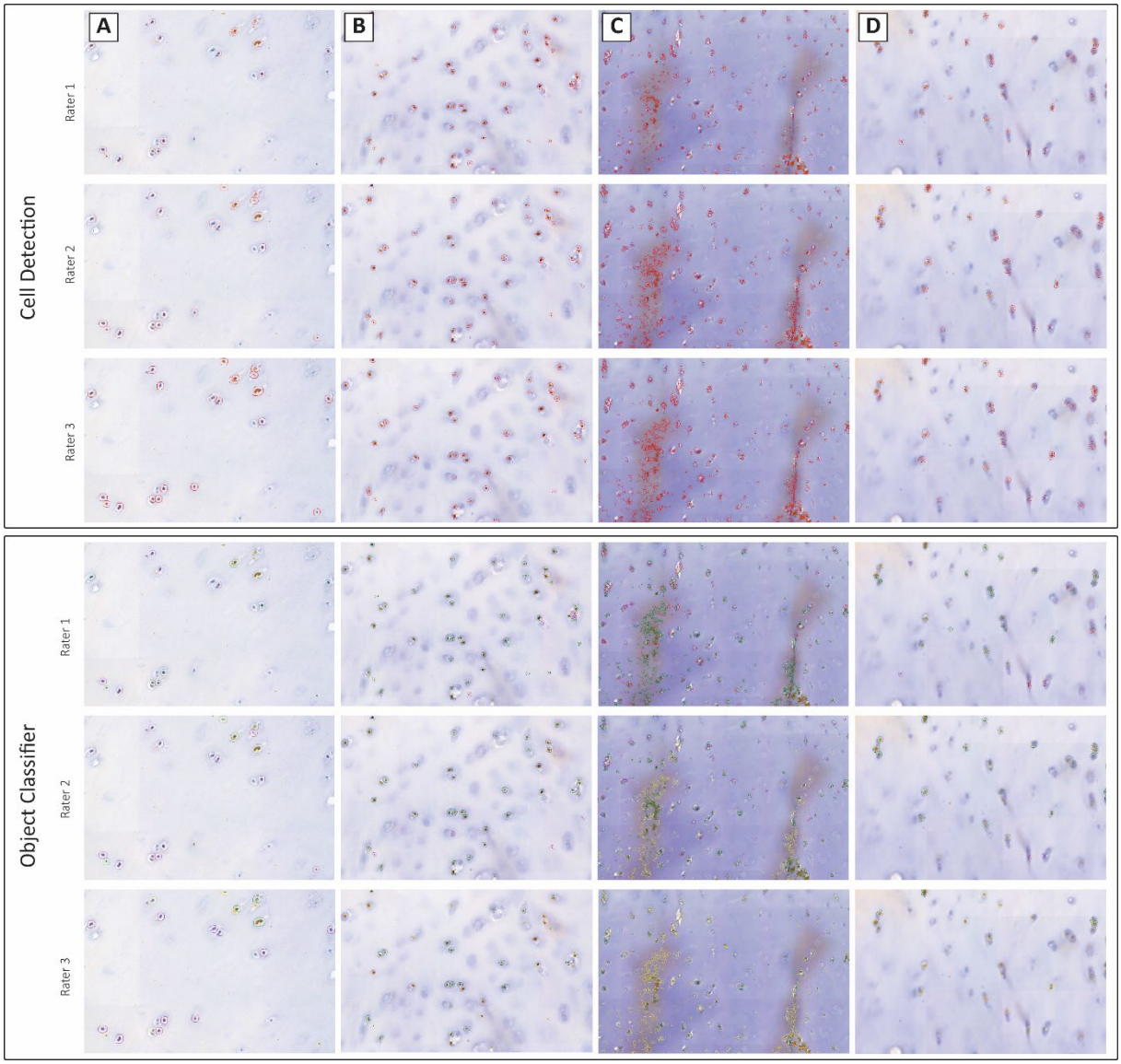

Figure 2.5 | Interrater differences in cell detection and object classification

The figure shows the differences between the different raters in parameters set for the cell detection as well as for the object classification. The top box shows the cell detection, detected objects are marked in red. The bottom box shows the object classification, displaying immunopositively classified cells in green, immune-negatively classified cells in pink and objects to ignore in yellow. Whilst images in row **A** and **B** show high similarities in the detection and classification images **C** and **D** differ highly. Rater 1 (row **C**) has not trained the classifier to exclude and ignore DAB debris within the stain whilst rater 2 partly ignores it and rater 3 fully. To acquire exact measurements rater 1 would therefore need to exclude mal stained regions from the analysis. Row **D** shows an image that is blurred. Rater 1 classifies blurred cells as positive and negative, whilst rater 3 classifies them as no cells and excludes them from the analysis.

2.3.3 SURVEY EVALUATION

Survey evaluation showed that five out of six participants had no prior experience with QuPath, while one had used it occasionally (Figure 2.6). Their familiarity with immunohistochemical analysis ranged from slightly familiar (n=2) to extremely familiar (n=2).

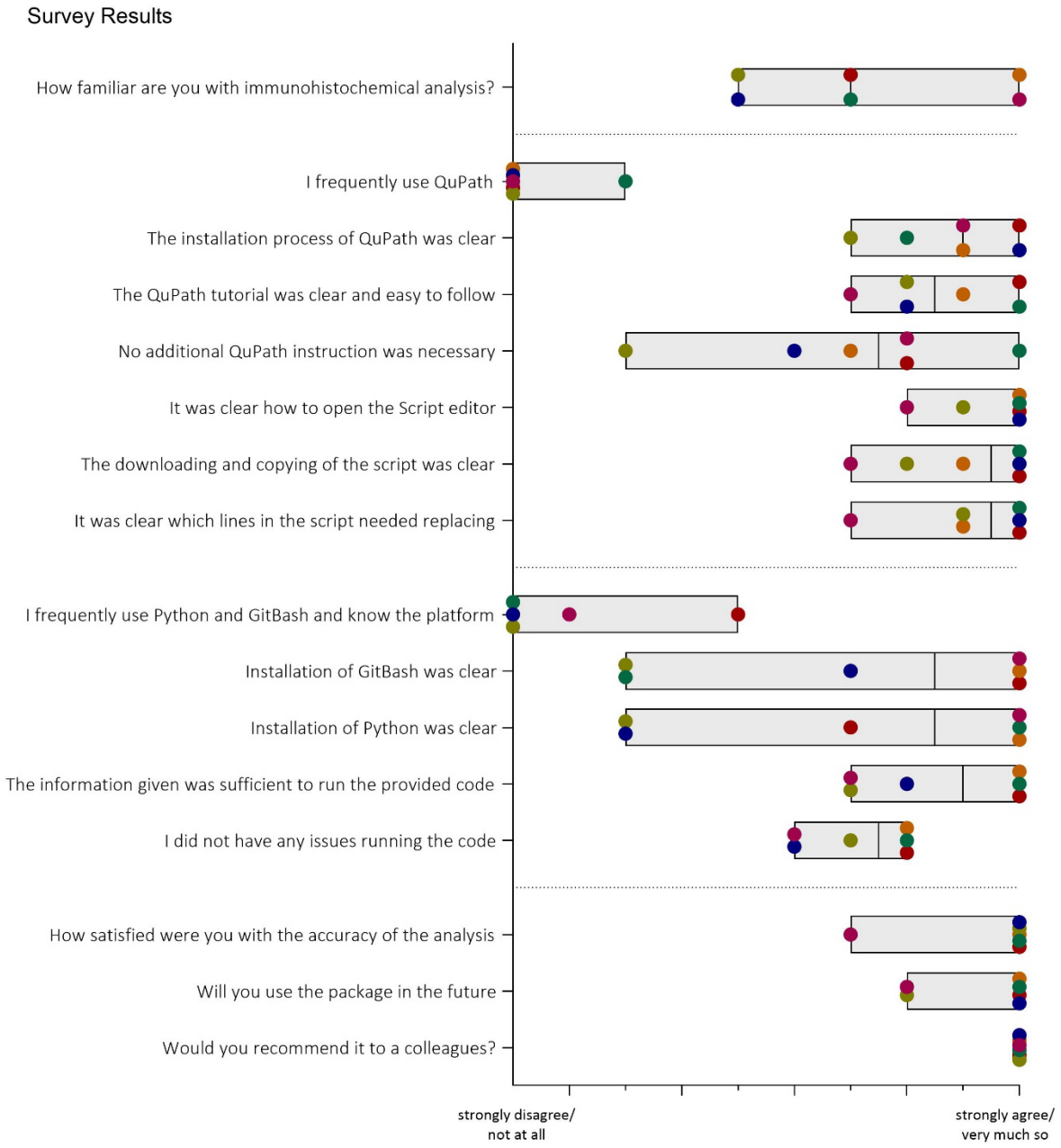

Figure 2.6 | Survey evaluation

Participants assessed various aspects of the guide's usability using a Likert scale ranging from 1 (strong dissatisfaction) to 10 (strong satisfaction). The different floating bars range from the minimal rated value to the maximum rated value showing the mean as a line. The different colours represent the different raters

The clarity of the installation process received an average score of 8.83/10, and the QuPath tutorial was rated at 8.67/10 (Figure 2.6). Some participants sought additional help from the official QuPath webpage, which was linked in the GitBook. The tasks of downloading, opening the script, accessing the script editor, and modifying the script lines were rated highly, with scores of 9/10, 9.5/10, and 9.17/10, respectively. Only two participants had prior experience with Python and GitBash, but the installation process was straightforward for Windows users. However, Mac users gave the process a lower rating of 3/10 (Figure 2.6).

The information provided in the GitBook was rated as sufficient for running the Python script (8.67/10), and participants were able to resolve issues independently while executing the code (Figure 2.6). One participant analysed 10-20 slides, four analysed 20-30 slides, and one participant analysed over 50 slides using the provided script. The tissues analysed included IVD tissue from humans and rats, as well as osteochondral tissue and cartilage. While one participant was somewhat satisfied with the detection and classification of cells in QuPath, five participants reported being extremely satisfied (Figure 2.6).

Regarding future use, two participants indicated they would probably use the package, and four participants stated they would definitely use it. All participants reported that they would recommend it to a friend or colleague (Figure 2.6).

2.4 DISCUSSION

IHC is a well-established and widely accepted method in both clinical and experimental medical sciences for assessing the localization and semi-quantification of proteins. However, the commonly used manual approach of counting 200 cells is limited by human fatigue, subjective interpretation of colour intensity, and regional bias, all of which reduce the accuracy and reproducibility of this method [201,202]. In response, several research fields [203], particularly in cancer research [175,176,178], have developed semi-automatic or fully automated methods, emphasizing the need for standardized, accurate, scalable, and reproducible evaluation techniques. However, these methods are not suitable for tissues like IVD components or cartilage due to morphological differences and the low cellularity of IVD tissue.

This study aimed to develop a guide for semi-automatic quantitative analysis of IHC-stained slides from low-cellularity tissues using QuPath. A fully automated pipeline was not implemented due to the region-dependent nature of cell detection parameters [204], which requires the system to be trained to differentiate between immunopositive and immunonegative cells, as well as tissue artifacts. The semi-automatic approach also allows for flexibility, enabling the use of various immunohistochemical

staining protocols. The focus of this study was specifically on cellular immunopositivity, and quantification of extracellular matrix (ECM) staining was beyond the scope of our analysis. While techniques such as area positivity measurements could be employed to assess ECM staining, quantifying staining intensity for DAB staining is not appropriate due to amplification of the staining and therefore potential inaccuracies in intensity or area-based quantification.

The method's evaluation involved comparing manual and semi-automatic results, along with calculating inter-rater correlation coefficients from the same sample set, following the established guideline. The high correlation between manual and semi-automatic counting confirmed the accuracy and highlighted the robustness of the semi-automatic QuPath method. Slight differences in positivity rates were attributed to the higher cell count and reduced regional bias in QuPath's quantification. The ICC analysis demonstrated strong reliability for both single raters and averaged measures, underscoring the robustness of the method. The single-measure ICC indicates good agreement among individual raters, while the higher ICC for average measures reflects excellent reliability when scores from multiple raters are averaged. This highlights the value of incorporating multiple raters to enhance the precision of measurements [205]. The inter-item correlation matrix further supports these findings, showing high consistency between raters, particularly between raters 2 and 3, while rater 1 exhibited slightly lower agreement with the others. These differences in inter-rater reliability were attributed to variations in QuPath training, manual tissue selection, and staining quality. Slides with greater inter-rater variability were characterised by high background staining with DAB, which made cell identification and classification more challenging. These findings highlight the importance of standardised training and stringent quality control during staining and image preparation to minimise variability. Overall, the results confirm that while individual raters achieve good reliability, averaging ratings from multiple raters substantially enhances the consistency and robustness of the method, particularly when addressing challenges posed by staining artefacts or subjective variability in tissue selection. The survey results indicated that the instructions provided in the GitBook were clear and sufficient for users to successfully follow and perform the analysis, yielding highly satisfactory outcomes in cell detection and classification. Importantly all participants stated they would recommend it to a colleague and most participants expressed an intention to use the method for future analyses.

Considering QuPath as the benchmark for biological image analysis, it lacks automation for tasks including calculating positivity rates and correlation coefficients, as well as generating customised visualisations [177]. A result, users have been forced to export the results and manually process the MRXS results, occasionally using other tools like Excel or R, which for non-experts can be time-consuming

and error prone. Additionally, manual data processing limits scalability when dealing with large datasets.

The ProcessScannigData class designed with a versatile hierarchical structure, offers a robust solution. It can serve as the foundation for a customised workflow, tailored on the type of scanned files the user's expertise level in bioinformatics. Accompanied by a template and an extended documentation, the instantiation of a customisable workflow is simplified for both experts and non-experts, producing ultimately the output files necessary for the assessment of immunopositivity and the generation of scatter plots and heatmaps [183,184] A standardised method like ProcessScanningData is crucial because it ensures reproducibility and portability across studies, avoiding the inconsistencies and arbitrary interpretations that can arise with manual curation. By eliminating subjective calculations, it provides a reliable framework for exploring relationships between different biomarkers, making it an invaluable resource for researchers working with histological data.

The proposed pipeline for semi-automatic counting demonstrates consistent and reliable performance, as evidenced by the high ICC values observed in this study. A comparison between manual and semi-automatic counting demonstrated that both methods yielded similar results, with the semi-automatic approach offering a more streamlined process by utilising predefined parameters. However, the dataset for this comparison was relatively small, and ICC analysis was not performed for manual counting by multiple raters, which limits the ability to fully evaluate variability in the manual method. While the semi-automatic pipeline reduces the need for repetitive, labour-intensive tasks, human input during the training phase and manual tissue selection can still introduce variability. Variability observed in slides with high background staining or poorly defined tissue regions highlights the importance of standardised training and quality control to ensure reliable results across both methods.

2.4.1 LIMITATIONS

The methods used in this analysis have several limitations. First, the requirement of a slide scanner limits accessibility, as not all laboratories may have the necessary equipment. Additionally, poor staining quality of the slides can negatively impact the accuracy of both manual and semi-automatic counting, as unclear or inconsistent staining makes cell identification more difficult. Furthermore, there is an element of subjectivity in the classification process, especially when training the semi-automatic system, which can introduce variability in results despite the use of standardised parameters. These factors must be considered when interpreting the data. Finally, during the evaluation process multiple users reported issues whilst using a Mac. CaseViewer used for the

visualisation of 3D HISTECH scanned slides is not available on Macs, however 3DHistech Panoramic viewer can be downloaded for free in the Appstore for iPads.

2.4.2 CONCLUSION

In conclusion, this study presents a semi-automatic pipeline for quantitative analysis of immunohistochemically stained slides, particularly for low-cellularity tissues such as intervertebral discs (IVD) and cartilage. The semi-automatic method developed using QuPath has been proposed to address key limitations of manual cell counting, such as human fatigue, subjective interpretation, and regional bias, with the aim to improve accuracy and reproducibility across groups following uptake. High inter-rater agreement and strong correlation with manual counting underscore the method's robustness and reliability. Furthermore, the ProcessScanningData class enhances the workflow by providing a scalable, customisable solution for processing large datasets, reducing manual intervention, and facilitating reproducible results. Despite minor reliance on manual training for cell detection, this approach represents a significant step forward in standardising IHC analysis, making it a valuable tool for researchers dealing with immunohistochemical data where the outcome measure of interest is cellular immunopositivity. The positive feedback from users, who reported high satisfaction and intent to continue using the method, with all survey participants reporting that they would recommend its use to colleagues, highlights its practical applicability and potential for widespread adoption in future studies.

ACKNOWLEDGEMENTS

We would like to extend our sincere thanks to Niklas Koehne (Icahn School of Medicine at Mount Sinai), Claire E. Pishko (Arizona College of Medicine-Tucson), Irina Heggli (Icahn School of Medicine at Mount Sinai), Paola Bermudez Lekerika (University of Bern), Lauren E. Lowe (University of Sheffield), Joseph Snuggs (University of Sheffield), and Grace McDemont (University of Sheffield) for their valuable participation in evaluating the semi-automatic quantification guide on GitBook. Their insightful feedback on its user-friendliness greatly contributed to refining the step-by-step instructions, enhancing both clarity and overall usability. We thank Mark Wilkinson, Diane Swift and South Yorkshire and North Derbyshire Musculoskeletal Biobank for providing surgical samples of osteochondral tissues, and the surgeons: Mr Ashley Cole, Mr Neil Chiverton, Mr Lee Breakwell, Mr Michael Athanassacopoulos, Mr Marcel Ivanov, Mr James Tomlinson, Miss Shreya Srinivas, Mr Surya Gandham and Mr Paul Brewer from Northern General Hospital, Sheffield Teaching Hospitals NHS Trust for supply

of human disc samples. Funding was received by the Marie Skłodowska Curie International Training Network (ITN) “disc4all” (https://disc4all.upf.edu, accessed on 9 April 2024) grant agreement #955735 (https://cordis.europa.eu/project/id/955735, accessed on 9 April 2024).

CHAPTER 3

INTRACELLULAR DETECTION OF *C. ACNES* AND *S. AUREUS* IN NON-HERNIATED HUMAN INTERVERTEBRAL DISCS: IMPLICATIONS FOR CATABOLIC SIGNALLING PATHWAYS

INTRACELLULAR DETECTION OF *C. ACNES* AND *S. AUREUS* IN NON-HERNIATED HUMAN INTERVERTEBRAL DISCS: IMPLICATIONS FOR CATABOLIC SIGNALLING PATHWAYS

Andrea Nüesch[1], Exarchos Kanelis[2,3], Leonidas. G. Alexopoulos[2,3], Benjamin Gantenbein[4,5], Melissa Lacey[6], Christine L Le Maitre[1]

[1]Division of Clinical Medicine, School of Medicine and Population Health, University of Sheffield, Sheffield, UK, [2]School of Mechanical Engineering, National Technical University of Athens, 9 Heroon Polytechniou Str, Zografou, 15780, Greece, [3]Protavio ltd, Science Park Demokritos, Agia Paraskevi, 15373, Greece, [4]Tissue Engineering for Orthopaedics & Mechanobiology, Bone & Joint Program, Department for BioMedical Research (DBMR) of the Faculty of Medicine of the University of Bern, University of Bern, Murtenstrasse 35, CH-3008 Bern, Switzerland, [5] Department of Orthopaedic Surgery and Traumatology, Inselspital, Bern University Hospital, Medical Faculty, University of Bern, Freiburgstrasse 3, CH-3010 Bern, Switzerland, [6]School of Biosciences and Chemistry, Sheffield Hallam University, Sheffield, UK

This manuscript is in preparation for submission.

AUTHOR CONTRIBUTIONS

AN, ML and CLLM performed the conceptualisation. AN ran the main experiments, wrote the main text, performed the data analysis and prepared the visualisation and graphs. EK & AN performed Luminex measurements. CLLM, ML, BG and LA provided intellectual input, reviewed and edited the manuscript and sourced funding. All authors read and approved the manuscript.

DETAILED AUTHOR CONTRIBUTION

I wrote the manuscript, conducted the experiments, and performed the data analysis and visualisation. Secretome samples from cells in 2D and 3D exposed to bacterial cell wall components were collected in Sheffield were sent to Protavio, a collaborator in Greece, where Exarchos Kanelis carried out a Luminex assay. However, I conducted the data analysis in Sheffield. I performed the Luminex assay for the samples collected from the experiment were we combined bacterial stimulation with inhibitors. Christine Le Maitre reviewed the manuscript, providing valuable feedback on the text, graphs, and visualisation. Exarchos Kanelis also performed the Luminex assay and reviewed the manuscript, while Mel Lacey and Benjamin Gantenbein provided additional review.

CONFLICT OF INTEREST

Exarchos Kanelis and Leonidas Alexopoulos work at Protavio.

ABSTRACT

The existence of a disc microbiome and the potential for disc infection have sparked considerable debate within the spine research community, challenging the long-standing belief that the intervertebral disc (IVD) is a sterile environment. Despite advancements in microbial culture and next-generation sequencing (NGS), these methods have struggled to rule out perioperative contamination. This study examined the detection of bacteria within non-herniated IVDs using immunohistochemistry to determine if bacterial presence indicated *in vivo* colonisation rather than contamination. The survival of bacteria under conditions mimicking the harsh IVD environment was assessed to gauge potential growth rates *in vivo*. Following confirmation of bacterial presence, correlations with catabolic factors were analysed, alongside the *in vitro* effects of bacterial exposure. Human nucleus pulposus (NP) cells were treated with bacterial cell membrane components in both monolayer and 3D cultures to evaluate their impact on the cellular secretome, analysed via Luminex assay. Co-culture studies tracked bacterial internalisation, while NP cells were exposed to peptidoglycans or co-cultured with what is believed to be physiologically relevant MOIs of *S. aureus* or *C. acnes* to explore the activation of intracellular signalling pathways. Immunohistochemical staining showed significant correlations between *C. acnes* and MMP-3, GSDMD, and NOD2, indicating an active role of NP cells in immune surveillance. The involvement of NOD2 points to previously unrecognised intracellular pathways contributing to bacterial detection and subsequent inflammatory responses. This study highlights the complex interplay of various receptors and pathways in the disc's immune response to bacteria, suggesting avenues for targeted therapeutic strategies for disc-related conditions.

3.1 INTRODUCTION

The intervertebral disc (IVD) is a key structural component of the spine, responsible for maintaining flexibility and facilitating the distribution of mechanical loads across vertebral segments [206]. Degeneration of the IVD is strongly associated with low back pain (LBP), a condition that stands as the leading cause of disability worldwide. In 2020, it was estimated that LBP affected approximately 619 million individuals, particularly affecting females [207]. Traditionally, the avascular nature of the IVD led to the assumption that it was a sterile environment. This long-held view was first challenged in 2001, when Stirling *et al*. identified anaerobic bacteria, particularly *Cutibacterium acnes* (Moore *et al.* 1963)[101] , in the disc tissue of patients suffering from sciatica [208]. Since this discovery, the potential role of bacterial infection within the disc, as well as the presence of a disc-specific microbiome, has become a topic of intense debate within the spine research community. In particular, the relationship between bacterial colonisation and Modic changes, which are vertebral bone marrow lesions observable on MRI, has been of significant interest, as bacterial colonisation has been suggested as a potential aetiology [138].

With improvements in microbiological detection methods, particularly next-generation sequencing (NGS), it has become possible to explore the microbiome in low-biomass environments such as the IVD [138]. Recent studies suggest that the disc may harbour its unique microbiome [138,147]. However, data indicating an IVD microbiome has been viewed cautiously due to the vulnerability to perioperative contamination, raising questions about whether detected bacteria truly exist *in vivo* within the disc or are artifacts of the surgical procedure. Among the bacteria frequently identified within the disc, *C. acnes* has gained the most attention to date [125–127,132,209–215]. *C. acnes* is a Gram-positive, aerotolerant anaerobic bacterium and is a commensal that colonises the skin, oral cavity, gastrointestinal tract, and genitourinary tract [216,217]. However, it is also known to act as an opportunistic pathogen, particularly in skin and soft tissue infections, as well as infections associated with medical devices [218,219]. Since its initial detection in IVD tissue, *C. acnes* has been the focus of numerous studies, alongside other microbes such as coagulase-negative Staphylococci and *Staphylococcus aureus* (Jevons *et al.* 1963) [220], which have also been detected in disc samples [147].

Recent research has focused on the presence of bacteria within the IVD, and the potential signalling pathways activated by bacterial stimulation. Molecular pattern recognition is a fundamental mechanism in innate immunity and tissue repair, mediated by pattern recognition receptors (PRRs) that detect danger signals from damage-associated molecular patterns (DAMPs) and pathogen-associated molecular patterns (PAMPs). The critical PRR families in humans include retinoic acid-inducible gene I (RIG-I)-like receptors (RLRs), nucleotide oligomerisation domain (NOD)-like receptors

(NLRs), and toll-like receptors (TLRs). While RLRs primarily detect viral infections [221], certain NLRs and TLRs are responsible for recognising bacterial components such as lipopolysaccharide (LPS), lipoteichoic acid (LTA), and peptidoglycan (PGN) fragments [222,223]. TLRs have been identified in human IVD cells [151,224]. TLR2, a membrane-bound receptor, forms heterodimers with either TLR1 or TLR6 and has been shown to upregulate catabolic factor expression when stimulated by bacterial cell wall components from Gram-positive bacteria, including *C. acnes* [225]. Similarly, the TLR4 homodimer is activated by Gram-negative bacteria and fragments such as LPS [226]. Within the NLR family, NLR family pyrin domain containing 3 (NLRP3) has been detected in IVD cells and is implicated in *C. acnes*-induced pyroptosis in nucleus pulposus (NP) cells [168]. However, the presence of NOD2, an intracellular sensor of PGN-derived small peptides [227], has not yet been investigated in the context of IVDs.

This study aimed to investigate the presence of bacteria within non-herniated human IVDs and differentiate between perioperative contamination and authentic *in vivo* bacterial colonisation. Additionally, the study sought to examine the correlations between PRRs, catabolic factors, and bacterial presence. Furthermore, bacterial growth was monitored in conditions mimicking the IVD microenvironment, and the effects of bacterial exposure on human disc cells were explored, with a focus on the signalling pathways activated in response to such exposure.

3.2 METHODS

3.2.1 EXPERIMENTAL DESIGN

This study initially investigated whether bacteria could be detected within non-herniated human IVDs using immunohistochemistry to enable localisation of bacteria and determine whether bacterial presence was likely due to contamination alone or represented *in vivo* disc bacteria (Figure 3.1). Bacterial growth was also assessed under conditions mimicking the harsh disc environment to monitor their survival. The ability of bacteria to survive and multiply within conditions which mimicked the harsh disc environment was undertaken to determine potential growth rates *in vivo.* Following confirmation of bacterial presence within the disc, correlation with catabolic factors and the ability of bacteria to multiply within conditions which mimicked the disc environment, the potential direct effects of bacteria were investigated *in vitro.* Initial studies utilised human nucleus pulposus (NP) cells in monolayer and subsequently in a 3D culture system treated with bacterial cell membrane components to determine their influence on cellular secretome, which was analysed using a Luminex

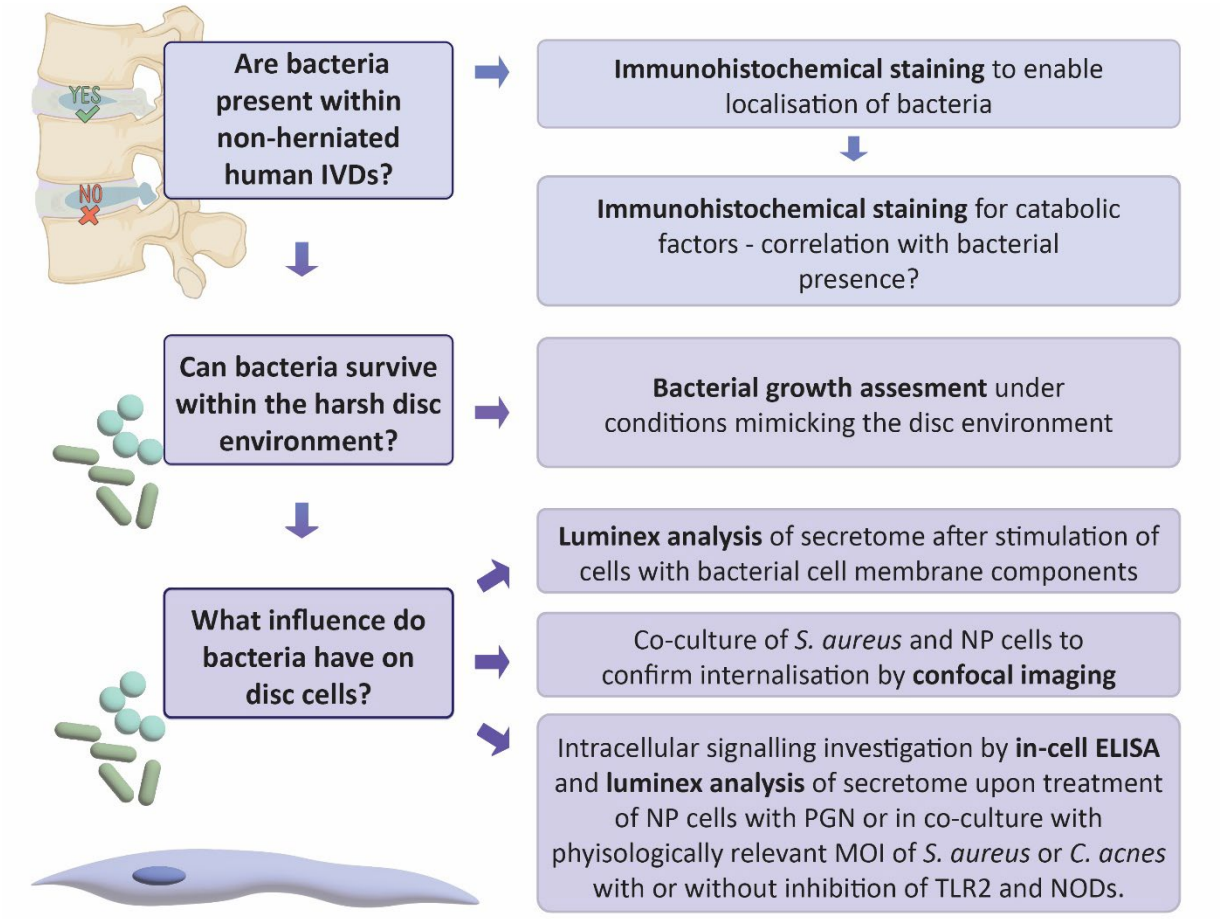

Figure 3.1 | Project overview

Addressing the main questions whether bacteria are present within non-herniated human IVDs and what their potential influence is with the methods stated on the right-hand side.

assay. Co-culture studies were then utilised to determine time course of bacterial internalisation into human NP cells. Finally, NP cells were treated with PGNs or in co-culture with physiologically relevant MOI of *S. aureus* or *C. acnes* to determine activation of intracellular signalling pathways and modulation of secretome. These cultures were performed with and without the presence of inhibitors of TLR2 and NOD receptors to determine potential receptor-mediated responses.

3.2.2 TISSUE COLLECTION

Human IVD tissue was collected from patients who gave their consent during spinal surgery at Northern General Hospital or Claremont Hospital in Sheffield (UK). Local ethics approval was given for this work by Sheffield Research Ethics Committee (09/H1308/70) (IRAS approval: 10226). The tissue was placed into 30 ml low glucose (1.0 g/L) Dulbecco's Modified Eagle Medium DMEM (LG-DMEM, Invitrogen 31600-083, Paisley, UK) supplemented with 1% Penicillin/ Streptomycin (P/S, Invitrogen, 15070-063) and 25 µg/ml Amphotericin B (Sigma, A2942, Dorste, Gillingham, UK) at 4 degrees at surgery, and transported under sterile conditions to the laboratory. As a first step the tissue was washed twice in sterile phosphate buffered saline (PBS, OXOID BR0014G, Thermo Fisher Scientific, Loughborough, UK) before splitting the tissue into annulus fibrosus (AF), cartilaginous endplate (CEP), and NP tissues. For cell isolation solely NP tissue was used in this study whereas parts from all tissue components (where available), were fixed in 10 % (w/v) formalin (Leica, Milton Keynes, UK), processed, embedded in paraffin wax to perform histological grading of degeneration and immunohistochemical staining.

3.2.3 HAEMATOXYLIN AND EOSIN STAINING AND GRADING FOR STATE OF DEGENERATION

Sections were cut with a microtome at a thickness of 4 µm and mounted on positively charged slides (Superfrost Plus, Epredia, Runcorn UK). Sections were dewaxed in sub-X (Leica Microsystems) 3x 5 minutes and hydrated in industrial methylated spirit (IMS, 3x5 minutes). Sections were the stained with Harris's haematoxylin (Surgipath Europe Ltd) for 5 minutes and blued for 3 minutes under running tap water. For counterstaining alcoholic eosin (Leica Microsystems) was applied for 2 minutes. After dehydration in IMS and clearing in sub-X the slides were mounted using Pertex® (Leica Microsystems). Grading was performed following the standardised histopathology scoring system for human IVD degeneration [228]. For samples consisting of both NP and AF, the average of the two scores was taken as degenerative score. CEPs were excluded from the analysis as they were observed in low numbers of samples.

3.2.4 IMMUNOHISTOCHEMICAL STAINING (IHC)

Human IVD specimens were fixed in 10 % (w/v) formalin for 48 hours up to a week and embedded in paraffin wax. Sections were cut with a microtome at a thickness of 4 µm and mounted on positively charged slides. Immunohistochemical staining was performed as previously published [229]. The sections were de-waxed and rehydrated and endogenous peroxidases were blocked for 60 minutes in 100% IMS containing 3% (v/v) hydrogen peroxide (Sigma Aldrich) and 0.06% (v/v) concentrated HCl. Antigen retrieval depended on antibody (Table 3.1) and consisted either of no antigen retrieval, enzyme antigen retrieval [0.1% w/v α-chymotrypsin (Sigma Aldrich, Poole, UK) in tris-buffer saline (TBS) (20 mmol/L Tris, 150 mmol/L NaCl pH7.5) containing 0.1 % w/v $CaCl_2$ for 30 minutes at 37°C] or heat antigen retrieval [0.05M Tris, pH 9.5 preheated on automatic cook mode prior to 5 minutes incubation of samples within a rice steamer on warm (ASAB, AS-40979, UK)]. Following antigen retrieval, the sections were washed in TBS and non-specific antibody binding was blocked (Table 3.1) for 1 hour at room temperature in 1% (w/v) bovine serum albumin (BSA) containing 25% (v/v) normal serum in TBS. Primary antibodies (Table 3.1) were applied to the slides overnight at 4 degrees diluted in TBS containing 1% (w/v) BSA. Simultaneously IgG controls in place of the primary antibodies were used at equal protein concentrations to test for non-specific binding of the isotype. Following the overnight incubation, the sections were washed with TBS three times prior to the application of the secondary antibodies at room temperature for 30 minutes followed by three more TBS washes, before applying Elite®ABC reagent (Vector, Laboratories, Peterborough, UK) to the slides for 30 minutes. After another 3 TBS washes 0.65 mg/mL 3,3'-diaminobenzides tetrahydrochloride (DAB, Sigma-Aldirch) containing 0.08% (v/v) H_2O_2 in TBS was added for 20 minutes, prior to washes in running tap water for 5 minutes. Counterstaining of the nuclei was performed with Haematoxylin (Gill's Haematoxylin

Table 3.1 | Target antibodies used for immunohistochemical staining

Primary Antibody	Clonality	Stock conc. [mg/ml]	Dilution	Antigen Retrieval	Secondary Antibody	Normal Serum
ADAMTS4 (ab185722)	rabbit polyclonal	2.3	1:200	none	Goat anti rabbit (ab6720)	Goat
C acnes (D371-3)	mouse monoclonal	1	1:100	enzyme	Rabbit anti mouse (ab6727)	Rabbit
G43J (ab267414)	mouse monoclonal	0.1	1:50	enzyme	Rabbit anti mouse (ab6727)	Rabbit
GSDMD (ab210070)	rabbit monoclonal	0.78	1:100	heat	Goat anti rabbit (ab6720)	Goat
IL1b (AB_223567)	mouse monoclonal	1	1:400	none	Rabbit anti mouse (ab6727)	Rabbit
MMP3 (ab53015)	rabbit polyclonal	1	1:400	enzyme	Goat anti rabbit (ab6720)	Goat
NLRP3 (ab263899)	rabbit monoclonal	0.58	1:100	none	Goat anti rabbit (ab6720)	Goat
NOD2 (ab31488)	mouse monoclonal	1	1:600	heat	Rabbit anti mouse (ab6727)	Rabbit
S aureus (AB_1087481)	mouse monoclonal	2	1:100	enzyme	Rabbit anti mouse (ab6727)	Rabbit
TLR2 (ab226913)	rabbit polyclonal	1	1:500	enzyme	Goat anti rabbit (ab6720)	Goat
TLR4 (ab22048)	mouse monoclonal	1	1:100	heat	Rabbit anti mouse (ab6727)	Rabbit

GHS232, Sigma, Doset, UK) for 20 seconds and blued for 3 minutes under running tap water. After dehydration in graded ethanol and clearing in xylene the slides were mounted using Pertex®. Slides were scanned at 20x and 40x magnification using a slidescanner (PANNORAMIC® 250 Flash II DX, 3DHistech) and representative images included to highlight immunohistochemical staining. Image analysis was performed using the semi-automatic quantification protocol described in chapter 2.

3.2.5 ISOLATION AND EXPANSION OF HUMAN NUCLEUS PULPOSUS (NP) CELLS

Cell isolation was performed using the standardised protocol as previously published [230]. Briefly, upon washing with PBS, the tissue was transferred into a 50 ml falcon tube containing 20 ml of Collagenase type II (285.00 units/mg, 0.05 mg/ml, Invitrogen: 17101-015) and incubated (37°C, 5% CO_2, 21% O_2) for 4 hours on an orbital shaker. The released cells were filtered through a 70 µm cell strainer, counted, and plated at a seeding concentration of 10'000 cells/cm^2. Culture media composed of high glucose (4.5 g/L) DMEM Medium (HG-DMEM, Invitrogen: 10569010 HG) supplemented with 10% (v/v) heat-inactivated foetal calf serum (FCS, LifeTechnologies, Paisley, UK), 1% P/S, 1% L-Glutamine (Invitrogen: 25030-024), 2.5 µg/ml Amphotericin B and 25µg/ml L-ascorbic acid 2-Phosphate (AA, Sigma, A5960) was added and changed 3 times per week. At 80% confluence cells were detached using Trypsin-EDTA (Invitrogen, 25300-062) and passaged 1:3. Upon passage 2, cells were used for experiments in monolayer or resuspended in 1.2% alginate to enable re-differentiation to NP phenotype.

3.2.6 ENCAPSULATION OF NP CELLS IN ALGINATE

Following trypsinisation, cell suspensions were centrifuged at 400 g for 4 minutes. The cell pellet was then resuspended in culture media and counted using a NucleoCounter® NC-2000™. Following further centrifugation at 400 g, cells were resuspended at 1.2 % medium viscosity sodium alginate (Sigma A2033) in 0.15 M sodium chloride (NaCl) at $4x10^6$ cells/ml density. The resulting cell suspension was passed through a 21-gauge needle into a 24 well plates containing 200 mM calcium chloride ($CaCl_2$), six beads per well. Beads were incubated for 10 min at 37°C in 200mM $CaCl_2$, followed by 2 washes of 0.15 M NaCl and media. Two millilitres of complete low glucose (LG, 1g/L) -culture media: LG DMEM, supplemented with 1% insulin transferrin selenium-x (ITS-x, Invitrogen, 51500-056), 1% P/S, 1% L-Glutamine, 2.5 µg/ml Amphotericin B, 25µg/ml AA, 40 µg/ml L-Proline and 1.25 mg/ml Albumax were added [230]. Cultures were maintained for 2 weeks at 37°C under physioxia conditions (5%O_2, 5%CO_2) to regain *in vivo* phenotype.

3.2.7 BACTERIAL CULTURES

Staphylococcus aureus SH1000 a derivate of the 8325-4 strain and *Cutibacterium acnes* (NCTC 737, Culture Collection UK Health Security Agency, Salisbury, UK) were used for this study. *S. aureus* was grown on Mueller Hinton agar (70191, Merck, Dorset, UK) plates at 37 degrees and 21% O_2 overnight. *C. acnes* was grown at 37 degrees in an anaerobic chamber on agar plates for 1 week. Liquid cultures were grown under 5% O_2 by adding one colony-forming unit (CFU) to 4 ml of complete LG media. *S. aureus* was used after 16 hours of culture, whilst *C. acnes* was cultured for 48 hours prior to use.

3.2.8 BACTERIAL GROWTH

Bacterial growth was measured at 5% O_2 within 3 different culture media. Mueller Hinton Broth was used as positive control, whilst complete LG-culture media at an osmolarity of 350 mOsm/Kg and 450 mOsm/Kg were used to represent the disc environment [231]. An initial liquid culture in the respective culture media was diluted to have an optical density of 0.1 at a wavelength of 600 nm. The suspended bacteria were then seeded into a 96-well plate, and the optical density was measured with the stratus kinetic microplate reader (Cerillo, Charlottesville, VA 22902, USA). A second 96-well plate was used to prepare serial dilution to count CFU every hour for *S. aureus* and twice a day for *C. acnes*

3.2.9 CO-CULTURE OF HUMAN NP CELLS AND *S. AUREUS*

Human NP cells were seeded into chamber slides at $0.3x10^5$ cells/well in LG-culture media. Cells were left to attach overnight at 37°C, 5% CO_2, 21% O_2, whilst *S. aureus* was grown in a liquid culture in LG-culture media overnight. Two hours before usage, NADA green (0.5mM, Cat 6648, TOCRIS) was supplemented with the media labelling the peptidoglycans in the live bacteria. Fresh media, supplemented with *S. aureus* at an MOI 1:100 (bacteria: cells) was added to the cell culture and incubated for 1 hour prior to fixation in 10 % (w/v) formalin for 20 minutes. Cells were then stained with Phalloidin (A12381, Thermo Fisher) for 30 minutes prior to washing with PBS and mounting with gold antifade mountant with DNA stain DAPI (P36931, Thermo Fisher). Imaging was performed on Zeiss LSM 800 confocal microscope (Carl Zeiss Microscopy GmbH, Oberkochen, Germany).

3.2.10 STIMULATION WITH PEPTIDOGLYCANS (PGN) AND LIPOPOLYSACCHARIDES (LPS)

Following trypsinisation and counting, cells were seeded into a 12 well plate at a concentration of $0.5x10^6$ cells/well for the monolayer culture (Appendix 3). Cultures were held at 37°C, 5% CO_2, 21% O_2. After an initial settling period for 24 hours in complete LG media, the cells were treated for 48 hours with different concentrations (0-50 µg/ml) of peptidoglycans (PGN) and lipopolysaccharides (LPS) respectively. Media was collected following treatment for protein analysis with Luminex immunoassay. Cells in alginate were cultured under physioxia conditions (5% O_2, 5% CO_2) complete LG media for 2 weeks prior to the treatment with complete LG media supplemented with different concentrations of PGN (0-50 µg/ml) for 72 hours respectively. Cells were permeabilised with 0.1% Triton X-100 in PBS for 3 minutes and stained with Phalloidin for 30 minutes.

3.2.11 INHIBITION OF NOD AND TLR2 AND STIMULATION WITH PGN, *S. AUREUS* AND *C. ACNES*

Cells from 3 human donors (Appendix 3) at passage 2 were trypsinised and counted and seeded into 96 well plates at a density of 15'000 cells per well, and 48 well plates at a seeding density of 30'000 cells per well. Cells were left to attach overnight in complete LG media under physioxia conditions (5% O_2, 5% CO_2). Cells were treated with the inhibitors for nucleotide oligomerisation domain in 1 (NODin1, 10 µM, Selleckechem, S0004), toll like receptor 2 (TLR2, 50 µM, Selleckchem, S6597) and a combination of the two for 24 hours prior to treatment. Optimisation of the concentrations was performed by measuring the metabolic activity using a resazurin reduction assay to confirm no detrimental effects on viability. Cells were incubated for two hours at 37°C and resazurin sodium salt (119,4 µM, Sigma Aldrich, R7017) in media before absorbance was measured at excitation 560 nm and emission 590 nm. The treatment groups were stimulation with PGN (50 µg/ml) for 48 hours or bacterial stimulation with *C. acnes* or *S. aureus* SH1000 with and without the presence of inhibitors. Bacteria were added for 2 hours with and without the presence of inhibitors at a ratio of 1 bacterium to 100 cells (MOI 1:100) before washing non-internalised bacteria with PBS and adding fresh media supplemented with the inhibitors to culture the cells for a further 48 hours. Media was collected to perform Luminex analysis.

3.2.12 CELL BASED PHOSPHORYLATION MEASUREMENTS

Protein phosphorylation was measured for c-Jun-N-terminal Kinase (JNK, CBEL-JNK-1, RayBiotech, GA 30092, US) p38 mitogen-activated protein kinase (p38, CBEL-P38, RayBiotech), extracellular signal-regulated kinase (ERK, CBEL-ERK, RayBiotech) and nuclear factor kappa B p65 (NFkB, FBCAB0073, Assay Genie, Dublin Ireland) as per manufacturer's instructions. As previously stated, cells were seeded into the 96 well-plates and incubated overnight before applying inhibition followed by the treatment. After

2 hours of treatment, following the manufacturer's instructions, the cell culture medium was discarded and washed 3 times with the provided wash buffer before fixing the cells for 20 minutes. Following the manufacturer's instructions for kits purchased from Raybiotech (CBEL-JNK-1, CBEL-P38, CBEL-ERK) the absorbance for the phosphorylated and non-phosphorylated form of the target protein was measured in two identically treated wells. For the NFkB p65 kit, in addition to measuring the phosphorylated and non-phosphorylated target, GAPDH was measured in each well.

3.2.13 LUMINEX

Conditioned media from the initial LPS and PGN treatment was collected and analysed for 73 secreted proteins for monolayer culture (Table 3.2, 2D) and 28 proteins for alginate bead culture (Table 2, 3D) using bead-based Luminex multiplex immunoassays (Protavio, Athens, Greece), as described previously [232]. Six assay panels were employed to measure the 73 analytes in the conditioned media, utilising an eight-point standard curve. Ninety-six well plates were coated with 50 µl of each 1X bead mix dilution (Mag-Plex® magnetic microspheres, Luminex Corp, Austin, TX, USA), containing 2'500 beads per bead ID, and incubated with 35 µl of standards, samples, and blanks for 90 minutes at room temperature on an orbital shaker (1'000 rpm). Wells were washed twice with assay buffer (PR-ASSB-1x, Protavio, Greece), followed by the addition of 20 µl of a detection antibody mix at an average concentration of 1 µg/ml to each well, and incubated for 60 minutes at room temperature on an orbital shaker (1'000 rpm). After two more washes with assay buffer, 35 µl of Streptavidin-R-Phycoerythrin conjugate (5 µg/ml, SAPE-001, MOSS, USA) was added and incubated for 15 minutes under the same conditions. Finally, the wells were washed twice and resuspended in 130 µl of assay buffer, and the median fluorescence intensity (MFI) values were measured using the Luminex FLEXMAP 3D platform (Luminex Corp., Austin, TX, USA) with a minimum of 100 bead counts per sample.

For the Luminex analysis performed on the study of treatment with PGN, *S. aureus* or *C. acnes* with or without inhibitors a reduced panel was used based on results from the first study (Table 3.2, I). The analysis was performed in Sheffield, using R&D Systems' Luminex assay (LXSAHM-20, R&D systems Minneapolis, US) following the manufacturer's instructions. The median MFI values were measured utilising Luminex 200, Thermo Scientific with a minimum of 50 bead counts per sample.

Table 3.4 | List of analysed proteins

Analytes grouped according to their function. Whilst all the below listed cyto- and chemokines were measured for the monolayer culture stimulated with LPS and PGN (2D), the panel was reduced for the alginate culture (3D) and the experiment of bacterial stimulation in combination with inhibitors.

	Abbreviation	Analytes	2D	3D	I
Anti-inflammatory cytokines	TGFb	Transforming Growth Factor Beta1	x		
	IL1RA	Interleukin 1RA	x	x	x
	IL2RA	Interleukin 2RA	x		
	IL4	Interleukin 4	x	x	
	IL10	Interleukin 10	x	x	
	IL11	Interleukin 11	x		
	IL13	Interleukin 13	x		x
	IL22	Interleukin 22	x		
	LIF	LIF Interleukin 6 Family Cytokine	x		
Proinflammatory/catabolic cytokines	IL1A	Interleukin 1A	x	x	x
	IL1B	Interleukin 1B	x	x	x
	IL6	Interleukin 6	x	x	
	IL7	Interleukin 7	x	x	x
	IL15	Interleukin 15	x		
	IL16	Interleukin 16	x	x	
	IL17A	Interleukin 17A	x		x
	IL17F	Interleukin 17F	x	x	
	IL-18	Interleukin 18	x	x	x
	IL20	Interleukin 20	x	x	
	MIF	Macrophage Migration Inhibitory Facto	x		
	IFNA2	Interferon Alpha 2	x		
	IFNG	Interpheron Gamma	x	x	x
	RETN	Resistin	x	x	
	S100AB	S100 calcium-binding protein A8	x	x	
	ST2	Suppression Of Tumorigenecity 2	x	x	
	TNF	Tumor Necrosis Factor	x	x	x
	TNF10	Tumor Necrosis Factor Member 10	x	x	
	TNFRF9	TNF Receptor superfamily member 9	x	x	
	TWEAK	TNF Superfamily Member 12	x		
Neurotrophic/ angiogenic regulators	CNTF	Ciliary Neurotrophic Factor	x	x	
	NGF	Neural Growth Factor	x	x	x
	NRG1	Neuregulin 1	x	x	
	PAI1	Serpin Family E Member 1	x		
	PROK1	Prokineticin1	x	x	
	VCAM1	Vascular Cell Adhesion Moldecule 1	x		
	VEGF	Vascular Endothelial Growth Factor A	x		x
	2D, 3D	PGN, LPS treatment monolayer and alginate beads			
	I	Bacterial stimulation combined with inhibition			

	Abbreviation	Analytes	2D	3D	I
Chemokines	CCL2	C-C Motif Chemokine Ligand 2	x		
	CCL3	C-C Motif Chemokine Ligand 3	x		
	CCL4	C-C Motif Chemokine Ligand 4	x		x
	CCL7	C-C Motif Chemokine Ligand 7	x		
	RANTES	C-C Motif Chemokine Ligand 5	x		x
	Eotaxin	C-C Motif Chemokine Ligand 11	x		
	CCL17	C-C Motif Chemokine Ligand 17	x		
	CCL19	C-C Motif Chemokine Ligand 19	x		
	CCL20	C-C Motif Chemokine Ligand 20	x		
	CCL22	C-C Motif Chemokine Ligand 22	x		
	CTACK	C-C Motif Chemokine Ligand 27	x		
	GROA	C-X-C Motif Chemokine Ligand 1	x		
	IL8	Interleukin 8	x		
	CXCL9	C-X-C Motif Chemokine Ligand 9	x		
	IP10	C-X-C Motif Chemokine Ligand 10	x		x
	CXCL11	C-X-C Motif Chemokine Ligand 11	x		
	CXCL12	C-X-C Motif Chemokine Ligand 12	x		
	CXCL13	C-X-C Motif Chemokine Ligand 13	x		
	CXCL16	C-X-C Motif Chemokine Ligand 16	x		
	SCF	Stem Cell Factor	x	x	
Regulators immune cell differentiation/survival	IL5	Interleukin 5	x		
	IL9	Interleukin 9	x		
	IL12	Interleukin 12	x		
	sRANK-L	Receptor Activator of NF-kB	x		
Degrading enzymes/ inhibitors	MMP1	Matrix Metallopeptidase 1	x	x	
	MMP2	Matrix Metallopeptidase 2	x		
	MMP3	Matrix Metallopeptidase 3			x
	MMP7	Matrix Metallopeptidase 7	x		
	MMP9	Matrix Metallopeptidase 9	x	x	
	MMP13	Matrix Metallopeptidase 13	x	x	
	TIMP1	TIMP Metallopeptidase Inhibitor 2	x		
others	DEFB1	Defensin Beta 1	x		
	FGF Basic	Fibroblast Growth Factor 2	x	x	x
	M-CSF	Colony Stimulating Factor 1	x		
	GM-CSF	Colony Stimulation Factor 2	x		
	G-CSF	Colony Stimulation Factor 3	x	x	x
	ICAM1	Intetercellular Adhesion Molecule 1	x		x
	FST	Follistatin	x	x	

3.2.14 STATISTICAL ANALYSIS

Statistical analysis for IHC positivity rates was conducted using GraphPad Prism (Version 10.3.1 509). A Kruskal-Wallis test with Dunn's multiple comparisons was used to compare different groups for each antibody staining. A two-tailed Pearson correlation analysis with a 95 % confidence interval was performed to assess the correlation between positivity rates for various antibodies. For the comparison between bacterial cell wall component treatments and the control group, statistical analysis was conducted in R (R Core Team, 2020) and RStudio (R version 4.4.1, RStudio Team, 2020), utilising the "rstatix 29" and "stats 30" packages. Kruskal-Wallis tests with Bonferroni correction were applied to adjust p-values for multiple comparisons. Additionally, differences in cytokine expression levels between PGN- and bacteria-stimulated samples, with or without inhibition, were analysed using Kruskal-Wallis Dunn's multiple comparisons in GraphPad Prism. A p-value of ≤ 0.05 was considered statistically significant. Experiments were conducted in biological triplicates unless stated differently.

3.3 RESULTS

3.3.1 *C. ACNES* AND *S. AUREUS* ARE PRESENT IN NON-HERNIATED HUMAN IVD SAMPLES

C. acnes (detected with an antibody to *C. acnes* lysate*)* and *S. aureus* were investigated in human IVD samples using immunohistochemical staining (Figure 3.2, A). *C. acnes* was detected in all the samples ranging from 5.9-99.6 % of cells with immunopositivity staining (n = 79, average positivity rate= 68.15 ± 26.6 %) (Figure 3.2, B). No statistically significant difference was observed between age groups, degeneration grade or presence of Modic change (Figure 3.2). *S. aureus* was detected in 38 out of 78 IVDs ranging from 0.6 to 7.6 % (average positivity rate 1.9 ± 1.4%). Samples from female (f) patients showed a higher abundance of *S. aureus* than samples from male (m) patients (f = 60.5 % (26/43), m = 47.8% (11/23)). No differences were observed in the different age groups, degeneration states or types of Modic changes. *C. acnes* and *S. aureus* were solely detected intracellularly and not as biofilms within the tissue (Figure 3.2).

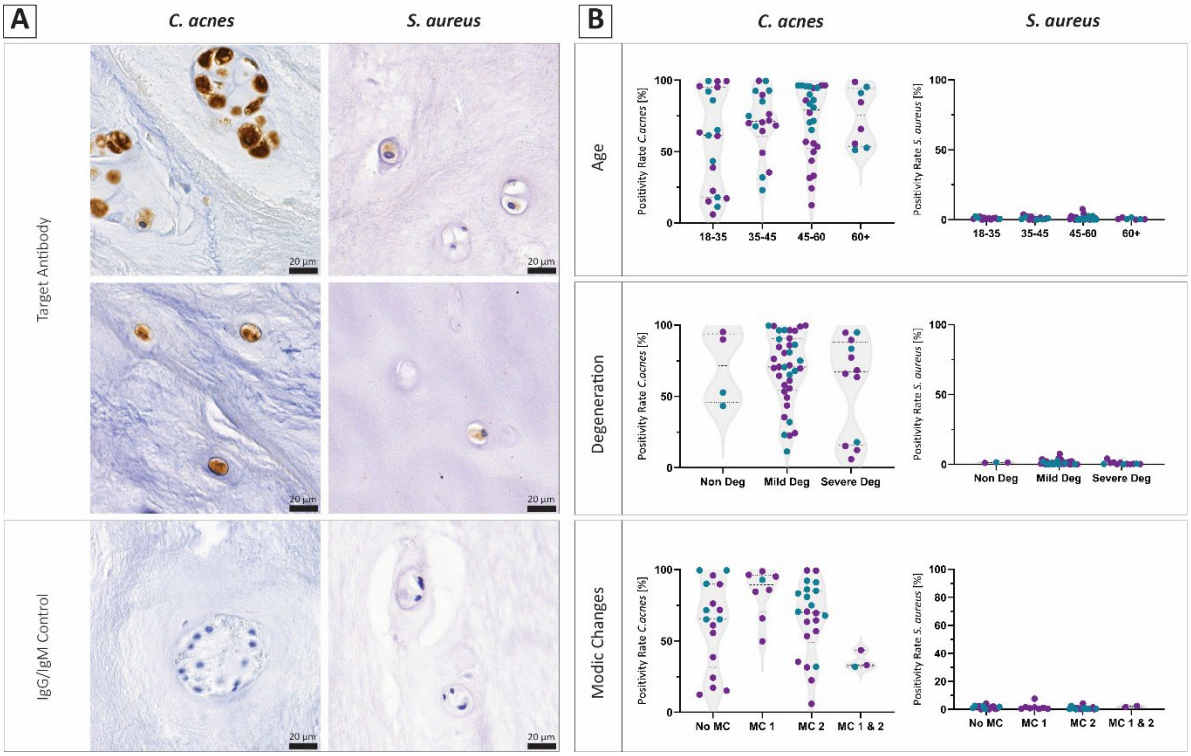

Figure 3.2 | *C. acnes* and *S. aureus* are present within non-herniated human IVDs

A Immunohistochemical staining for *C. acnes* lysate and *S. aureus* in human IVD tissue. Brown staining confirms the presence of the target antigen, whilst the only blue IgG/IgM control shows no unspecific binding. The bacteria were only detected intracellularly and not as biofilm within the tissue **B** Positivity rate of *C. acnes* and *S. aureus* in each sample, separated according to age (top), the histological state of degeneration (middle) and the type of Modic changes (bottom). The different colours purple and blue represent female and male tissue donors respectively. Statistical analysis was performed using Kruskal-Wallis multiple comparison.

3.3.2 TLR2, TLR 4 AND NOD2 ARE EXPRESSED IN HUMAN IVD SAMPLES; NOD2 PRESENCE CORRELATES WITH THE POSITIVITY RATE OF *C. ACNES*, TLR2 AND TLR4

Immunohistochemical staining confirmed the presence of TLR2 (average positivity rate= 67.4 ± 24.5), TLR4 (average positivity rate= 28.52 ± 23.6) as well as NOD 2 (average positivity rate= 28.27 ± 26.25) within human IVD tissue (Figure 3.3, A). Pearson correlation showed a positive correlation between the expression of TLR2 and NOD2 ($p=1.58x10^{-6}$, r=0.589), TLR4 and NOD2 ($p= 1.79x10^{-7}$, r=0.576) and

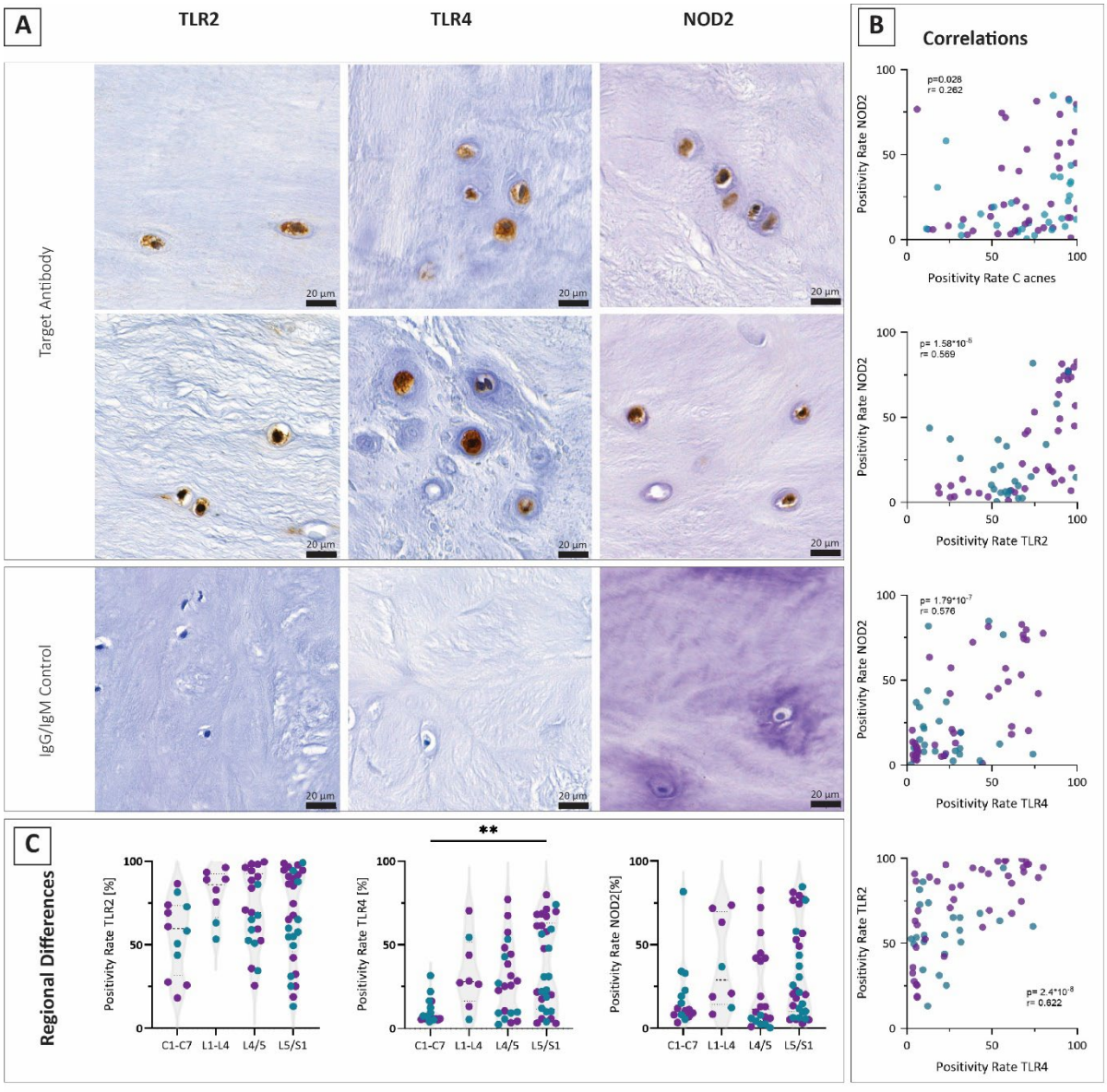

Figure 3.3 | Expression of TLR2, TLR4 and NOD2 within human IVD samples

A Immunohistochemical staining for TLR2, TLR4 and NOD2 confirmed their presence within the human IVD. The brown staining shows the presence of the target antigen whilst the blue IgG/IgM controls confirm only specific binding occurred. **B** Pearson correlation was performed between *C. acnes* lysate, *S. aureus*, LTR2, TLR4 and NOD2. A correlation was observed between *C. acnes* and NOD2, TLR2 and NOD2, TLR4 and NOD2 and between TLR2 and TLR4 (p=0.05). **C** Graphs showing regional differences for TLR2, TLR4 and NOD2. Purple dots represent samples obtained from female patients, blue dots from male patients. The samples were sorted according to their disc levels from C1-C7, L1-L4, L4/5 and L5/s1. TLR4 was significantly higher on the level L5/S1 compared to the cervical discs (C1-C7). Statistical analysis was performed using Kruskal-Wallis.

between TLR2 and TLR4 ($p=2.4x10^{-8}$, r=0.622) (Figure 3.3, B). A further correlation was detected between the positivity rate of NOD2 and the positivity rate of *C. acnes* (p=0.028, r=0.262) (Figure 3.3, B). While other comparisons failed to show significant correlations (p>0.05). Division of the samples into their spinal location showed that TLR4 showed significantly more immunopositively stained cells (p=0.0025) in discs at level L5/S1, compared to cervical IVDs (Figure 3.3, C), whilst TLR2 and NOD2 did not show differential percentage immunopositivity with disc level.

3.3.3 CORRELATION BETWEEN BACTERIAL COMPONENTS AND RECEPTORS WITH CATABOLIC FACTORS

Immunohistochemical staining revealed the expression of TLR2, TLR4 and NOD2 within the IVD. Additionally staining showed the presence of catabolic factors interleukin-1β (IL-1β), matrix

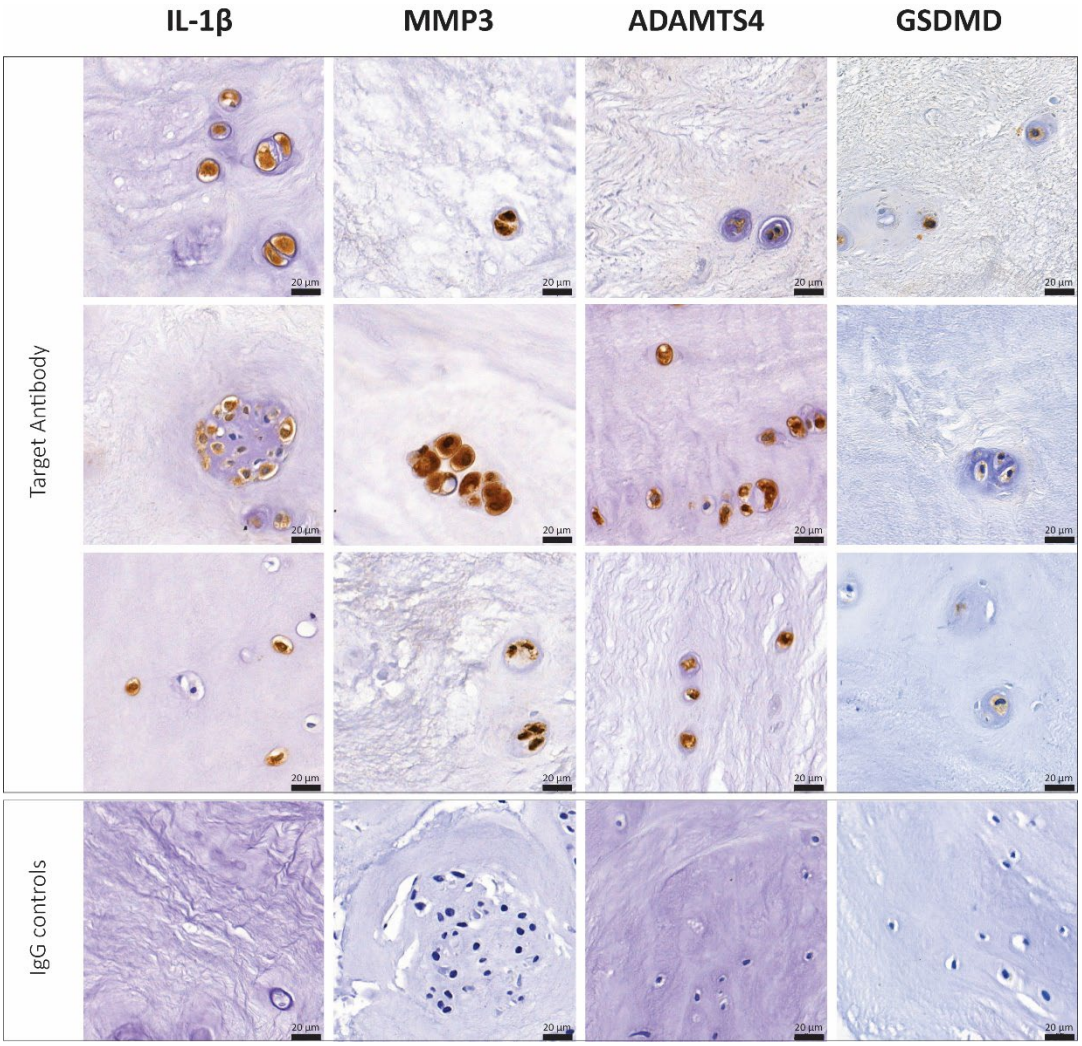

Figure 3.4 | Immunohistochemical staining for catabolic factors

Immunohistochemical staining for catabolic factors IL-1β, MMP3, ADAMTS4 and Gasdermin D confirmed their presence within the human specimens used in this study. The brown staining shows the presence of the target antigen whilst the blue IgG/IgM controls confirm only specific binding occurred.

metalloproteinase 3 (MMP-3), a disintegrin and metalloproteinase with thrombospondin motifs 4 (ADAMTS4) and gasdermin-D (GSDMD) (Figure 3.4).

Pearson correlation between the patients age, the degenerative state of the tissue, different catabolic factors and the bacteria as well as the receptors showed a positive correlation between the patients age and the positivity rate of *C. acnes* (p=0.048, r=0.235) (Figure 3.5). The histological grading score representing the tissue's degenerative state did not show any correlation with the catabolic factors, the presence of bacteria or the expression of TLR2, TLR4 and NOD2. The positivity rate of IL-1 showed a moderate positive correlation with matrix mettaloproteinase-3 (MMP-3) ($p=7.03x10^{-6}$, r=0.518) and TLR4 ($p=2.1x10^{-6}$, r=0.539) as well as a weak positive correlation with NOD2 ($p=2.6x10^{-5}$, r=0.483), TLR2 ($p=2.06x10^{-4}$, r=0.455) GSDMD (p=0.004, r=0.371) and ADAMTS4 (p=0.031 ,r=0.263) (Figure 3.5b). MMP-3 showed another moderate positive correlation with NOD2 ($p=6.56x10^{-9}$, r=0.649). It furthermore correlated with the positivity rate of GSDMD (p=0.001, r=0.426), *C. acnes* ($p=3.39x10^{-4}$, r=0.431) TLR2 (p=0.02, r=0.400) and TLR4 (p=0.04, r=0.424). The positivity rate of ADAMTS4 correlated with the positivity rate of TLR2 (p=0.002, r=0.406), TLR4 (p=0.011, r=0.319) and NOD2 ($p=9.6x10^{-5}$, r=0.465). Pyroptosis marker GSDMD correlated with the abundance of *C. acnes* (p=0.019, r=0.298) as well as NOD2 (p=0.022, r=0.288) (Figure 3.5).

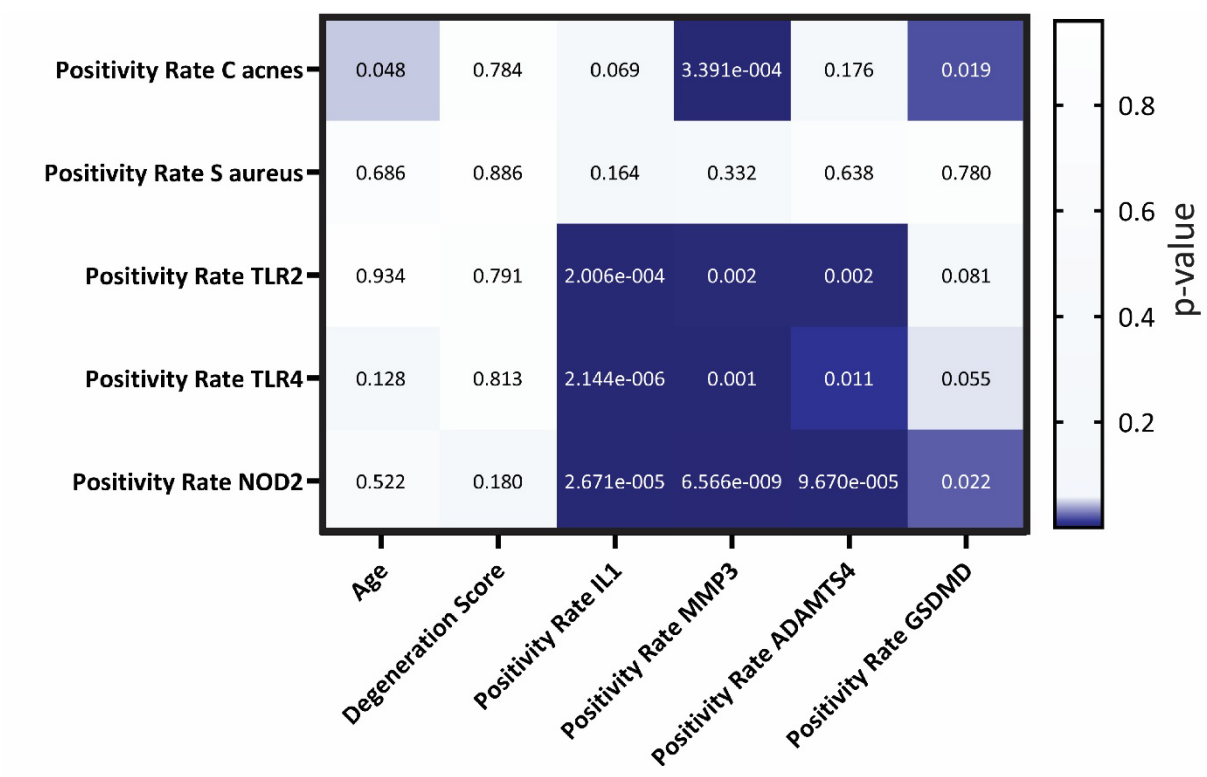

Figure 3.5 | Pearson correlation plotting the p-value

Pearson correlation between the factors age, degeneration score, catabolic factors and the abundance of the bacteria *C. acnes* and *S. aureus* as well as the different receptors TLR2, TLR4 and NOD2. Darker colours indicate a lower p-value. (p=0.05).

3.3.4 PGN STIMULATION INDUCES A CATABOLIC RESPONSE IN HUMAN NP CELLS

The levels of cytokines and chemokines in the collected media were measured using the Luminex 73-plex assay. These measurements, taken from the secretome of NP cells in monolayer cultures exposed to bacterial cell wall components, revealed a dose-dependent increase in catabolic cytokines, degrading enzymes and their inhibitors, neurotrophic and angiogenic regulators, anti-inflammatory cytokines, immune regulators, and chemokines following treatment with PGN (Figure 3.6, A). A dose response was observed for various factors (Figure 3.6, F). While treatment with LPS also resulted in an increase in multiple factors, the changes were not statistically significant compared to the untreated control group (Figure 3.6, A). Notably, treatment with 5 µg/ml of PGN led to a significant increase in IL-5, IL-9, IL-13, IL-18, IL-16, IL-6, and C-X-C chemokine ligand 12 (CXCL12, Figure 3.6, C, D). At a higher dose of 50 µg/ml PGN, there was a broad increase in numerous cytokines and chemokines. Factors that exhibited a significant upregulation ($p<0.05$) with at least a 1.5-fold change compared to the non-treated control were highlighted in volcano plots. These included anti-inflammatory cytokines (IL-1RA, IL-2Ra, IL-4, IL-10, IL-11, IL-13, IL-22, LIF), catabolic markers (IL-1α, IFN-α2, IFN-γ, IL-6, IL-7, IL-15, IL-16, IL-17F, IL-18, ST2, TNF, TNF-10, TWEAK), chemokines (CCL3, CCL4, CTACK, CXCL9, CXCL11, CXCL12, IP-10, RANTES, SCF), degrading enzymes (MMP-7, MMP-9), neurotrophic factors (CNTF, NGF, NRG1, PAI-1, PORK1), and cytokines (DEFB1, FGF-basic, FST, G-CSF, GM-CSF, ICAM1, IL-5, IL-9, IL-12, M-CSF) (Figure 3.6, B). In addition, stimulation with 50 µg/ml PGN of NP cells resuspended in alginate resulted in the upregulation of catabolic markers such as IL-1α, TNF, IL-6, IL-7, IL-16, IL-17F, IL-18, IFN-γ, and anti-inflammatory markers IL-1Ra, IL-4, and IL-10. Other factors like SCF, PROK1, FGF Basic, and G-CSF also showed significant increases (Figure 3.6, E). Factors showing a significant increases compared to the non-treated control but with less than a 1.5-fold change included CCL22, CXCL13, CXCL16, IFN-α2, IL-1β, IL-17A, IL-20, S100A8, sRANK-L, ST2, TNFRSF9, and VEGF.

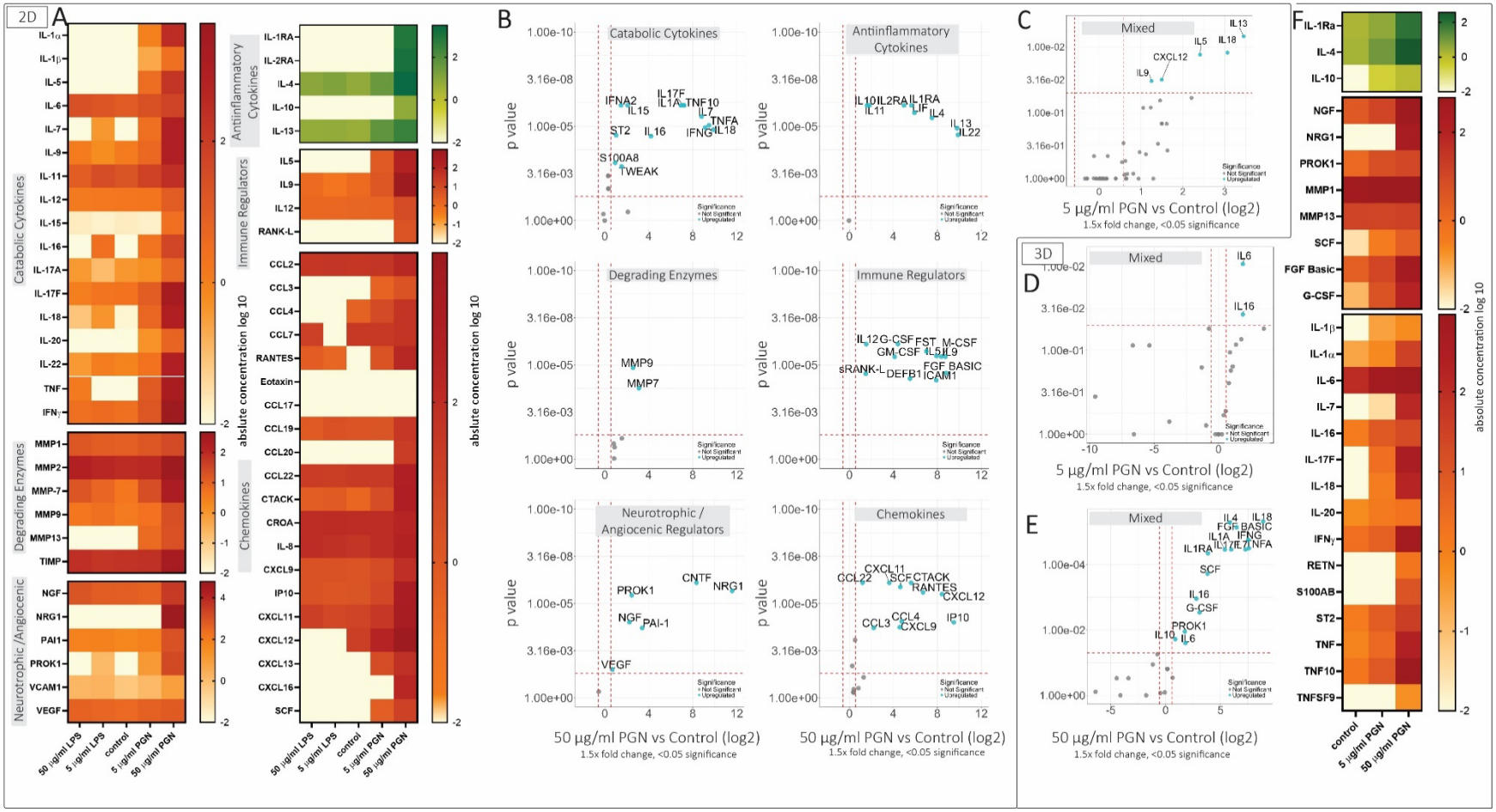

Figure 3.6 | Exposure of human NP cells to bacterial cell wall components

A Heatmaps of the absolute cytokine concentration obtained from media of human NP cells (n=3) in monolayer stimulated with LPS or PGN respectively for 48 hours. **B,C,D,E** Volcano plots for the different cyto- and chemokines, grouped according to their function. Cyto- and chemokines plotted show a 1.5x fold change and are significantly upregulated compared to the untreated control. Statistical analysis was performed using Kruskal Wallis with a p value adjustment through Bonferroni correction**. F** Showing heatmaps of the absolute concentration of cyto- and chemokines measured with Luminex from the media of NP cells resuspended in alginate (n=3) stimulated with PGN for 72 hours.

3.3.5 *S. AUREUS* IS DETECTED INTRACELLULARLY AFTER ONE HOUR OF CO-CULTURE

S. aureus and *C. acnes* were first grown under conditions mimicking the disc environment. The growth of *S. aureus* was not affected by the different culture conditions, *C. acnes* however showed a slower growth under LG media than Mueller Hinton Broth (Figure 3.7). Fluorescently labelled *S. aureus* was observed intracellularly within disc cells after a one-hour incubation period at an MOI of 1:100 (Figure 3.8).

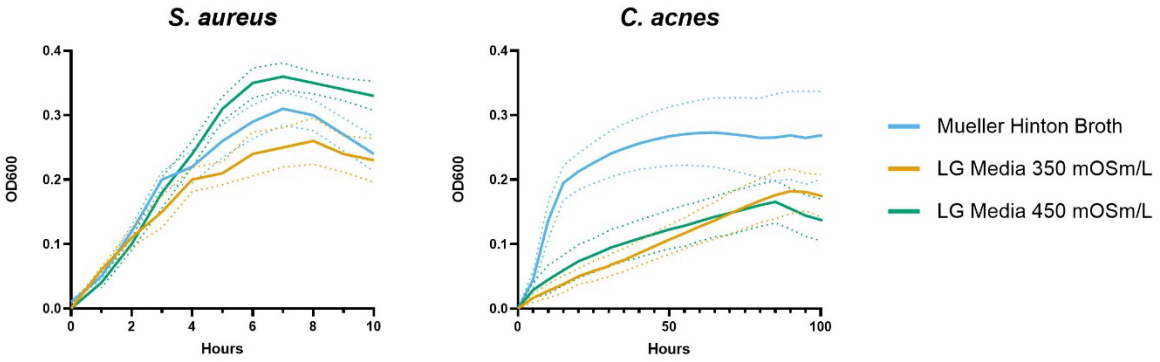

Figure 3.7 | Growth curve of bacteria in different growth-media

S. aureus and *C. acnes* grown in Mueller Hinton Broth, complete LG Media at an osmolarity of 450 mOSm/L, and complete LG Media at an osmolarity of 350 mOSm/L at 5 % O_2. S aureus growth was not impacted by the different culture conditions; however, growth of C. acnes was slowed down in the LG Media culture conditions compared to the Mueller Hinton Broth control.

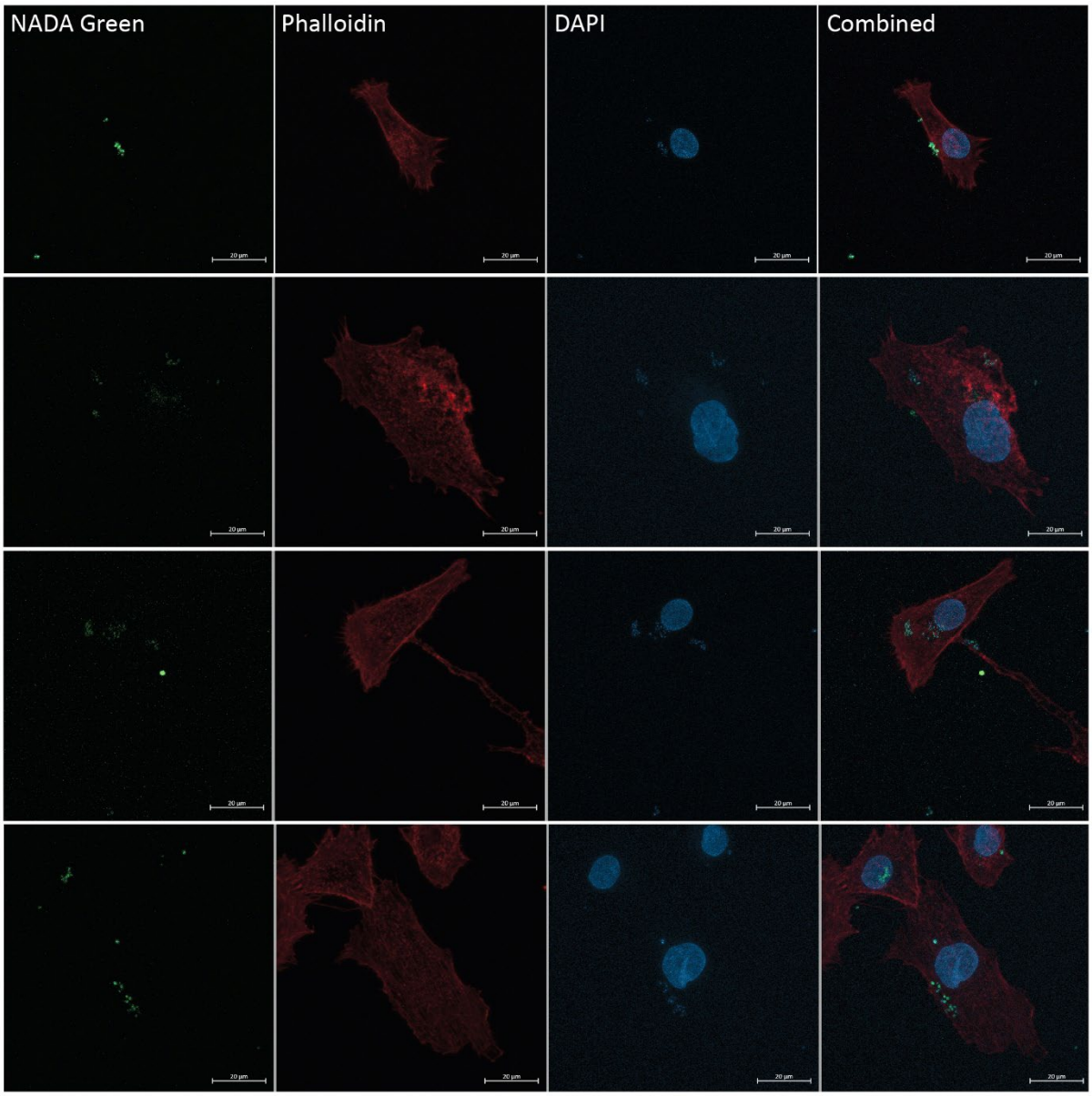

Figure 3.8 | Confocal image of intracellular *S. aureus*

Confocal microscopy image of *S. aureus* infected disc cells (multiplicity of infection (MOI) 1:100; 1 hour). Left displaying the NADA green stained *S. aureus*, followed by the phalloidin stained cytoskeleton of the cells and the DAPI stained nuclei of the cells.

3.3.6 LOW BACTERIAL LOAD DOESN'T UPREGULATE PHOSPHO-ERK, JNK, P38 OR NFKB

Within no treatment groups which were only treated with the inhibitors of TLR2 and NOD no changes in the expression of phosphorylated ERK, JNK, p38 or NFkB were observed (Figure 3.9). When cells were treated with either 50 µg/ml PGN, *S. aureus* (MOI 1:100) or *C. acnes* (MOI 1: 100) in the absence of inhibitors a small increase in phosphorylated ERK, phosphorylated JNK, phosphorylated p38 and phosphorylated NFkB following PGN treatment was seen which reached significance for ERK ($p=0.0041$) and NFkB ($p=0.0011$) compared to the non-treated control. Inhibition of TLR2 in combination with PGN treatment still showed a slight increase in ERK, JNK, p38 and NFkB, with the increase being significant for phosphorylated ERK ($p=0.0008$) and phosphorylated NFkB ($p=0.0006$) compared to inhibited but non-stimulated control. TLR2 inhibition in combination with *S. aureus* treatment led to a significant decrease ($p=0.0312$) in JNK compared to the non-treated control (Figure 3.9). Inhibition of NOD in combination with PGN treatment showed a small increase in phosphorylated-ERK, - JNK, -p38 and -NFkB which reached significance ($p=0.0003$) for phospho-NFkB compared to the non-treated, inhibited control. In the combined inhibition of TLR and NOD, PGN treatment led to an increase in phosphorylated ERK, -JNK, -p38 and NFkB with a significant increase in phosphorylated ERK ($p=0.0094$) and phosphorylated NFkB ($p=0.0109$) compared to inhibited non treated control (Figure 3.9). A significant increase ($p=0.0442$) in phospho-JNK was also observed following stimulation with *C. acnes* compared to the non-treated inhibited control (Figure 3.9).

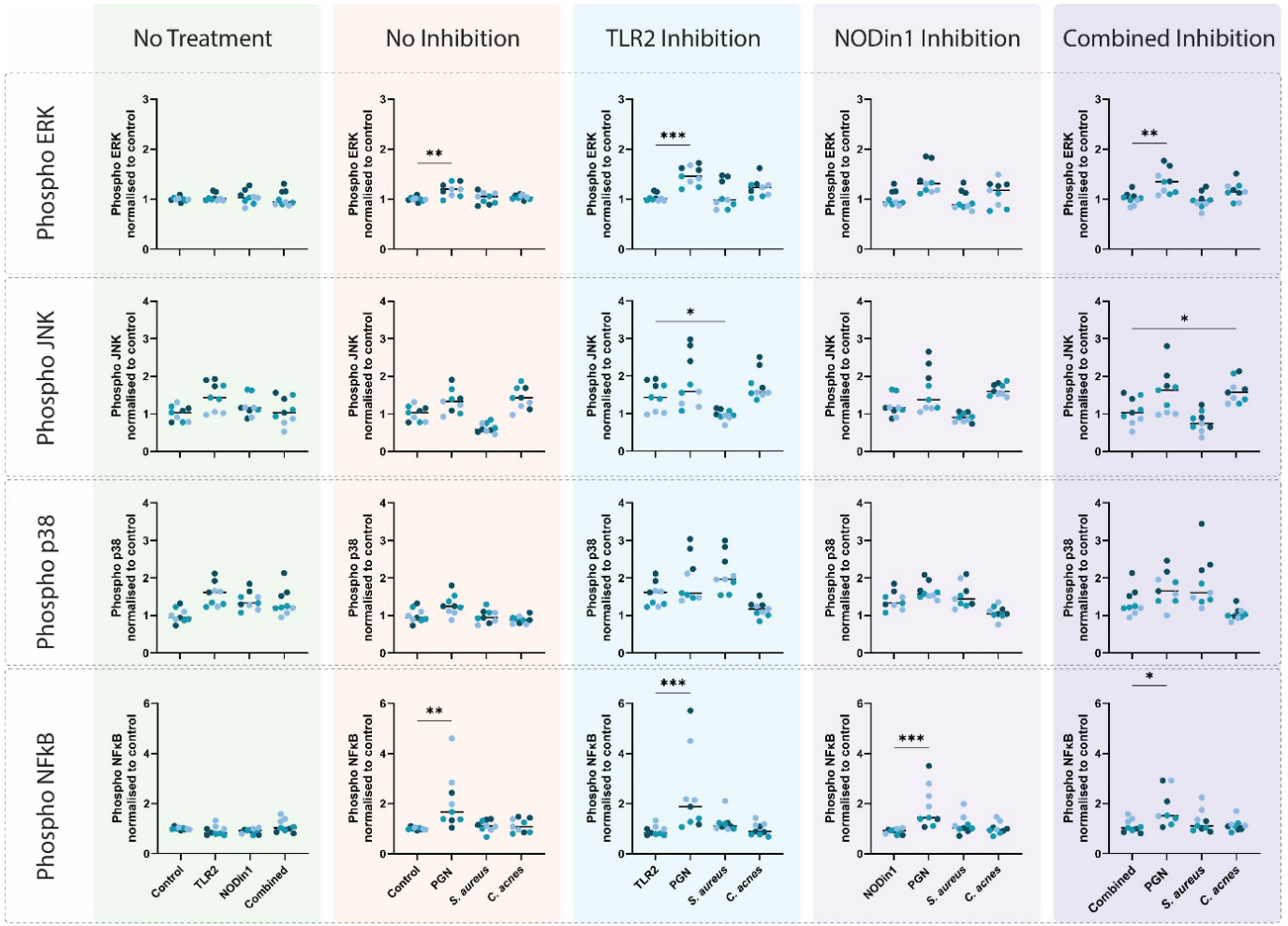

Figure 3.9 | Stimulation of NP cells with *S. aureus* and *C. acnes* combined with inhibitors.

In cell-ELISA was used to measure phospho- ERK, JNK, p38 and NFkB. Cells in monolayer under hypoxia were left to attach overnight before treatment with the inhibitors for TLR2, NODin1 and both combined for 24 hours. Followed by the inhibition was treatment with 50 µg/ml PGN, *S. aureus* (MOI1:100) and *C. acnes* (MOI1:100) for 2 hours in combination with the inhibitors. The different shades of blue represent the different donors (n=3). All the measured concentrations were normalised to the non-treated control. The No treatment graphs, show the different levels of phospho ERK, JNK, p38 and NFkB for cells only inhibited but not treated with a stimulant. No Inhibition shows treatment with PGN, *S. aureus* and *C. acnes* without inhibitors and TLR2, NODin1 and Combined Inhibition show the treatment combined with the inhibition. Statistical analysis was performed using Kruskal Wallis multiple comparison against the control group of each treatment (p= 0.05)

3.3.7 CATABOLIC FACTORS WERE INCREASED BY PGN STIMULATION BUT DOWN REGULATED BY CO-CULTURE WITH BACTERIA

Inhibition of TLR2 or NODin1 as well as the combined inhibition without treatment only showed an effect on CCL5 expression, as NOD inhibition led to a significant downregulation (p=0.0071) compared to non-inhibited control (Figure 3.10). Treatment without inhibition resulted in an increase in the PGN treated samples in two donors in TNF, IL-1α, IL-1Ra, and CCL5 (Figure 3.10). IL-1β was below the detection limit for the untreated control samples but was detected in the PGN stimulation control in 2 out of 3 donors, demonstrating treatment induced production of IL-1β. Treatment of cells in monolayer with *S. aureus* (MOI 1:100) in the absence of inhibitors resulted in a significant decrease of IL-1Ra (p=0.0307), CCL5 (p=0.0160) and VEGF (p=0.0011), compared to the control (Figure 3.10, Figure 3.11). Exposure of the cells to *C. acnes* (MOI 1:100) in the absence of inhibitors showed a significant decrease in VEGF (p=0.0068) and CXCL10 (p=0.0144) compared to the non-inhibited untreated control. Inhibition of TLR2 in combination with PGN treatment still showed an increase in TNF, IL-1α, IL-1Ra and CCL5 in 2 out of the 3 donors (Figure 3.10). Treatment with *S. aureus* in combination with TLR2 inhibition showed a significant decrease in IL-1α (p=0.0282), CCL5 (p=0.0352) and VEGF (p=0.0059) compared to the non-treated TLR2 inhibited control (Figure 3.10). *C. acnes* treatment combined with TLR2 inhibition showed a significant decrease in IL-1α (p=0.0301), CCL5 (p=0-0428), VEGF (p=0.0007) and ICAM (p=0.0435) compared to the control (Figure 3.10, Figure 3.11). Inhibition of NOD1 and NOD2 in combination with PGN treatment resulted in an increase in CCL5 in 2 donors and a significant increase in TNF (p=0.0246) and IL-1Ra (p=0.0301) compared to the NODin1-inhibited untreated control. A significant decrease of VEGF was detected in NOD inhibited samples treated with *S. aureus* (p=0.0123) and *C. acnes* (p=0.0421) compared to the control (Figure 3.10). Furthermore, the inhibition of NOD in combination with *C. acnes* exposure led to a significant decrease in CXCL10 (p=0.0361) (Figure 3.11). Combination of TLR2, NOD1 and NOD2 inhibition in combination with PGN treatment resulted in an increase in IL-1Ra, CCL5 and VEGF, and a significant increase in TNF (p=0.0027) compared to the inhibited untreated control (Figure 3.10). The combined inhibition together with *S. aureus* treatment resulted in significant decreases in CCL5 (p=0.0209), VEGF (p=0.0427), IL-7 (p=0.0074) and CXCL10 (p=0.0279) compared to the control. *C. acnes* treatment combined with inhibition of TLR2, and NODs resulted in a significant decrease in IL-1α (p=0.0033), VEGF (p=0.0078), and CXCL10 (p=0.0315) compared to the control (Figure 3.10). No changes in any treatment conditions or inhibitors were detected in IL-4, IL-18 and CCL4 (Figure 3.11). Cytokine concentration of MMP-9 were below detection limits, whilst MMP-3 was above the limit of detection and thus could not be quantified.

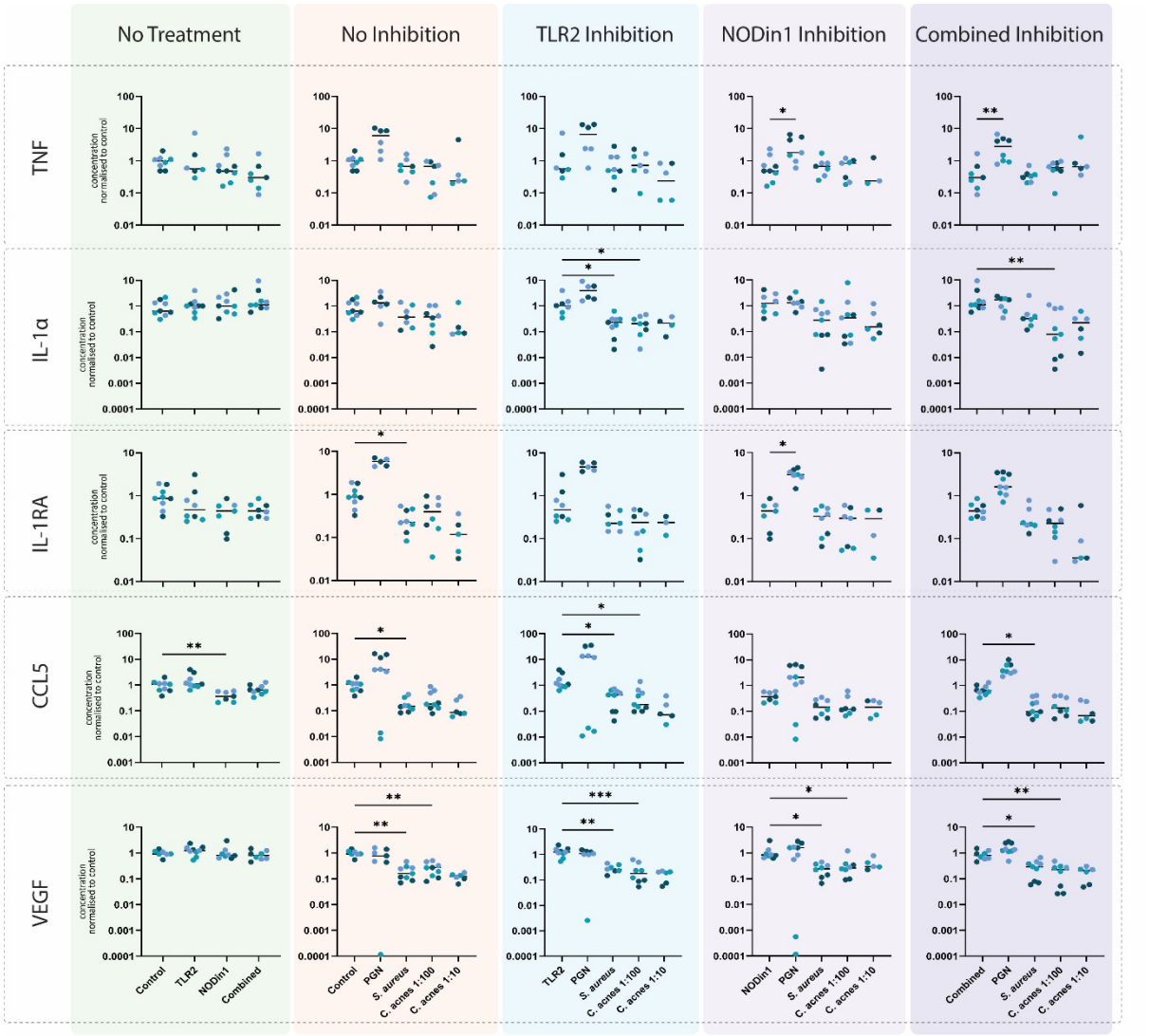

Figure 3.10| Cytokine expression following treatment with PGN, *S. aureus* and *C. acnes* in combination with inhibitors

Cells in monolayer were left to attach overnight in a low oxygen chamber before stimulating them with TLR2 inhibitor, NODin1 inhibitor and a combination of the inhibitors for 24 hours. Following the stimulation period cells were exposed to 50 µg/ml PGN, *S. aureus* (MOI 1:100) or *C. acnes* (MOI 1:100, MOI 1:10) for 2 hours followed by a PBS wash and the addition of fresh media supplemented with the inhibitors. The secretome was collected and a Luminex assay was performed. Concentrations of each cytokine are shown normalised to the non-stimulated non-treated control. Statistical analysis was not performed for *C. acnes* at an MOI 1:10 as the experiment was only performed in biological duplicates. Kruskal Wallis multiple comparison test was used to compare the treatments with the stimulation control (p= 0.05). Different shades represent different donors (n=3)

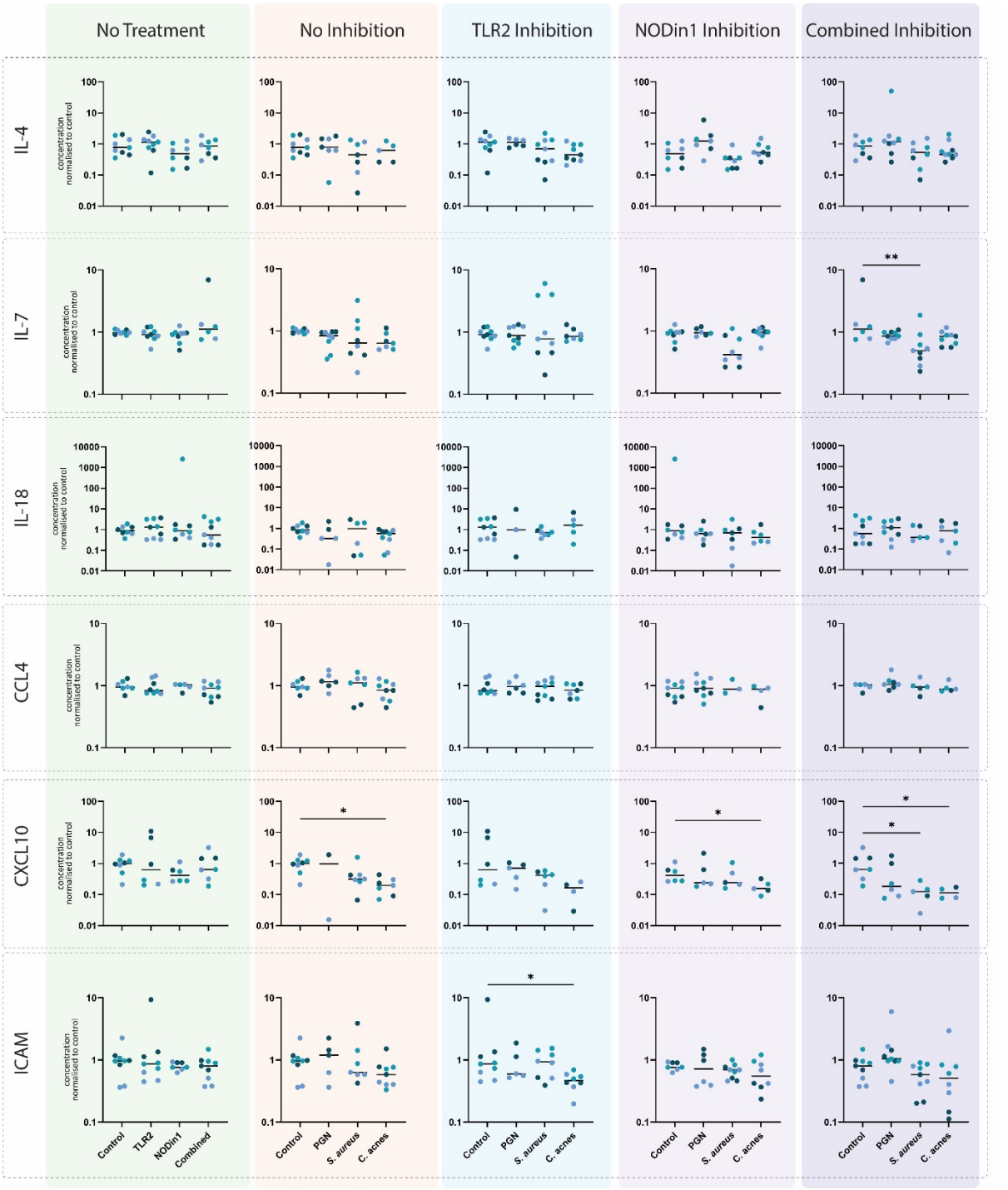

Figure 3.11 | Cytokine expression following treatment with PGN, *S. aureus* and *C. acnes* in presence of inhibitors

Cells in monolayer were left to attach overnight in a low oxygen chamber before stimulating them with TLR2 inhibitor, NODin1 inhibitor and a combination of the inhibitors for 24 hours. Following the stimulation period cells were exposed to 50 µg/ml PGN, *S. aureus* (MOI 1:100) or *C. acnes* (MOI 1:100, MOI 1:10) for 2 hours followed by a PBS wash and the addition of fresh media supplemented with the inhibitors. The secretome was collected and a Luminex assay was performed. Concentrations of each cytokine are shown normalised to the non-stimulated non-treated control. Statistical analysis was not performed for *C. acnes* at an MOI 1:10 as the experiment was only performed in biological duplicates. Kruskal-Wallis multiple comparison test was used to compare the treatments with the stimulation control (p= 0.05). Different shades represent different donors (n=3)

3.4 DISCUSSION

This study investigated the presence of bacteria within non-herniated human IVDs, aiming to distinguish between perioperative contamination and *in vivo* bacterial colonisation while also exploring the potential effect of bacteria on human disc cells and possible pathways upon bacterial exposure. By using immunohistochemical staining, *C. acnes* and *S. aureus* were not only detected within the tissue but could also be located intracellularly in human NP cells. After confirming bacterial presence, staining for catabolic factors, TLRs, and NOD2 revealed correlations between *C. acnes* and NOD2, as well as MMP-3 and GSDMD. Although the p-value for the correlation between *C. acnes* and IL-1β wasn't significant a low p-value (p=0.069) indicates a potential correlation, but a higher sample number may be required. Bacterial survival and growth were observed under harsh disc-like conditions for anaerobic *C. acnes* and facultative aerobe *S. aureus*. Bacterial cell wall components induced a catabolic response in human NP cells, both in monolayer and 3D constructs *in vitro*. However, a low bacterial load with laboratory strains of bacteria, mimicking predicted physiological levels within non-infected discs, did not affect catabolic cytokine expression. Additionally, inhibition of TLR2 and NOD did not fully suppress the catabolic response of NP cells to high doses of PGN exposure suggesting the involvement of alternative receptor mediated effects.

3.4.1 DETECTION OF BACTERIA IN NON-HERNIATED HUMAN DISCS

The topics of disc infection and the disc microbiome have sparked significant debate within the spine research community, challenging the longstanding paradigm that the IVD is sterile [128–130]. *C. acnes*, an aerotolerant anaerobic bacterium, has garnered particular interest in this discussion [131–133,233–236]. However, the two primary methods for bacterial detection, microbial culture and NGS, have faced criticism due to their inability to fully rule out perioperative contamination. To date, specific bacterial staining within the IVD has only been reported using fluorescence in situ hybridization (FISH), in a study focusing on biofilm presence in herniated human discs [236]. Herniation was an exclusion criterion in the current study to focus on degenerated but contained discs only, using discs reported at surgery to have an intact annulus, termed here as an intact disc, minimising the risk of contamination from surrounding tissue and determining whether bacteria are of disc origin. The detection of *C. acnes* and *S. aureus* intracellularly in NP and AF cells provides strong evidence that these bacteria represent true *in vivo* disc bacteria. Furthermore, bovine NP cells have been found to phagocytose latex beads and apoptotic bodies, suggesting NP cells may play an immune defensive role within the IVD, behaving in a macrophage-like manner [237,238]. The internalisation of *S. aureus* by human NP cells via phagolysosome formation was previously reported by Lin *et al*. [239]. Additionally, *C. acnes* has been observed within

living human NP cells in an *in vitro* experiment 48 hours post-infection [240]. The immunohistochemical detection of bacteria within the IVD further supports the existence of an intrinsic disc microbiome. Unlike microbial culture and NGS, immunohistochemistry enables the precise localisation of bacteria within disc cells, reducing the risk of contamination and offering more substantial evidence that the disc harbours its microbiome, with potential implications for disc health and pathology. By focusing exclusively on staining for *S. aureus* and *C. acnes*, despite recent evidence from 16S-Sequencing studies indicating that a variety of bacterial species can be present within IVDs, the bacterial scope may overlook the potential impact of other microbial species on disc pathology.

3.4.2 POSSIBLE PATHWAYS UPON BACTERIAL EXPOSURE

Bacterial components such as LPS and PGN are known to trigger a robust catabolic response in human NP cells, inducing the expression of the catabolic cytokine IL-1β, matrix-degrading enzymes MMP-13 and ADAMTS-4, and neurotrophic factors like NGF and BDNF through the activation of the TLR2 heterodimer and the TLR4 homodimer [226,241,242]. Consistent with previous studies, our *in vitro* experiments showed a significant catabolic response, especially with PGN treatment, highlighting the potential effects of bacterial presence in the disc environment.

Immunohistochemical staining revealed a positive correlation between *C. acnes* and MMP-3, as well as between *C. acnes* and GSDMD, a protein involved in pyroptosis [168]. However, no correlation was found between bacterial presence and the positivity rate of TLRs, suggesting the involvement of other mechanisms in driving this catabolic response beyond TLR activation alone. Indeed, TLRs may not be the dominant driver in the catabolic response to bacteria, as bacteria were detected intracellularly. Mengis *et al*. reported elevated TLR2 expression in cells from patients with Modic changes type 1 and in catabolic conditions, highlighting their pro-inflammatory and pro-catabolic roles, which may contribute to disc degeneration and MCs [224]. Similarly, Schmid *et al*. demonstrated in a study the involvement of the TLR2/4 pathways in inducing a catabolic response upon stimulation with *C. acnes*, but only in a subgroup of patients further supporting the involvement of other pathways [225].

NOD2 is an intracellular patten recognition receptor sensing muramyl dipeptide, a component of bacterial PGN. It plays a role in inflammatory responses, particularly in epithelial cells and immune cells, where it activates NFkB and MAPK pathways leading to cytokine production [243,244]. While NOD2 has not been previously reported in human NP cells, our immunohistochemical analysis detected NOD2 and showed its presence in the disc, with a positive correlation between NOD2 positivity and *C. acnes*. This finding points to a potentially important role for NOD2 in the disc's response to bacterial presence, further supporting the notion that multiple receptors contribute to bacterial detection and

the ensuing catabolic activity in the disc. It furthermore suggests that NP cells play an active role in immune surveillance within the disc environment and act as immune-like responders.

Despite these findings, the inhibition of TLR2 and NODs in the presence of PGN did not affect the phosphorylation of ERK, JNK, p38, or NFkB, nor did the inhibition alter the expression of cytokines such as TNF and IL-1α. This lack of inhibition suggests that either other signalling pathways may be compensating for the absence of TLR and NOD activation, or the inhibitors failed to inhibit the receptors fully. However, the concentration utilised for NODin1 inhibition was shown to be effective reducing IL-1β secretion in mice CD8 T cells upon infection [245]. TLR2 inhibition has also been shown to decrease the release of pro-inflammatory factors in BV2 microglial cells in a concentration which was applied in our study [246]. This points to the involvement of additional pathways, such as NLRP3 inflammasomes, which are activated by microbial stimuli and have been implicated in NP cell pyroptosis [168]. This aligns with our finding of a correlation between the positivity rate for GSDMD and *C. acnes* in immunohistochemistry samples. GSDMD is a key effector of pyroptosis, supporting the hypothesis that NLRP3-mediated inflammasome activation could contribute to the observed catabolic response.

Another potential pathway might involve C-type lectin receptors (CLRs), a family of pattern recognition receptors (PRRs) that detect specific carbohydrate structures commonly found on pathogens, including bacteria. CLRs recognise glycans such as mannose, fucose, and N-acetylglucosamine, which are components of bacterial peptidoglycan [170]. Notable CLRs include DC-SIGN, Dectin-1, and the mannose receptor, primarily expressed on antigen-presenting cells like macrophages and dendritic cells. Upon activation, CLRs initiate signalling cascades that lead to cytokine production and immune cell recruitment to fight infections [247–250]. However, it remains unknown whether CLRs are expressed within the IVD, representing an avenue for further investigation.

3.4.3 LOW BACTERIAL LOAD DOES NOT TRIGGER A CATABOLIC RESPONSE IN NP CELLS

Growth of facultative anaerobe *S. aureus* was not significantly affected by the harsh disc environment, suggesting its resilience under these conditions. In contrast, aerotolerant anaerobe *C. acnes* exhibited slower growth when exposed to 5% O_2 and disc culture media, compared to its growth in standard anaerobic conditions with Mueller-Hinton broth. This difference in growth rate highlights the unique adaptations of *C. acnes* to varying oxygen levels and/or nutrient requirements, which could impact its ability to persist in the disc.

Co-culture of NP cells with a low bacterial load (MOI 1:100, bacteria to NP cells) which was predicted to mimic physiological levels showed no significant activation of these pathways, aligning with the notion that a higher bacterial load may be required to induce a stronger response. Interestingly, we observed a strong downregulation of IL-1Ra, CCL5 and VEGF protein expression in cells stimulated with a low load of *S. aureus*. Furthermore, VEGF was strongly downregulated upon stimulation with a low load of *C. acnes*. The degenerated NP cells used for this experiment already have a higher catabolic cytokine expression than healthy cells [251] and, therefore, might also express VEGF at a higher level. Even when treated with PGN, one donor showed a decrease in CCL5 and IL-1Ra compared to the non-treated control, indicating donor variability. Notably, also the other two donors did not show an increase in VEGF, implying that the VEGF upregulation may occur later as a downstream effect of the rise in catabolic cytokines [65].

The observed cytokine expression levels might also be a consequence of the study design. First, we did not capture cytokine release during the initial 2-hour infection period, which may have resulted in missing early catabolic responses triggered by bacterial internalisation. Furthermore, the internalisation rate of bacteria by NP cells remains unknown, leading to uncertainty in determining the precise MOI specific to intracellular bacteria. Previous studies with higher MOI (100:1) reported robust activation of ERK, JNK, p38, and NFkB in human NP cells derived from patients with degenerate discs after *C. acnes* infection for different culturing periods peaking at 4 hours [252]. Elevated IL-6 and IL-8 levels in NP cells of IVDs from degenerate patient samples have also been associated with higher bacterial loads (MOI 100:1) after 24 hours *in-vitro* stimulation [226], suggesting that bacterial load and duration of exposure may play critical roles in modulating NP cell responses. It is important to note that bacteria multiply more rapidly than human cells, meaning the MOI will shift over time as bacterial populations grow. Additionally, culture conditions play a significant role in experimental outcomes. While previous studies utilised HG F12 DMEM media supplemented with 10-15% FCS at 37°C, 5% CO_2 and 21% O_2, the current study was conducted in a low-oxygen (5%) glovebox with LG DMEM media supplemented with 1% ITS-X, which more closely replicates the disc environment. However, using *in vitro* monolayer cultures, while useful for controlled experimentation, did not fully capture the complexity of the 3D architecture and microenvironment in the human IVD disc. This simplification could limit the applicability of the findings to *in vivo* conditions.

3.4.4 DIFFERENCES IN BACTERIAL PHYLOTYPES

Another important factor to consider is the bacterial strains used in experimental designs or detected in studies. Over the past decade, biochemical, transcriptomic, and proteomic analyses have shown that different phylotypes of *C. acnes* vary in their inflammatory potential and expression of putative virulence factors [135]. For instance, *C. acnes* is the most prevalent bacterium in the human skin microbiome, with no significant difference in load between healthy skin and acne-affected skin. However, inflammatory acne is believed to be triggered by an imbalance in the skin microbiota, specifically due to the selection of certain *C. acnes* phylotypes [253]. Additionally, different *C. acnes* types have been identified at different body sites. While phylotype IA was mostly identified in severe acne, infections in foreign material and soft tissues have been linked to phylotypes IB and II, types IB and IC have been associated with colonisation of the prostate, urinary tract, and orthopaedic equipment [253–256]. A study examining the phylotypes of *C. acnes* detected in IVDs reported that 18 out of 60 analysed samples were positive for *C. acnes* microbial cultures. Among these 18 strains, 39% belonged to phylotype II, 33% to type IA1, 6% to type IB1, and 22% to phylotype III. The study further observed that rabbits injected with *C. acnes* type IB or II strains exhibited significantly decreased T1-weighted imaging (T1WI) and increased T2-weighted imaging (T2WI) signals at eight weeks, whereas those injected with strain III showed hypointense signals on both T1WI and T2WI, highlighting differences between the phylotypes [257]. Schmid *et al*. used a clinical *C. acnes* isolate from spinal infection and ATCC purchased strain isolated from facial acne to treat human NP cells *in vitro*. They reported higher gene expression levels of IL-1β, IL-6 and IL-8 for the ATCC strains as well as higher protein levels in the secretome for IL-6 and IL-8 (IL-1β was not reported). Cytokine expression however was not significantly upregulated upon treatment with either *C. acnes* strain due to high fluctuations between their 4 donors [225]. Indicating again donor variability and the possibility of responders and non-responders.

Similarly, to *C. acnes*, *S. aureus* is a normal component of the skin microbiome, can cause a wide range of diseases depending on the virulence factors it carries, from mild skin infections to life-threatening conditions such as pneumonia and sepsis [258]. In this study, laboratory strains of bacteria were used: *C. acnes* isolated from acne-affected skin and *S. aureus* from the conjunctiva. It is important to note that the virulence factors of these laboratory strains may differ from strains isolated directly from infection sites.

3.4.5 CONCLUSION

This study provides compelling evidence of bacterial presence within non-herniated human intervertebral discs, specifically *C. acnes* and *S. aureus*. Immunohistochemical detection not only localises bacteria within NP cells but also reveals significant correlations between *C. acnes* and catabolic markers such as MMP-3, GSDMD, and NOD2. This suggests that NP cells may actively participate in immune surveillance. The involvement of NOD2 points to previously unrecognised intracellular pathways contributing to bacterial detection and subsequent inflammatory responses. Our findings suggest that TLRs may not be the dominant receptors in this process, indicating the role of other mechanisms, such as the NLRP3 inflammasome or potentially CLRs, which could drive the catabolic response, although this requires further investigation. While low bacterial loads did not trigger significant activation of the MAPK or NF-kB pathways, previous studies with higher bacterial loads highlight the importance of infection intensity and duration in modulating NP cell responses. These results underscore the complex interplay of multiple receptors and pathways in the disc's immune response to bacteria and pave the way for further exploration of targeted therapeutic interventions for disc-related pathologies.

ACKNOWLEDGMENTS

We thank the Marie Skłodowska Curie International Training Network (ITN) “Disc4All” for financial support. Our sincere thanks go to the surgeons (Mr Ashley Cole, Mr Neil Chiverton, Mr Lee Breakwell, Mr Michael Athanassacopoulos, Mr Marcel Ivanov, Mr James Tomlinson, Miss Shreya Srinivas, Mr Surya Gandham and Mr Paul Brewer) at Northern General Hospital and Claremont Hospital for their invaluable efforts in collecting tissue samples, as well as to the patients for their donations. We also extend our gratitude to Shreya Srinivas and Jo McKay for their assistance in the classification of samples according to Modic changes.

CHAPTER 4

EXPLORING THE PRESENCE AND IMPACT OF A DISC MICROBIOME: IMMUNOHISTOCHEMICAL DETECTION AND BACTERIAL CORRELATION WITH CATABOLIC FACTORS IN INTACT BOVINE INTERVERTEBRAL DISCs

EXPLORING THE PRESENCE AND IMPACT OF A DISC MICROBIOME: IMMUNOHISTOCHEMICAL DETECTION AND BACTERIAL CORRELATION WITH CATABOLIC FACTORS IN INTACT BOVINE INTERVERTEBRAL DISCS

Andrea Nüesch[1], Katherine Crump[2,3], Benjamin Gantenbein[2,3], Melissa Lacey[4], Christine Le Maitre[1]

[1] Division of Clinical Medicine, School of Medicine and Population Health, University of Sheffield, Sheffield, UK, [2] Tissue Engineering for Orthopaedics & Mechanobiology, Bone & Joint Program, Department for BioMedical Research (DBMR) of the Faculty of Medicine of the University of Bern, University of Bern, Murtenstrasse 35, CH-3008 Bern, Switzerland, [3] Department of Orthopaedic Surgery and Traumatology, Inselspital, Bern University Hospital, Medical Faculty, University of Bern, Freiburgstrasse 3, CH-3010 Bern, Switzerland, [4] School of Biosciences and Chemistry, Sheffield Hallam University, Sheffield, UK

This manuscript needs further data such as IHC staining in mice, rats, pigs, sheep and dog for *C. acnes* and *S. aureus* for publication.

AUTHOR CONTRIBUTIONS

AN, ML, BG and CLLM performed the conceptualisation. AN ran the main experiments, wrote the main text, performed the data analysis and prepared the visualisation and graphs. KC helped dissect the bovine tails as well as with the handling of the bioreactor. CLLM, ML, BG and KC provided intellectual input, reviewed and edited the manuscript and sourced funding. All authors read and approved the manuscript.

DETAILED AUTHOR CONTRIBUTION

I wrote the manuscript, conducted the experiments, and performed the data analysis and visualisation. Katherine Crump introduced me to the bovine organ culture, helped with the isolation of bovine IVDs and with the handling of the bioreactor.

Christine Le Maitre contributed to data interpretation, reviewed the manuscript, providing valuable feedback on the text, graphs, and visualisation. Mel Lacey and Benjamin Gantenbein provided additional review.

CONFLICT OF INTEREST

No conflict of interest.

ABSTRACT

This study aimed to explore the presence of bacteria in intervertebral discs (IVDs) from healthy bovine donors to determine whether these discs naturally harbour bacteria. Immunohistochemical staining was performed to detect *Cutibacterium acnes* and *Staphylococcus aureus* in non-cultured, directly isolated bovine IVDs. A subset of bovine explants was subjected to spiking with *Staphylococci* before their loading and culturing, to assess whether bacteria can invade intact discs. Additionally, the study examined the correlation between bacterial presence and matrix-degrading enzymes or catabolic factors, along with 16S rRNA sequencing of microbes in the collected media to identify potential bacterial sources. The results demonstrated the presence of *C. acnes* and *S. aureus* in intact bovine IVDs, with a higher positivity rate for *C. acnes* observed in the inner annulus fibrosus compared to the outer annulus. Both positive and negative correlations were found between bacterial presence and catabolic factors, suggesting complex interactions between bacteria and disc cell biology. These findings support the notion of a microbiome existing within IVDs and emphasise the necessity for further research into the roles of various bacterial phylotypes and their impact on disc health and degeneration. Moreover, the identification of environmental and gut-related bacteria highlights the significance of considering external sources of bacterial presence in studies of the IVD microbiome.

4.1 INTRODUCTION

The question of whether the intervertebral disc (IVD) harbours its own microbiome has become a prominent topic in disc research. Bacterial colonisation and dysbiosis have been proposed as potential causes for Modic changes, which are vertebral bone marrow lesions visible on MRI scans, as well as for disc degeneration [138,147]. To date, most studies have focused on detecting bacteria in herniated discs or IVDs with endplate defects [233]. Rajasekaran *et al.* investigated the presence of bacteria in MRI-normal IVDs from organ donors using next-generation sequencing and found differences in the microbiome composition compared to degenerate and herniate discs [147].

It has been suggested that bacteria found in human discs may reach structurally compromised IVDs via haematogenous spread from distant infections or enter the bloodstream through minor injuries, migrating from the skin or other epithelial surfaces [259,260]. The detection of bacteria within MRI-normal [147] and non-herniated IVDs (Chapter 3) raises the possibility that bacteria can penetrate intact discs.

Animal models investigating bacteria within IVDs often involve the injection of *C. acnes*, an anaerobic bacterium found in human IVDs, directly into the disc [143,261]. Inoculating *C. acnes* into caudal IVDs has been shown to induce disc degeneration in rats [143,144] and rabbits [145,146]. However, these studies focused on the effects of *C. acnes* on the disc without addressing whether it was already present in intact discs or if it could naturally invade healthy IVDs. The presence of *in-vivo* disc bacteria within species other than human has not been investigated to date.

This study aimed to determine whether IVDs from healthy bovine donor's harbour bacteria such as *C. acnes* and *S. aureus*. Additionally, exploring whether bacteria could invade intact discs, and whether the application of mechanical load affected this migration. Furthermore, the expression of catabolic factors associated with disc degeneration were investigated to enable potential associations with bacteria to be unravelled.

4.2 METHODS

4.2.1 STUDY DESIGN

This study addressed three key questions (Figure 4.1). The first aimed to determine whether IVDs from healthy bovine tails naturally harbour microbes, such as *C. acnes* and *S. aureus*. To investigate this, control discs were immediately fixed in formalin for immunohistochemical analysis to detect bacterial presence. Furthermore, media of samples was collected, whether from discs showing visible bacterial growth and those without, and media utilised to perform 16S rRNA sequencing and identify the microbes and their potential heritage. The second question examined whether bacteria could invade an intact bovine IVD under *in vitro* conditions and whether loading has an influence in the invasion. Following a free-swelling period, the samples were subjected to either static or dynamic loading as well as control or infected, where the culture media was spiked with a mixture of S*taphylococci* species. The third question examined the correlation between bacterial presence and catabolic factors, as well as toll-like receptors (TLRs).

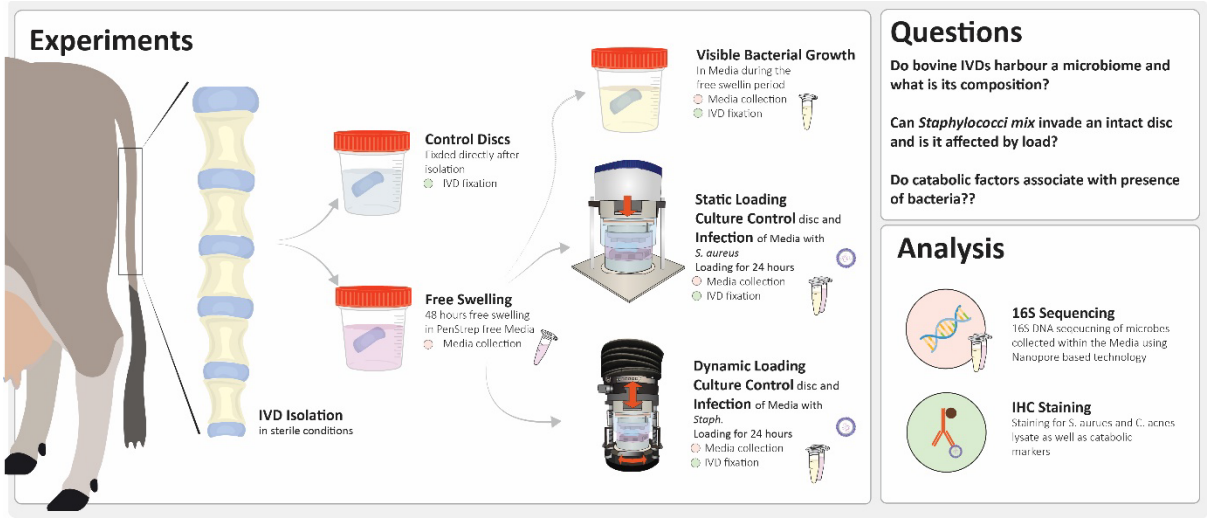

Figure 4.1 | Study overview

The aim of this study was to determine whether bacteria can invade an intact intervertebral disc and explore potential pathways of invasion. As a model for intact discs, whole organ samples were isolated from bovine tails. Control discs, used to assess the presence of bacteria in uncultured bovine intervertebral discs (IVDs), were immediately fixed and processed after isolation. The remaining discs were isolated and left to freely swell in media for 48 hours. Some discs showed signs of contamination, and both the discs and the surrounding media were collected to identify the bacteria present. Discs without contamination were either used as additional controls or exposed to media spiked with Staph species under static or dynamic loading conditions, to determine if S. aureus could subsequently be detected within the intact discs.

4.2.2 TISSUE PROCESSING

Bovine tails were obtained from a slaughterhouse in Interlaken, Bern, Switzerland. The tails were collected immediately after the animal's death and were transported in two freshly opened plastic bags during a one-hour train journey. The whole tail was washed in a 1% Betadine solution for 5 minutes before further steps were performed under sterile conditions in a laminar flow hood (Figure 4.2, A,B). The muscle was partially removed, and unnecessary parts, such as the tail end, were removed. For further sterilisation, the tail was quickly washed in 70% ethanol (Figure 4.2, C). Remaining muscle and tendons around the IVDs were removed, and the IVD-vertebrae connection point was located by gently moving the tail (Figure 4.2, D,E). The cleaving side was positioned 1-2 mm away from the IVD in the direction of the vertebrae. The growth plate located between the bony endplate of the IVD, and the vertebrae was removed as thoroughly as possible (Figure 4.2, G). After cleavage, the isolated IVD was wrapped with sterile gauze moistened with 0.9% sodium chloride containing 55mM sodium citrate.

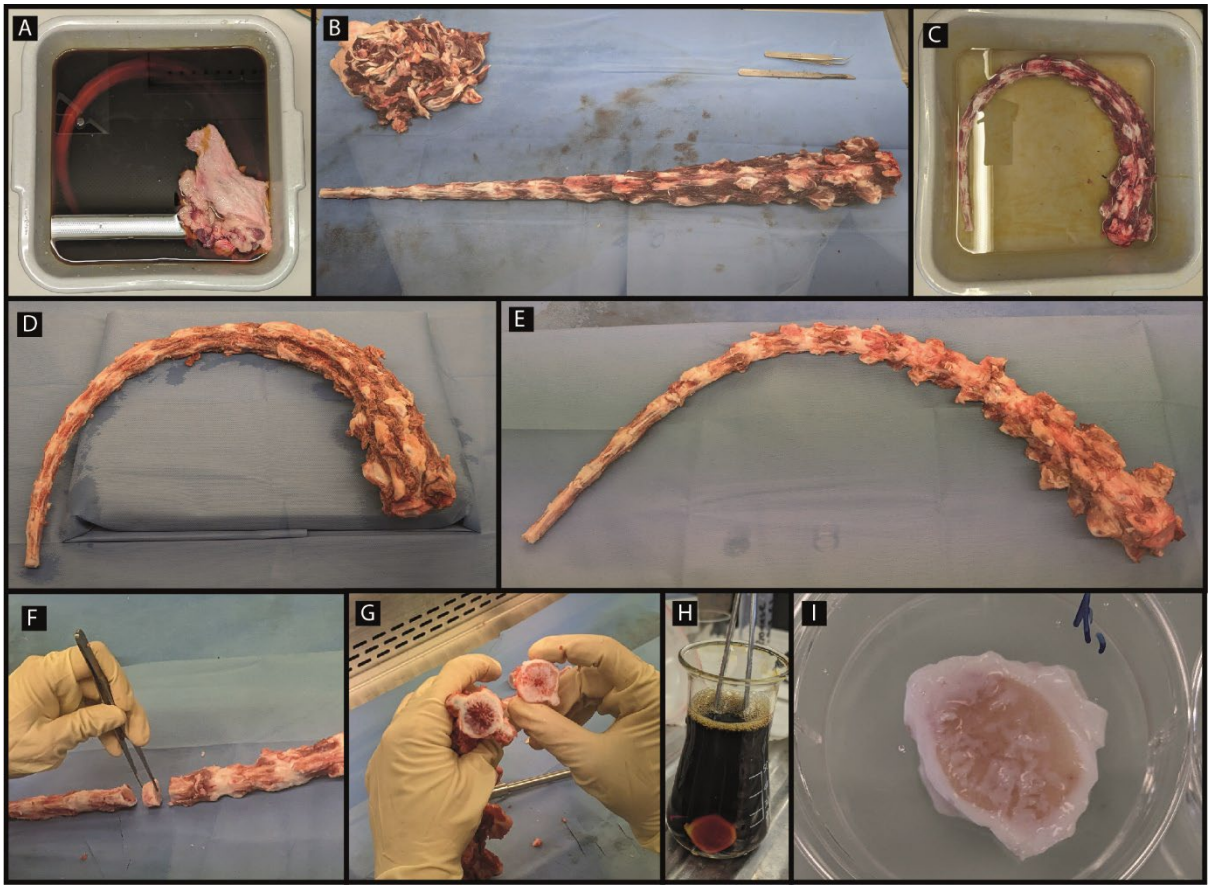

Figure 4.2 | Workflow of isolating whole bovine IVD

A Tail washing in 1% Betadine for 5 min **B** Removal of soft tissue **C** Additional washing step in 70% Industrial Spirit **D** Working under laminar flow hood with fresh sterile material **E** Removal of muscle and cleaning of disc tissue **F** Isolation of bovine whole organ model. Hammering of Guillotine through growth plate (GP) to separate the intervertebral disc (IVD) from the bone **G** GP shown, left side towards vertebrae, right side toward the IVD. Removal of as much cartilage from GP towards the bony endplate **H** Washing of IVD in 1% Betahdine and washing with Jetlevage to remove blood clots **I** Wash in 10% P/S and AmpB for 2x10 min before overnight free swelling in HG DMEM containing 5% FBS.

To remove coagulated blood from the bone, a pulsavac jet-lavage system was used. Before using the jet lavage system, the explant was dipped in Betadine (Figure 4.2, H). The gun was then applied at an angle of 30-60°, directed at the endplate surface for approximately 30 seconds on each side. To eliminate any microbes, the explant was washed twice in 10% Penicillin Streptomycin (P/S) for 10 minutes before being left to free swell overnight in high-glucose (4.5 g/L) Dulbercco's Modified Eagle Medium (HG-DMEM, #52100-039;Gibco, Life Technologies, Zug, Switzerland) supplemented with 1% P/S , 5% foetal bovine serum (FBS, #F7524, Sigma-Aldrich), 0.22% sodium hydrogen carbonate (#31437-500G-R, Sigma-Aldrich), 1mM sodium pyruvate (#11360-039, Thermo Fisher Scientific, Basel, Switzerland) and 10 mM HEPES buffer solution (#15630-056, Thermo Fisher Scientific). The following day, the media was changed every 1.5 hours using P/S fee media for a total of five times to remove any excess P/S. The explants were then left to free swell overnight in P/S free media [262,263].

4.2.3 BACTERIAL STRAINS

A mixture of Staphylococci strains was used in this study, which was first thought to be a pure *S. aureus* culture. However, 16-S sequencing reviled a mixture of *S. aureus*, *S. auricularis*, *S. caprae*, *S. condimenti*, *S. croceilyticus*, *S. felis*, *S. pasteuri*, *S. psicifermentans*, *S. schleiferi* and *S. werneri*. Bacterial cultures were grown overnight at 37°C in 21% O_2 on Mueller Hinton agar (70191, Merck, Dorset, UK) plates. Liquid cultures were prepared by adding one colony-forming unit (CFU) to 4 ml of complete media and incubated overnight.

4.2.4 TREATMENT GROUPS

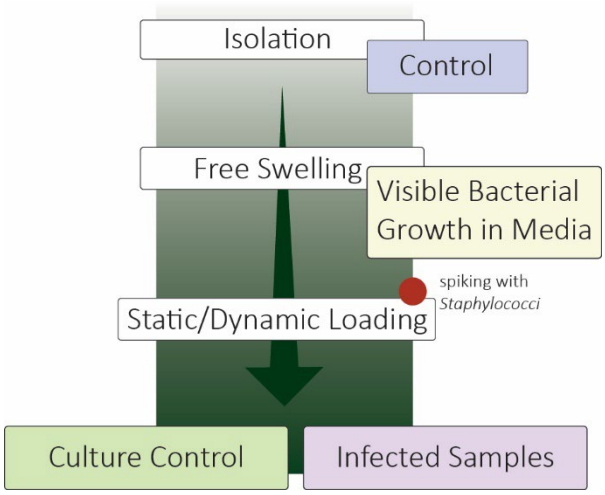

Figure 4.3 | Groups within the experiment

Overview of groups included in the experiment, from the directly isolated control samples to the contaminated samples collected during the free swelling period and the loaded samples divided into culture control and *Staph*. spiked infected samples.

Control samples were preserved in 10% (w/v) formalin (Leica, Milton Keynes, UK) immediately after isolation (Figure 4.2 F) and subsequently used for immunohistochemical staining (Appendix 4). Samples showing visible signs of bacterial growth during the free swelling period were also fixed in 10% formalin for one week to allow immunohistochemical analysis. Media from these samples was collected and stored at -80°C for later DNA extraction and 16S sequencing. Samples without visible bacterial growth were assigned either to the culture control group or the infection group, with further division based on static or dynamic loading conditions. Culture media was collected prior and after loading (Appendix 4). Media from the infection group samples was spiked with 100 µl of an overnight *Staphylococci* culture (OD_{600}=0.1, approximately 5.0 x 10^6 CFUs).

Static loading involved applying a 0.1 MPa load for 24 hours in an incubator at 37°C with 5% CO_2 and 20% O_2. Dynamic loading, performed in a custom-made two degrees-of-freedom bioreactor, consisted of a diurnal load that included a passive and active phase. The passive phase lasted 16 hours and consisted of a 0.1 MPa static load. The active phase lasted 8 hours and consisted of cyclic compression ranging from 0.3 MPa to 0.5 MPa at 0.1 Hz, combined with a 2° torsional load at 0.05 Hz, at 37°C with 5% CO_2 and O_2 for 24 hours [263,264].

4.2.5 IMMUNOHISTOCHEMICAL STAINING

The bovine IVD explants were preserved in 10% (w/v) formalin (Leica, Milton Kynes, UK) for one week and subsequently decalcified in 12.5% ethylenediaminetetraacetic acid disodium salt dihydrate (EDTA, Merck 03685, St. Louis US) for three months, with solution replacement occurring twice weekly. Decalcification was visually checked with µCT until clear. The samples were then processed and embedded in paraffin wax. Sections were cut to a 4 µm thickness using a microtome and mounted on positively charged Superfrost Plus slides (Epredia, Runcorn UK). Immunohistochemical staining followed previously established protocols [229]. After deparaffinisation and rehydration, endogenous peroxidases were blocked for 60 minutes in a 100% industrial methylated spirit (IMS) solution

containing 3% (v/v) hydrogen peroxide (Sigma Aldrich) and 0.06% (v/v) concentrated HCl. Antigen retrieval varied depending on the antibody used (Table 4.1) and included either no retrieval, enzymatic retrieval [0.1% (w/v) α-chymotrypsin (Sigma Aldrich, Poole, UK) in tris-buffer saline (20 mmol/L Tris, 150 mmol/L NaCl, pH 7.5) containing 0.1% (w/v) $CaCl_2$ for 30 minutes at 37°C], or heat retrieval [0.05M Tris, pH 9.5, preheated to 60°C before 5 minutes in a rice steamer]. After antigen retrieval, sections were rinsed in tris-buffered saline (TBS, (20 mmol/L Tris, 150 mmol/L NaCl pH7.5)) and blocked for 1 hour at room temperature with 1% (w/v) bovine serum albumin (BSA) solution containing 25% (v/v) normal serum in TBS to prevent nonspecific antibody binding. Primary antibodies were incubated overnight at 4°C in TBS with 1% (w/v) BSA. Simultaneous IgG control experiments were performed using the same protein concentrations to evaluate nonspecific isotype binding. After incubation, sections were rinsed in TBS three times, followed by the addition of secondary antibodies at room temperature for 30 minutes. After three more TBS washes, Elite® ABC reagent (Vector Laboratories, Peterborough, UK) was applied for 30 minutes. This was followed by an additional three TBS washes before the addition of 0.65 mg/mL 3,3'-diaminobenzidine tetrahydrochloride (DAB, Sigma-Aldrich) with 0.08% (v/v) hydrogen peroxide in TBS for 20 minutes, followed by 5 minutes of running tap water rinses. The nuclei were counterstained with Gill's Haematoxylin (GHS232, Sigma, Dorset, UK) for 20 seconds and blued under running water for 3 minutes. After dehydration in graded ethanol and clearing in xylene, the slides were mounted with Pertex®. Slides were scanned at 20x and 40x magnification using a PANNORAMIC® 250 Flash II DX slide scanner (3DHistech), and representative images captured to illustrate immunohistochemical staining. Image analysis was conducted following the protocol as described in chapter 2 distinguishing between the different regions CEP, NP, iAF and oAF calculating the positivity rate (Figure 4.4).

Table 4.1 | Target antibodies used for immunohistochemical staining

Primary Antibody	Clonality	Stock conc. [mg/ml]	Dilution	Antigen Retrieval	Secondary Antibody	Normal Serum
S. aureus (AB_1087481)	mouse monoclonal	2	1:100	enzyme	Rabbit anti mouse (ab6727)	Rabbit
C. acnes (D371-3)	mouse monoclonal	1	1:100	enzyme	Rabbit anti mouse (ab6727)	Rabbit
TLR2 (ab226913)	rabbit polyclonal	1	1:500	enzyme	Goat anti rabbit (ab6720)	Goat
TLR4 (ab22048)	mouse monoclonal	1	1:100	heat	Rabbit anti mouse (ab6727)	Rabbit
NOD1 (ab189409)	rabbit polyclonal	1	1:250	heat	Goat anti rabbit (ab6720)	Goat
NOD2 (ab31488)	mouse monoclonal	1	1:600	heat	Rabbit anti mouse (ab6727)	Rabbit
IL1b (KP1109B-100)	rabbit polyclonal	1	1:600	enzyme	Goat anti rabbit (ab6720)	Goat
IL6 (KP1898B-100)	rabbit polyclonal	1	1:600	enzyme	Goat anti rabbit (ab6720)	Goat
ADAMTS4 (ab185722)	rabbit polyclonal	3.2	1:200	none	Goat anti rabbit (ab6720)	Goat
MMP3 (ab53015)	rabbit polyclonal	1	1:400	enzyme	Goat anti rabbit (ab6720)	Goat
GSDMD (2100700)	rabbit monoclonal	0.78	1:100	heat	Goat anti rabbit (ab6720)	Goat
NLRP3 (ab263899)	rabbit monoclonal	0.58	1:100	none	Goat anti rabbit (ab6720)	Goat

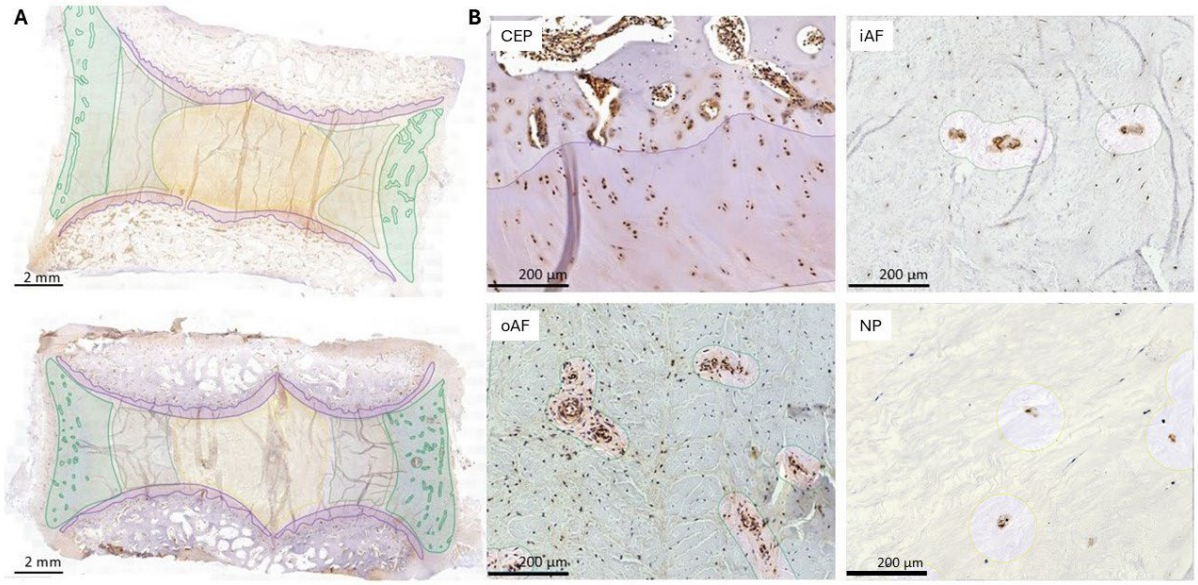

Figure 4.4| Analysis in QuPath

A Examples of manually selected regions are highlighted in different colours: the cartilaginous endplates (CEP) in purple, the nucleus pulposus (NP) in yellow, the inner annulus fibrosus (iAF) in light green, and the outer AF (oAF) in dark green. **B** A zoomed-in view of the regional selection demonstrates the CEP, NP with tissue folds excluded, oAF with blood vessels excluded, and iAF with staining artefacts excluded, scale bars as indicated.

4.2.6 DNA ISOLATION

DNA was isolated using the DNeasy® Blood and Tissue Kit (69504, Qiagen, Manchester, UK) following the manufacturer's protocol. Briefly, the collected media, control media, and an overnight bacterial culture were centrifuged at 5’000 g for 10 minutes to pellet the bacteria. The supernatant was discarded, and the pellet resuspended in 180 µl of enzymatic lysis buffer, followed by incubation at 37°C for 30 minutes. Afterward, 25 µl of Proteinase K and 200 µl of Buffer AL were added, and the sample was incubated at 56°C for 30 minutes. Subsequently, 200 µl of ethanol was added, and the mixture was vortexed briefly to ensure homogeneity. The lysate was transferred to a DNeasy mini spin column and centrifuged at 6’000 g for 1 minute. The flow-through was discarded, and the column was placed in a clean 2 ml collection tube. Then, 500 µl of Buffer AW1 was added, followed by centrifugation at 6’000 g for 1 minute. After discarding the flow-through, the spin column was transferred to a fresh collection tube, and 500 µl of Buffer AW2 was added. A final centrifugation at 20’000 g for 3 minutes ensured the drying of the DNeasy membrane. The spin column was placed in a 1.5 ml Eppendorf tube, and 200 µl of Buffer AE was applied to elute the DNA. After a 1-minute incubation at room temperature, the sample was centrifuged for 1 minute at 6’000 g. The eluted DNA was quantified using the Agilent High Sensitivity DNA Kit (Agilent Technologies, Santa Clara, Ca, USA)

following the manufacturer's instructions (Agilent High Sensitivity DNA Kit Quick Start Guide, Document No, G2938-90322) by SITRAN (University of Sheffield). The DNA samples were prepared by loading onto the Agilent 2100 Bioanalyzer for assessment enabling the precise measurement of low-concentration DNA samples providing high-resolution analysis.

4.2.7 16S RRNA SEQUENCING

Amplification of the 16S rRNA gene from extracted gDNA was performed using the 16S barcoding Kit 24 V14 (SQK-16S114.24, Oxford Nanopore Technologies, Oxford, UK). To ensure optimal sequencing results, a flow cell check was initially performed according to the MinKNOW protocol prior to library preparation. A 96-well plate containing 16S barcodes provided by the Kit were used, from which a set of barcodes (1-24) were separated and thawed at room temperature. After brief centrifugation, the barcodes were placed on ice. Genomic DNA samples were prepared by transferring 10 ng of DNA into 0.2 ml thin-walled PCR tubes and adjusting the volume to 15 µl with nuclease-free water. The samples were thoroughly mixed, spun down, and combined with LongAmp Hot Start Taq 2X Master Mix to a final reaction volume of 40 µl. Barcode addition involved carefully piercing the foil covering each barcode and transferring 10 µl of the desired barcodes into the sample tubes, followed by mixing and centrifugation. PCR amplification was performed using the following thermal cycling conditions: initial denaturation at 95°C for 1 minute, followed by 25 cycles of denaturation at 95°C for 20 seconds, annealing at 55°C for 30 seconds, and extension at 65°C for 2 minutes, with a final extension at 65°C for 5 minutes. Following amplification, 4 µl of EDTA was added to stop the reaction, and the barcoded samples were quantified using a Qubit fluorometer. Equimolar ratios of the barcoded samples were pooled, followed by a bead-based cleanup using AMPure XP Beads at a 0.6X volume ratio. The bead-bound DNA was washed with 80% ethanol, eluted in 15 µl of Elution Buffer, and quantified again using the Qubit fluorometer. Prior to loading the prepared library into the R10.4.1 flow cell (Flow-Min114, Oxford Nanopore Technologies) on the GridION instrument, the flow cell was primed according to manufactures instruction. Identification of the original single read was performed with epi2me-labs wf-metagenomics classifier Kraken 2 with a minimal read length of 1450 bp and a maximum of 1600.

4.2.8 STATISTICAL ANALYSIS

Statistical analysis for IHC positivity rates was performed using GraphPad Prism (Version 10.3.1 509). Group or regional comparisons for each antibody were evaluated using the Kruskal-Wallis test followed by Dunn's multiple comparison. A p-value of ≤ 0.05 was considered statistically significant.

For the 16S rRNA sequencing analysis, R (R Core Team, 2020) and RStudio (Version 4.4.1, RStudio Team, 2020) were used for both statistical analysis and data visualisation. Samples with a read count below 800 were excluded from further analysis, and species representing less than 3% of the total reads within a sample were also excluded. The analysis utilised several R packages: readxl for data import, dplyr and tidyr for data manipulation, and ggplot2 for visualisation. Custom colour palettes for species and genera were generated using the Polychrome package.

4.3 RESULTS

4.3.1 *C. ACNES* AND *S. AUREUS* ARE PRESENT IN BOVINE DISCS

Immunohistochemical staining for *C. acnes* (detected with an antibody against *C. acnes* lysate) and *S. aureus* revealed their presence within uncultured, directly fixed bovine IVDs (Figure 4.5, Appendix 5). While *C. acnes* was detected intracellularly in all control discs (n=8) and across all regions with high positivity rates (Positivity Rates; CEP=93.54 ± 4.9, NP=91.34 ± 7.61, iAF=98.33 ± 1.72, oAF=72.47 ± 20.47). *S. aureus* staining was positive in only 7 of the 8 samples, and its overall positivity rates were lower (CEP=27.73 ± 29.63, NP=2.98 ± 4.43, iAF=3.18 ± 4.58, oAF=11.97 ± 18.11) (Figure 4.9). However, for *S. aureus* more in tissue staining was observed then for *C. acnes* (Figure 4.5).

Regional comparison showed a significantly higher positivity rate of *C. acnes* in the iAF compared to the oAF in the control group (p=0.0003) (Figure 4.9). Although the positivity rate of *S. aureus* was highest in the CEP, no significant differences were found between regions (p>0.05) (Figure 4.9). Within samples where visible bacterial growth was identified, regional comparisons for *C. acnes* showed a significantly higher positivity rate in the iAF than in the oAF (p=0.0116). *S. aureus* displayed a significantly higher positivity rate in the culture control group in the CEP compared to the NP (p=0.0173) and iAF (p=0.0374), as well as in the oAF compared to the NP (p=0.0478). In the infection group, the positivity rate of the CEP was significantly higher than in the NP (p=0.0027) and iAF (p=0.0042). Samples where visible bacteria were observed without addition demonstrated significantly higher positivity rates in the CEP and oAF compared to the NP (p<0.001, p<0.001) and iAF (p<0.0001, p=0.0007) (Figure 4.9).

Comparing the different treatment groups (control, culture control, infection, and visible bacteria at baseline), the control group exhibited a significantly lower *C. acnes* positivity rate in the oAF compared to the infected group (p=0.0243) (Figure 4.9). For *S. aureus*, there were no significant differences across regions between groups, although the infected group showed the highest positivity rate with the lowest standard deviation in the CEP (Figure 4.9). No difference was observed in static versus dynamic loading (Figure 4.9).

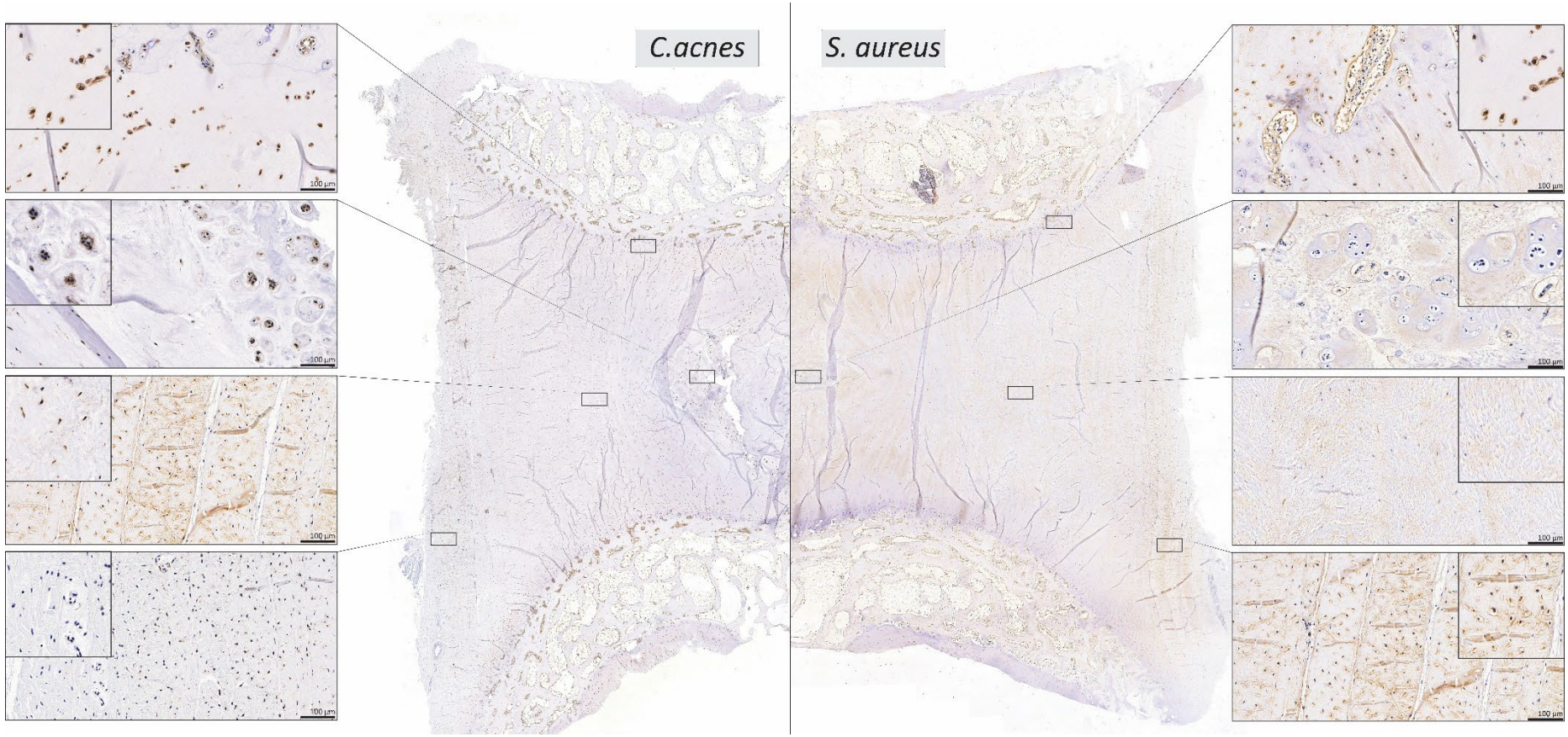

Figure 4.5 | *C. acnes* and *S. aureus* detection within non-cultured control discs

Presence of *C. acnes* lysate (left) and *S. aureus* (right) within non cultured control discs. Brown indicated the detection of the target antibody. Nuclei are counterstained with haematoxylin shown in blue. The regions on the sides show from top to bottom, the cartilaginous endplate, the nucleus pulposus, the inner annulus fibrosus and the outer annulus fibrosus. Scalebars have a length of 100 µm.

4.3.2 CATABOLIC FACTORS

Immunohistochemical staining was performed for the catabolic factors IL-1β, IL-6 (Figure 4.6, Appendix 5), MMP3, and ADAMTS4 (Figure 4.7, Appendix 5), all of which were expressed within bovine IVDs.

Regional comparison in the control group showed no significant differences in the expression of IL-1β, IL-6, or MMP3. However, ADAMTS4 exhibited a significantly higher positivity rate in the CEP and oAF compared to the iAF ($p=0.0039$, $p=0.0083$) (Figure 4.9). In the culture control group, ADAMTS4 also showed a significantly higher positivity rate in the oAF compared to the iAF ($p=0.0478$).

Infected samples demonstrated a significantly higher MMP3 positivity rate in the CEP compared to the iAF ($p=0.034$) and oAF ($p=0.0016$), along with a significantly higher ADAMTS4 positivity rate in the oAF compared to the NP ($p=0.0078$) and iAF ($p=0.0168$) (Figure 4.9). In the samples with visible bacterial growth, regional comparison revealed a significant increase in IL-1β in the oAF compared to the NP ($p=0.0293$). IL-6 expression was significantly higher in the CEP compared to the NP ($p=0.003$) and iAF ($p=0.0004$). MMP3 showed a significantly higher positivity rate in the CEP compared to the iAF ($p=0.0005$) and oAF ($p<0.0001$), and also a significantly higher positivity rate in the NP compared to the oAF ($p=0.0042$) (Figure 4.9). ADAMTS4 expression was significantly higher in the CEP and oAF compared to the NP ($p=0.0208$, $p<0.001$) and iAF ($p=0.0135$, $p<0.001$) (Figure 4.9).

Comparison of the different treatment groups (control, culture control, infection, and visible bacterial growth) showed no significant differences in any region for IL-1β, IL-6, and MMP3. However, ADAMTS4 displayed a significantly higher positivity rate in the visible bacterial growth group compared to the infection group in the CEP ($p=0.0170$) and NP ($p=0.0250$) (Figure 4.9).

4.3.3 TOLL LIKE RECEPTORS WITHIN BOVINE SAMPLES

Staining for TLR-2 and TLR-4 confirmed their presence within bovine tissue (Figure 4.8). Whilst TLR-2 was expressed within all the regions (Positivity Rates; CEP=68.21±20.06, NP=37.89±24.67, iAF=34.73±27.95, oAF=27.9±22.26). TLR-4 showed a very low positivity rate throughout the regions (Positivity Rates; CEP=4.93±2.89, NP=0.28±0.10, iAF=0.088±0.036, oAF=0.312±0.278) and was not detected in all samples (Figure 4.9).

Regional comparison in the control group showed no differences for TLR-2 whilst the positivity rate of TLR-4 was significantly higher in the CEP then in the iAF and oAF (Figure 4.9). The culture control group showed no regional differences for TLR-2 or TLR-4. Within the infection group TLR-2 was significantly higher in the CEP then in the oAF ($p=0.0463$). Regional comparison within the visible bacterial growth group significantly higher positivity rate for TLR-2 in the CEP compared to the oAF ($p=0.0224$) as well as a significantly higher positivity rate for TLR-4 in the CEP compared to the NP ($p<0.001$), iAF ($p<0.001$) and oAF ($p<0.001$) (Figure 4.9).

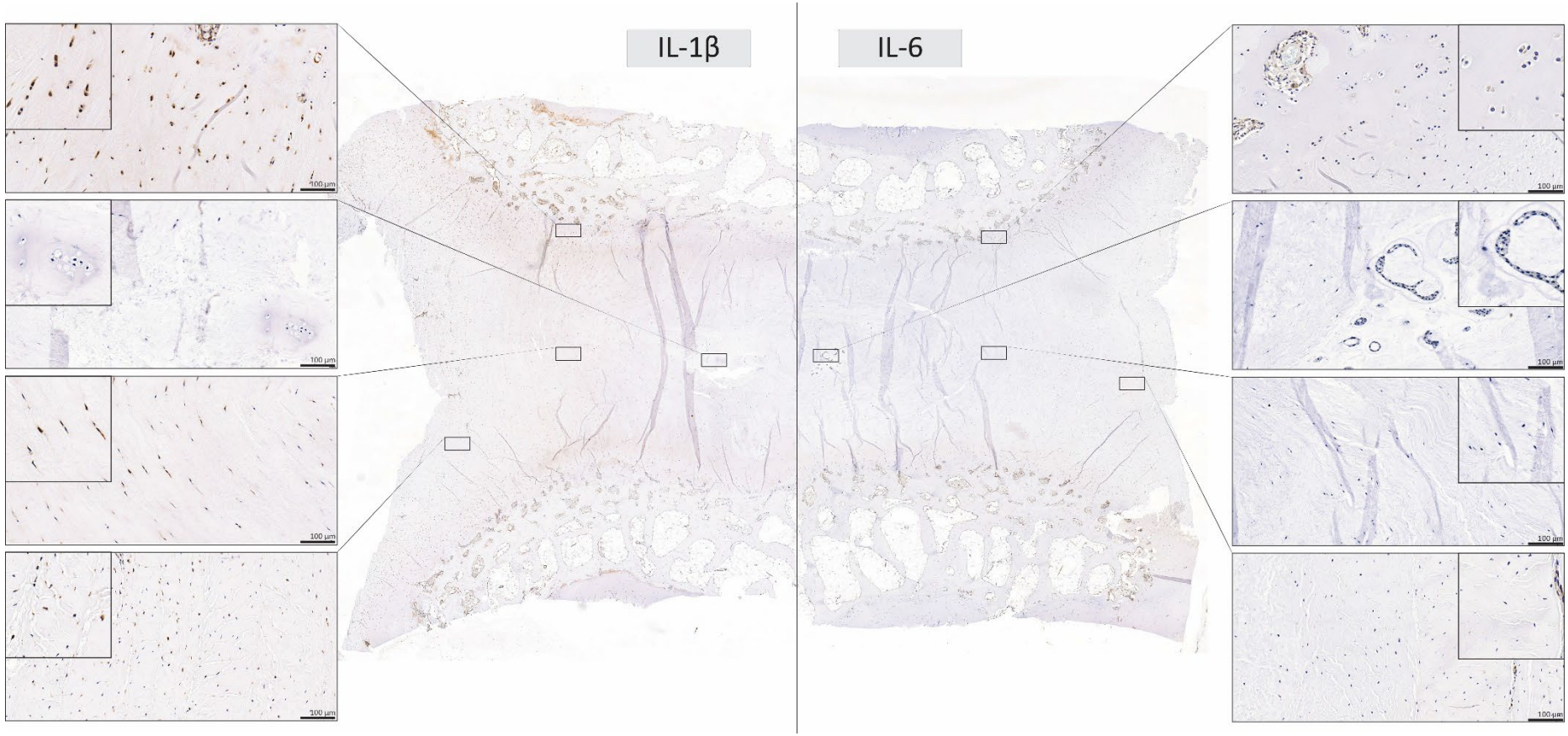

Figure 4.6 | Immunohistochemical staining for IL-1 and IL-6

Presence of IL-1β (left) and IL-6 (right) within non cultured control discs. Brown indicated the detection of the target antibody. Nuclei are counterstained with haematoxylin shown in blue. The regions on the sides show from top to bottom, the cartilaginous endplate, the nucleus pulposus, the inner annulus fibrosus and the outer annulus fibrosus. Scalebars have a length of 100 µm.

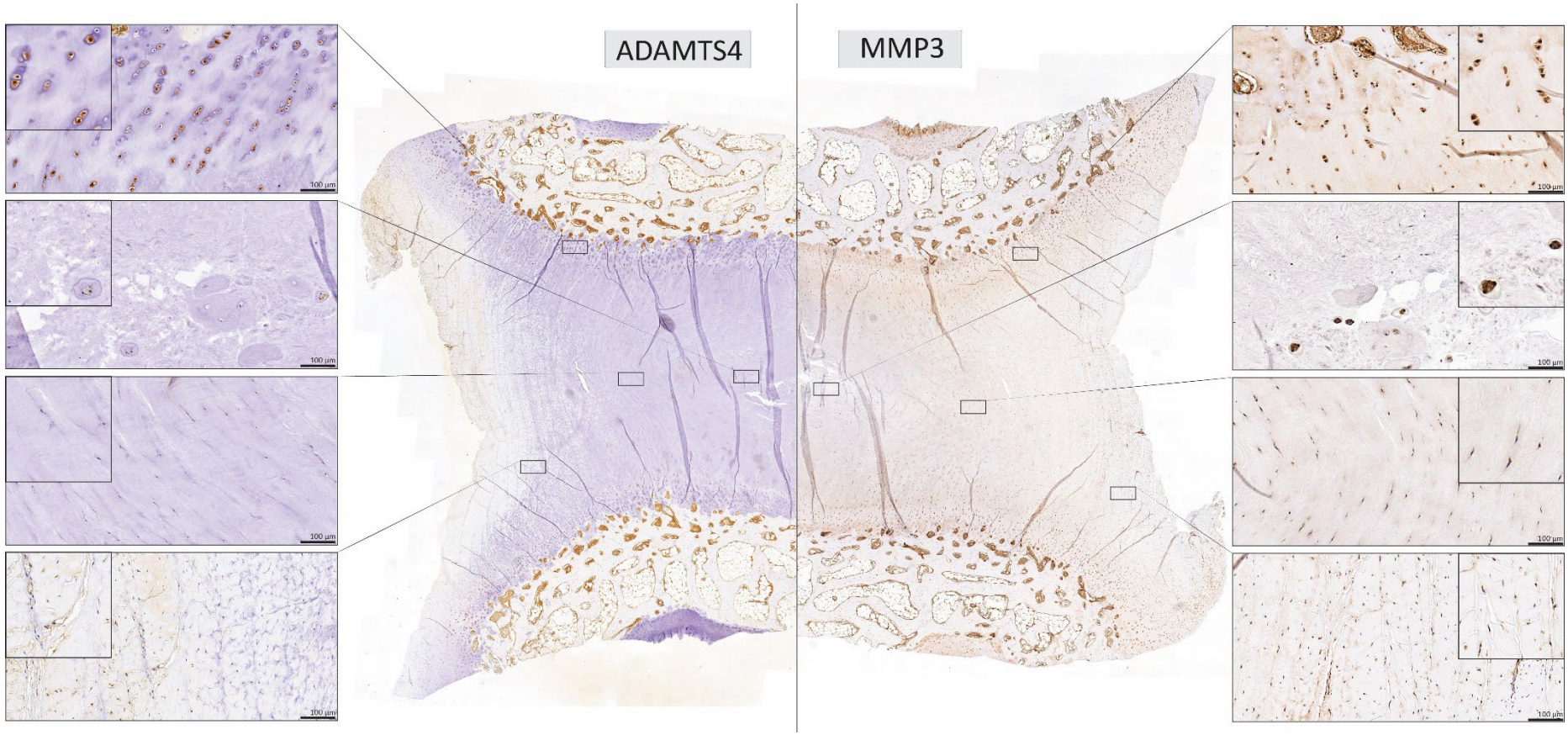

Figure 4.7 | Immunohistochemical staining for ADAMTS4 and MMP3

Presence of ADAMTS4 (left) and MMP3 (right) within non cultured control discs. Brown indicated the detection of the target antibody. Nuclei are counterstained with haematoxylin shown in blue. The regions on the sides show from top to bottom, the cartilaginous endplate, the nucleus pulposus, the inner annulus fibrosus and the outer annulus fibrosus. Scalebars have a length of 100 µm.

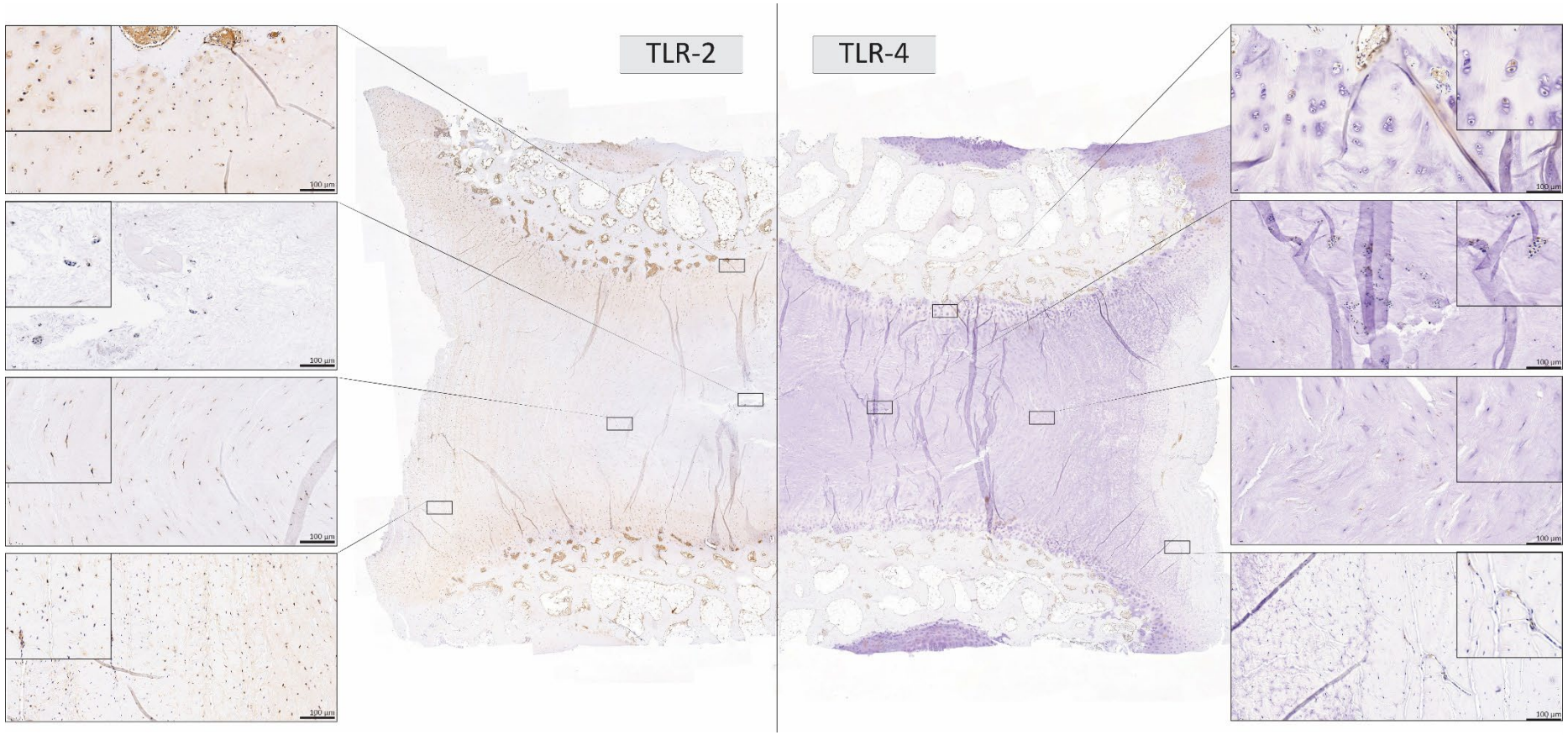

Figure 4.8 | Immunohistochemical staining for TLR-2 and TLR-4

Presence of TLR-2 (right) and TLR-4 (left) within non cultured control discs. Brown indicated the detection of the target antibody. Nuclei are counterstained with haematoxylin shown in blue. The regions on the sides show from top to bottom, the cartilaginous endplate, the nucleus pulposus, the inner annulus fibrosus and the outer annulus fibrosus. Scalebars have a length of 100 µm.

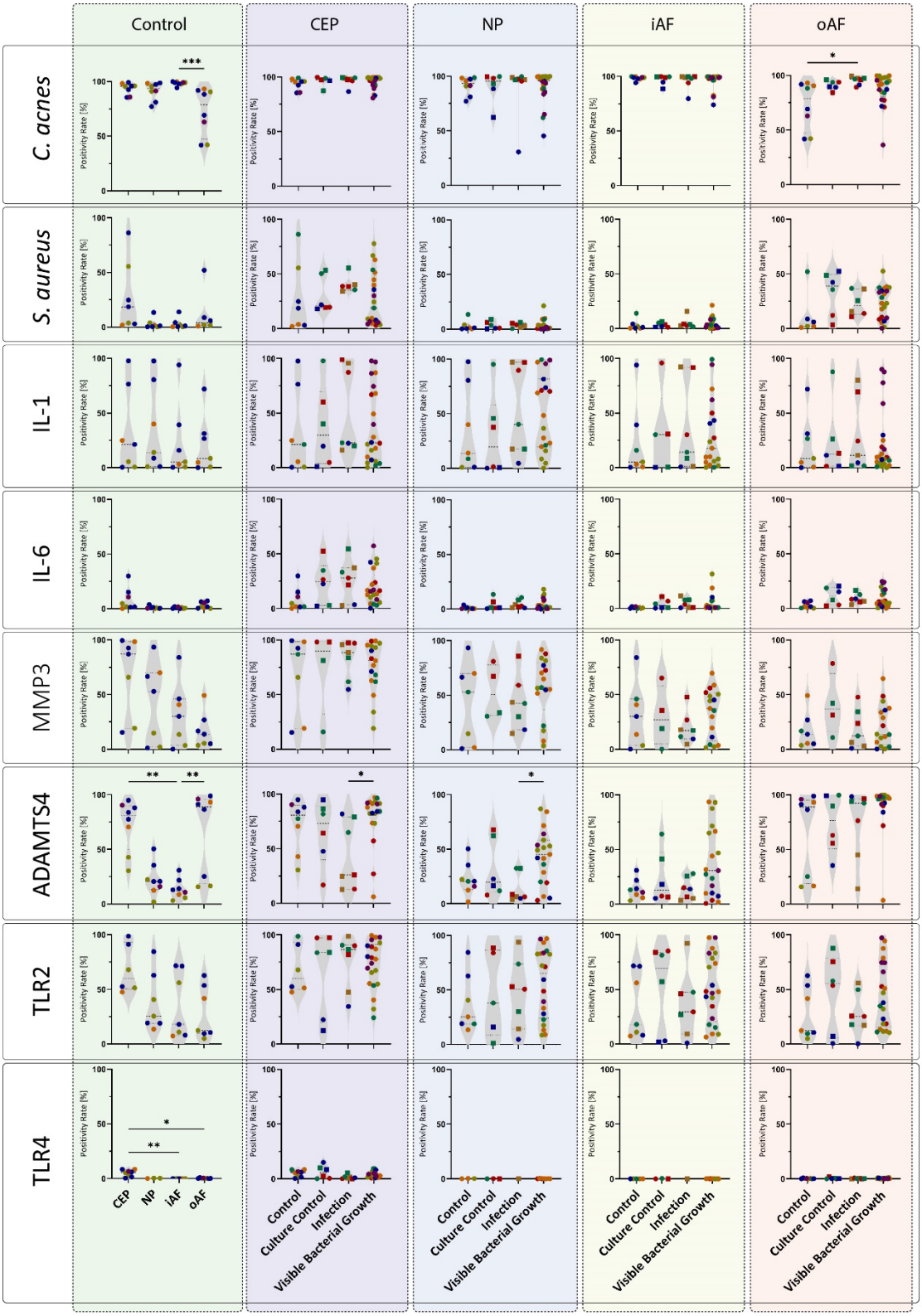

Figure 4.9 | Positivity rates from immunohistochemical staining analysis for each antibody sorted into regions and treatments

The first column represents data from the control group, sorted into the different regions. The other columns represent different regions of the IVD from left to right; cartilaginous endplate (CEP), nucleus pulposus (NP), inner annulus fibrosus (iAF) and outer AF (oAF). Within the regions the samples are shown within the treatment groups. Rows show the different target antibodies. The different colours represent different bovine donors, and the different shapes static loading (square), dynamic loading (triangle) and no loading (round). Statistical analysis was performed using Kruskall-Wallis Dunns multiple comparison ($p \leq 0.05$)

4.3.4 SPEARMAN CORRELATION BETWEEN THE FACTORS

Spearman correlation analyses were conducted to compare the presence of *C. acnes* and *S. aureus* with various stained factors within each region and experimental group (Figure 4.10). In the control group, a strong negative correlation was observed between the positivity rate of *C. acnes* and IL-1 in the outer annulus fibrosus (oAF) (p=0.048, r=-0.79) (Figure 4.10A, Figure 4.11). Additionally, *S. aureus* showed a strong positive correlation with ADAMTS4 in the inner annulus fibrosus (iAF) (p=0.007, r=0.93) (Figure 4.10B, Figure 4.11). In the culture control group, a significant positive correlation between *C. acnes* and TLR2 was identified exclusively in the nucleus pulposus (NP) (p=0.017, r=1) (Figure 4.10C, Figure 4.11). Within the infection group, a strong correlation was found between *S. aureus* and IL-1 (p=0.003, r=1), as well as TLR2 (p=0.017, r=0.094), both in the iAF (Figure 4.10D,E, Figure 4.11). Lastly, in the visible bacterial growth samples, *C. acnes* demonstrated a negative correlation with IL-1 (p=0.012, r=-0.54) and TLR4 (p=0.032, r=-0.49) in the oAF, while showing a positive correlation with ADAMTS4 (Figure 4.10F-H, Figure 4.11).

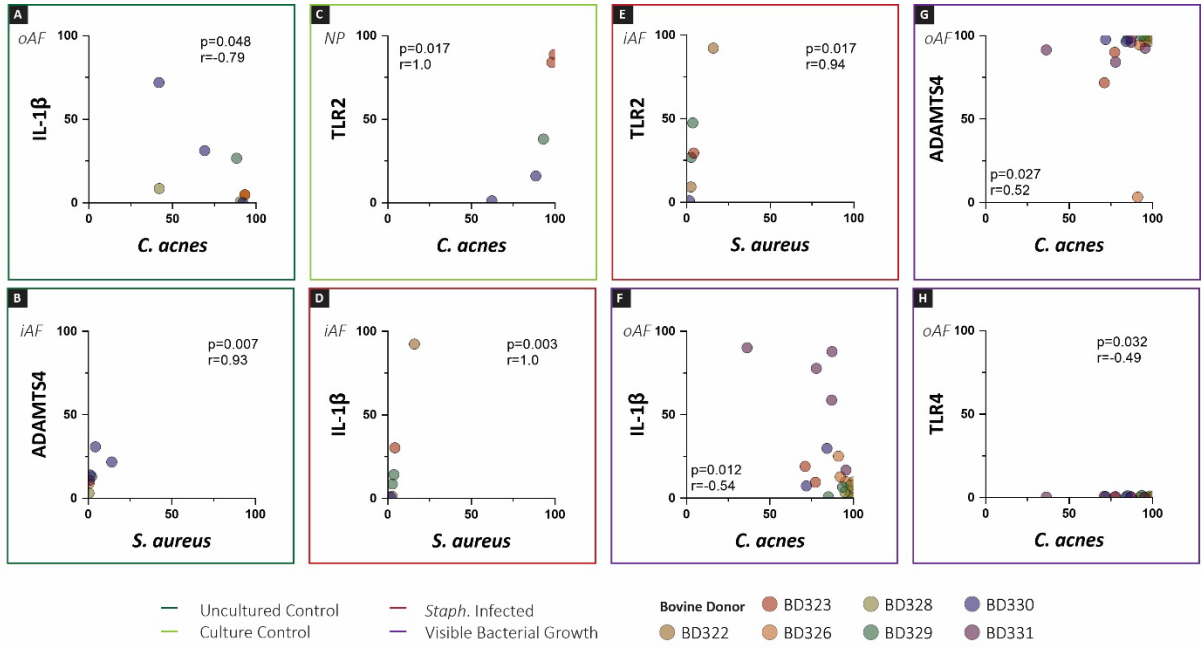

Figure 4.10 | Spearman correlation plotting individual correlations

Spearman correlations detected between the positivity rates of various immunohistochemically stained factors in the uncultured control group (A, B, n=8), the culture control group (C, n=6), the staphylococci-spiked group (D, E, n=7), and the group showing visible bacterial growth (F, G, H, n=22). Different coloured data points represent IVDs from different bovine donors.

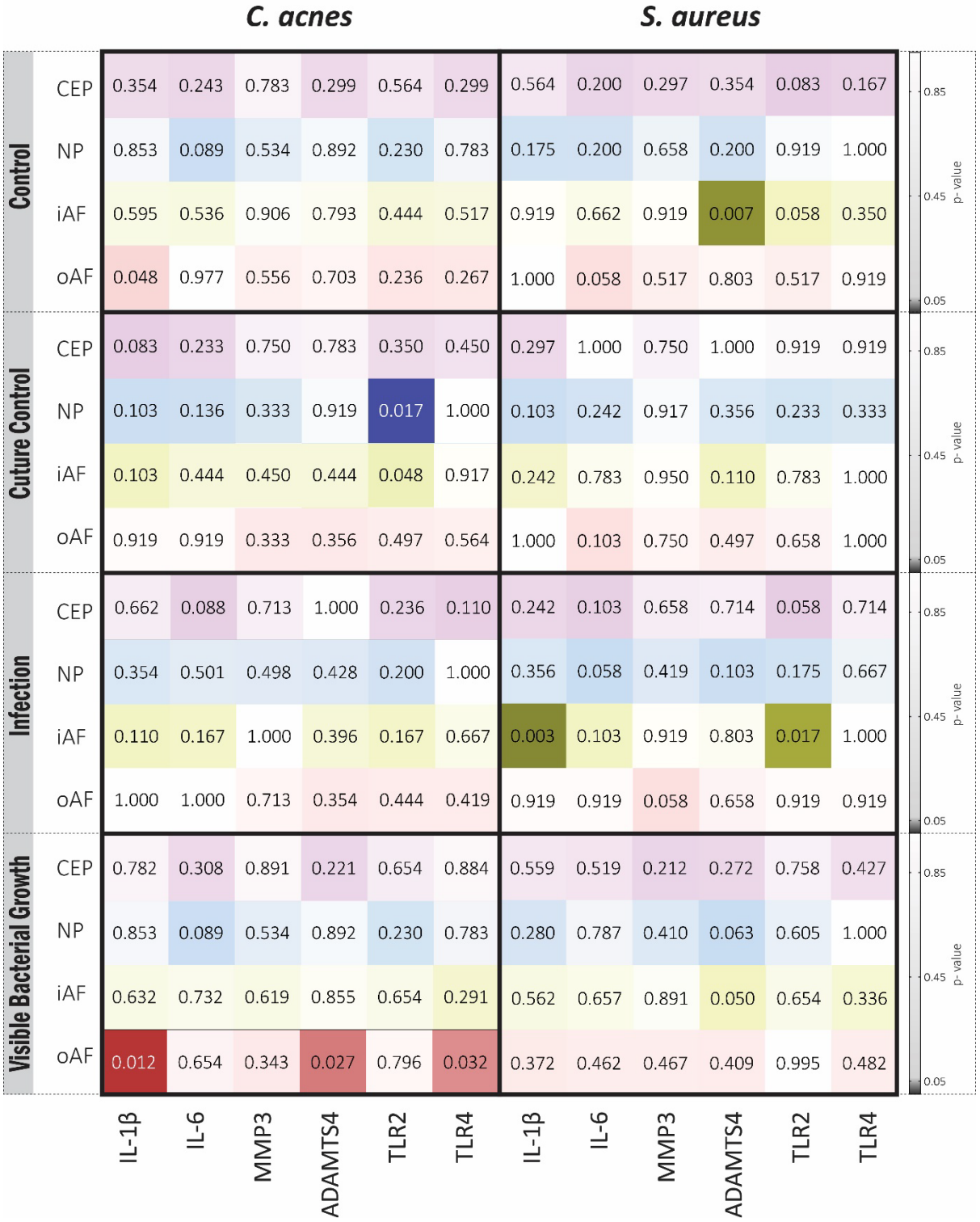

Figure 4.11 | Spearman correlation plotting the p-values

Spearman correlation between the C. acnes and S. aureus and the different factor within the different components of the IVD for the separate groups (control, culture control, infection, and visible bacterial growth) of the study. The different components of the IVD are shown in distinct colours (CEP=purple, NP=blue, iAF=yellow, oAF= red) darker colours indicate a lower p- value (p=0.05).

4.3.5 DNA MEASURED IN COLLECTED MEDIA

To ensure detection of any bacteria in the media, samples were collected regardless of visible signs of contamination. For samples without visible contamination, media was collected both before and after the 24-hour loading period, regardless of *Staphylococci* spiking. For samples with visible contamination during the free swelling period, as indicated by media discoloration, the media was collected upon signs of bacterial growth. DNA was then isolated from the media, and quantification revealed variations among samples. Those with a DNA concentration below 1000 pg/µL were excluded from further analysis (Figure 4.12). DNA concentration was measured using Qubit after initial PCR amplification following the 16S rRNA sequencing protocol.

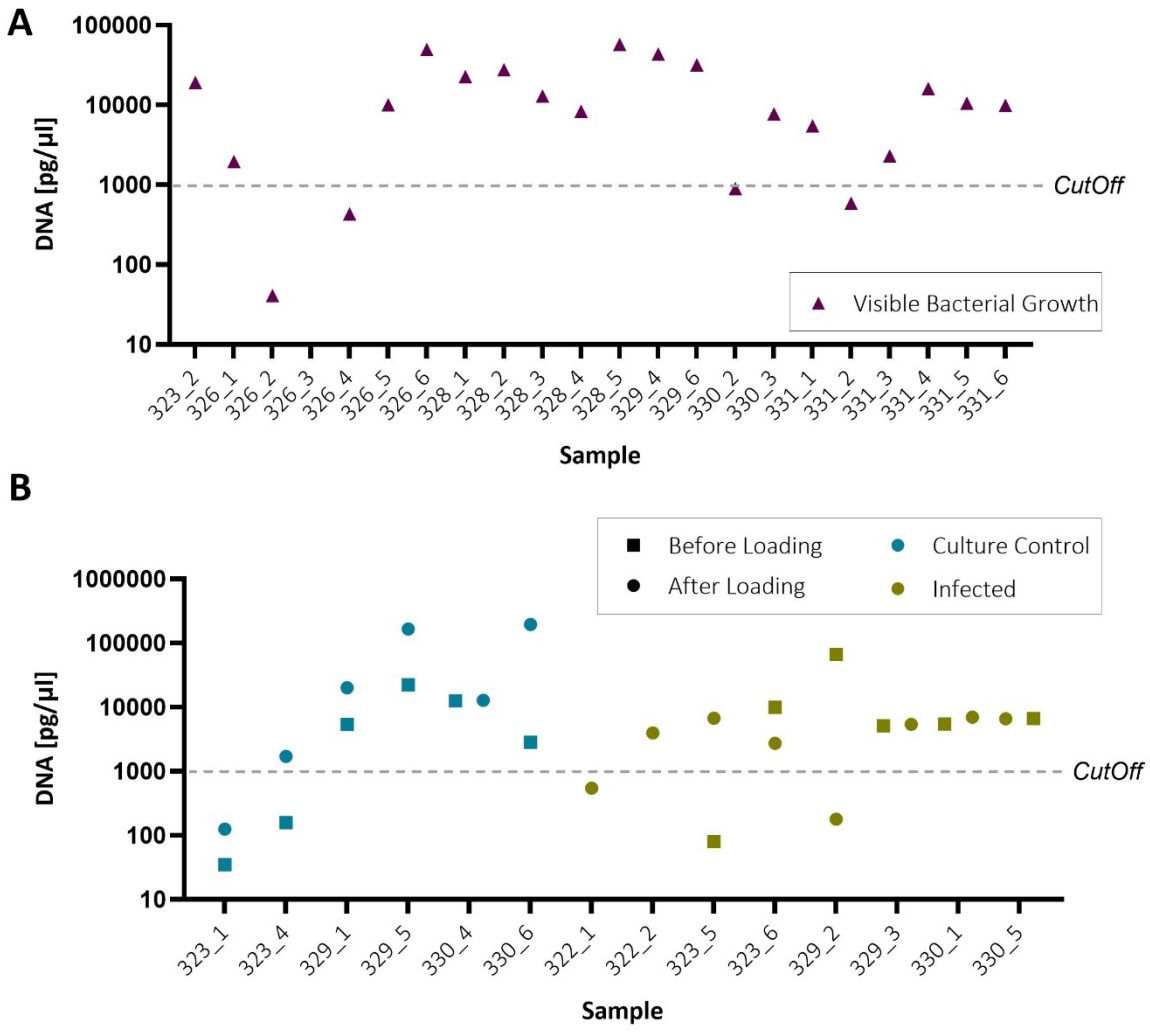

Figure 4.12 | DNA concentration measured isolated from media of cultured IVDs

A Showing the DNA concentration of samples showing visible bacterial growth during the free swelling period, indicated by the colour of the media. **B** DNA concentration of the loaded samples before (square) and after loading (round) grouped in cultured control (blue) or infected samples (green) spiked with Staphylococci.

4.3.6 VISIBLE BACTERIAL GROWTH IN BOVINE IVDS

While samples displayed visible signs of bacterial growth, not all collected samples contained sufficient DNA concentrations for 16S rRNA sequencing (17 out of 22, Figure 4.12A). Additionally, four samples yielded inadequate DNA levels following the initial PCR step. Media from IVDs isolated from the same donor tail exhibited similar bacterial rRNA profiles. Three donors showed the presence of *Citrobacter koseri* and *Pseudocitrobacter faecalis* (Figure 4.13). Furthermore, two of these nine IVDs contained *Escherichia marmotae* rRNA in the media, while one sample revealed *Bacillus anthracis*, *Bacillus cytotoxicus*, and *Bacillus mycoides*. Another donor demonstrated the presence of *Enterococcus faecalis* rRNA, with one of its IVDs also showing *Delftia tsuruhatensis* and *Empedobacter brevis* (Figure 4.13).

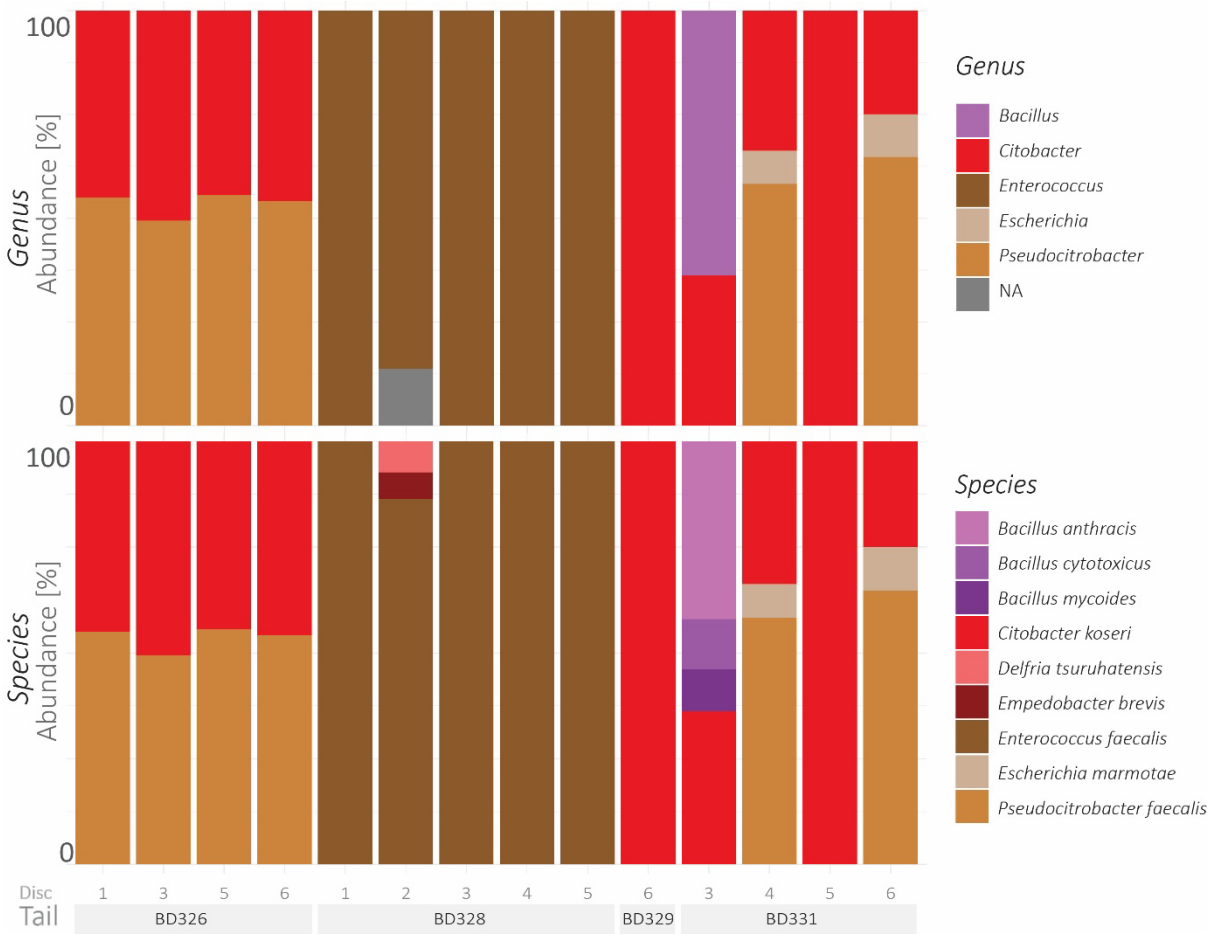

Figure 4.13 | Bacteria detected in media of samples showing visible bacterial growth

Bar charts displaying bacterial abundance detected via 16S rRNA sequencing, presented at both genus (top) and species(bottom) levels. Media was collected during the initial 48 hours of free swelling period of the explant. A 3% abundance cutoff was applied for data visualisation.

4.3.7 BACTERIAL PATTERNS IN BOVINE IVDS LACKING VISIBLE BACTERIAL GROWTH

Not all collected samples had a sufficient DNA concentration for 16S rRNA sequencing. In the pre-loading group, 9 out of 12 samples showed no visible growth but contained DNA (Figure 4.12). In the post-loading group, 5 out of 6 culture control samples showed no visible growth but contained DNA, while 6 out of 8 spiked samples indicated media colour change (Figure 4.12). Some samples did not reach the required DNA concentration (pre-loading 3/9, post-loading; control 3/5; spiked 4/6) following PCR amplification and were thus excluded from sequencing analysis.

Interestingly, samples with no visible bacterial growth, as indicated by the tissue culture media colour, were found to contain bacteria upon 16S rRNA sequencing (Figure 4.14). Detected bacterial rRNA included *Herbaspirillum huttiense*, *Stenotrophomonas cyclobalanopsidis*, and *Stenotrophomonas maltophilia* (Figure 4.13). Following the loading period, one culture control sample also revealed the presence of *Lactococcus garvieae* rRNA in the media. All samples spiked with a *Staphylococci* mix confirmed the presence of *Staphylococci* in the media, although it was not consistently the dominant species (Figure 4.14).

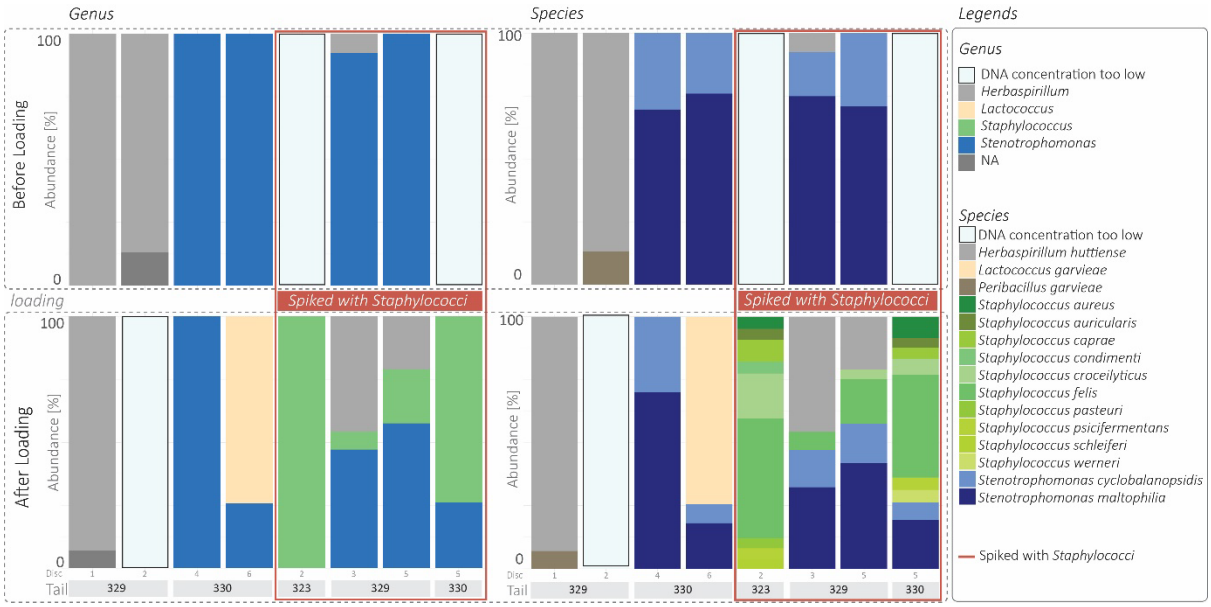

Figure 4.14 | Detected bacteria within the culture control and infection group media

Bar charts displaying the bacterial abundance detected via 16S rRNA sequencing, presented at both the genus (left) and species (right) levels. The upper panels show bacteria detected in the media after the free swelling period, prior to loading, while the lower panels represent the samples collected post-loading. Samples outlined in red were spiked with a mix of *Staphylococci* prior to loading, while those without red outlines represent culture control samples. A 3% abundance cutoff was applied for data visualisation.

4.4 DISCUSSION

This study aimed to investigate the presence of bacteria, particularly *C. acnes* and *S. aureus* in healthy bovine IVDs isolated from the tail, assessing whether these discs naturally harbour bacteria. Additionally, we explored whether bacteria could invade intact IVDs using a whole organ co-culture model. Immunohistochemical staining allowed us not only to detect the presence of bacteria but also to pinpoint differences across the IVD structures and identify potential entry sites upon co-culture. Furthermore, this study examined the culture media from IVD samples, regardless of visible bacterial growth, conducting 16S rRNA sequencing to identify microbes present. The detection of both environmental and gut-related bacteria within the media suggests that bacteria may not have originated from laboratory processing and contamination, but rather from the tissue itself or its surrounding environment.

This study has been performed using IVDs isolated from Swiss cattle. In Switzerland, the regulation of antibiotics in livestock is stringent, prioritising both animal health and food safety. Antibiotics are permitted only for treating sick animals, and there are strict guidelines to minimise their use, particularly prohibiting their use for growth promotion [265]. Similarly, the UK enforces regulations that aim to lower overall antibiotic usage while still allowing treatment for ill animals to combat antibiotic resistance [266]. In the United States, the use of antibiotics for treating sick animals is allowed, but the practice of using them for growth enhancement is being phased out [267]. While all three countries have regulations governing antibiotic use in livestock, Switzerland and the UK implement more rigorous measures to reduce overall consumption, especially concerning antibiotics that are vital for human health. The use of antibiotics in livestock, not only impacts antibiotics resistance, but also the composition of the gut microbiome, and may impact that within the disc.

4.4.1 INTRACELLULAR DETECTION OF *C. ACNES* AND *S. AUREUS* IN INTACT HEALTHY BOVINE IVDs

C. acnes is primarily recognised as a commensal bacterium associated with human skin, but its role in livestock, such as sheep or cows, is much less documented. It has been isolated as a pathogen in rare cases, such as a report of placentitis and abortion in a cow [268]. However, there is limited evidence linking *C. acnes* to significant diseases in cattle. Its potential presence as a commensal organism in livestock, including the bovine gastrointestinal tract or skin, has not been thoroughly explored. In contrast, *S. aureus* is a well-known bacterium in both human and veterinary medicine. It is notably associated with bovine mastitis, which leads to abnormalities in milk and udder swelling [269]. The

bacteria can spread between cows during milking [270] and may cause foodborne illness in humans [271]. However, its role as a commensal organism in livestock has not been extensively studied.

The intracellular detection of *C. acnes* and *S. aureus* in intact healthy bovine IVD tissue, which was fixed immediately after isolation, suggests that these bacteria are present *in vivo* within the disc. This aligns with findings in human IVD tissue, where *C. acnes* show a higher positivity rate than *S. aureus* (Chapter 3). Comparing positivity rates in different regions of the IVD revealed higher *C. acnes* detection in the iAF than the oAF. Since the IVD contains blood vessels only in the CEP and oAF, the oxygen concentration is lower in the iAF and NP. As an aerotolerant anaerobe, *C. acnes* likely prefers these low-oxygen environments, possibly migrating towards the centre. Conversely, *S. aureus*, a facultative aerobe, showed slightly higher detection in the CEP and oAF.

Interestingly, the positivity rate of *C. acnes* displayed a negative correlation with IL-1β in both healthy, uncultured bovine IVDs and those exhibiting visible bacterial growth in the oAF. Conversely, a positive correlation was found with ADAMTS4 in the IVD samples that showed visible bacterial growth. In the study involving human tissue (Chapter 3), no correlation was observed between *C. acnes* and either IL-1 or ADAMTS4, although a correlation with MMP-3 was noted. Similarly, Zheng *et al.* reported a downregulation of aggrecan and collagen type II, along with an upregulation of MMP1, in human tissue where *C. acnes* was identified through 16S rDNA sequencing, compared to *C. acnes*-negative controls, which is consistent with our findings. They also observed a similar pattern, with a downregulation of TIMP-1 and an upregulation of MMP1 in rats inoculated with *C. acnes* versus non-inoculated controls [272]. However, the limited sample size in this study highlights the need for further research involving additional donors, as well as the identification of strains and other bacterial species present.

A strong correlation was observed between the positivity rate of *S. aureus* and TLR2, as well as IL-1 in the iAF of discs infected with *Staphylococcus* species. These findings suggest that the phylotype used for infection may possess a higher pathogenic potential compared to those detected in healthy intervertebral discs, as this correlation was only evident in the infected samples [253]. However, specific staining for *S. aureus* alone, which was initially thought to have been used for the infection, was insufficient, as the spiking was carried out with a mixture of *staphylococci*, as subsequently identified with 16s rRNA sequencing. Therefore, IHC staining will need to be performed for *Staphylococcus* in general.

4.4.2 ENVIRONMENTAL AND GUT-RELATED BACTERIA GROWTH IN MEDIA OF DISC SAMPLES

In samples showing bacterial growth in the media, bacterial rRNA detected included *Citrobacter koseri*, *Pseudocitrobacter faecalis*, *Escherichia marmotae*, *Bacillus anthracis*, *Bacillus cytotoxicus*, and *Bacillus mycoides*. The *Bacillus* genus is abundant in soil and plays a role in plant health and nutrition [273]. Species of *Bacillus* are commonly detected in plant roots and can be transmitted to grasing animals via contaminated soil. Similarly, *Citrobacter* species are widespread in water, soil, and food, and can occasionally colonise the gastrointestinal tracts of humans and animals [274,275]. *Pseudocitrobacter faecalis* is another gut microbiome species, and both *C. koseri* and *P. faecalis* have been isolated from untreated cow milk [276]. *Escherichia marmotae*, a bacterium with relatively low pathogenicity, has been isolated from fecal samples of wild marmots, boars, farm cows, and healthy farm hens [277–279].

Bacterial rRNA detected in the media of non-visibly bacterial growth samples primarily included the genera *Herbaspirillum* and *Stenotrophomonas*, both commonly associated with environmental sources. *Herbaspirillum* species, are Gram-negative nitrogen-fixing bacilli from the class *Betaproteobacteria*, are typically found in plants, soil, groundwater, and drinking water systems [280]. Notably, *Herbaspirillum huttiense*, an aerobic strain, has been isolated from water sources [281] and is considered an emerging human pathogen, with documented cases of pneumonia, septicemia, and bacteremia [282–284]. Likewise, *Stenotrophomonas*, a highly adaptable environmental genus, is frequently isolated from plants and soil. While infections caused by *Stenotrophomonas cyclobalanopsidis* are not well-documented in humans, its close relative *Stenotrophomonas maltophilia* is recognised as an opportunistic pathogen, associated with severe infections such as pneumonia, bacteremia, and wound infections, particularly in immunocompromised patients [285–287].

The presence of this combination of environmental and gut-related bacteria suggests that the bacteria detected in the media of the samples may not stem from the processing procedures but rather from the sample tissue or its surrounding environment. One possible explanation for these findings could be bacterial translocation, the migration of indigenous gut bacteria across the intestinal mucosa into normally sterile tissues [288]. Recent studies, such as that by Rajasekaran *et al.*, have proposed that gut dysbiosis, coupled with changes in gut inflammatory status, erosion of the mucosal barrier, and a reduction in beneficial short-chain fatty acids, can increase the circulation of bacteria, pathobionts, bacterial products, and inflammatory metabolites. These factors may induce disc endplate changes and facilitate bacterial invasion into the IVD [289].

As the bacterial DNA was extracted solely from the culture media rather than directly from the IVD tissue, this detection method may not accurately reflect the true bacterial presence within the disc. Although bacteria may have migrated out of the discs during the culturing process, the collection of

media and subsequent sequencing could preferentially identify those bacteria that thrived under the specific culture conditions established. For instance, *C. acnes* was detected via immunohistochemical staining within the tissue, but not in the media. Since *C. acnes* is an anaerobic bacterium, its growth in media with 21% oxygen would have posed significant challenges.

The bacterial rRNA detected in samples exhibiting visible bacterial growth was attributed to *Citrobacter koseri*, *Pseudocitrobacter faecalis*, *Escherichia marmotae*, and various *Bacillus* species, all of which are capable of thriving under aerobic conditions with rapid growth rates [290–292]. In contrast, the bacterial rRNA detected in samples that showed no signs of contamination included *Herbaspirillum* and *Stenotrophomonas*, which are facultative anaerobes known to thrive in aerobic environments, albeit at slower growth rates [293]. Additionally, the detected bacteria may have originated from surrounding tissues.

Given the sterilisation of tissue surfaces with a high concentration of antibiotics before culturing, the detected bacteria are likely either antibiotic-resistant strains, insensitive to the antibiotics used, or may have migrated from the tissue during the culturing period. Additionally, spore-forming bacteria like *Bacillus* are notably resilient under adverse conditions, including exposure to antibiotics [294]. The impermeable structure of spores restricts antibiotic entry, while their minimal metabolic activity renders many antibiotics, including P/S used in this study, ineffective since they primarily target actively dividing cells [295]. This observation raises an important question: are these bacteria naturally embedded within the disc tissue and able to withstand the harsh disc environment, or are they external contaminants that persisted despite sterilisation efforts?

To address this question, a combination of next-generation sequencing for tissue samples and immunohistochemical staining should be employed. This approach would not only detect bacteria but also allow for their localisation and the investigation of regional differences. Furthermore, the metabolic activity of the bacterial cells should be investigated, which could be achieved by performing qPCR to detect dormancy-related genes [296,297]. Ultimately, combining these molecular and imaging techniques will provide a comprehensive understanding of bacterial presence, localisation, and metabolic state within tissue, shedding light on whether these bacteria are resident within the tissue or introduced as contaminants.

4.4.3 BACTERIA CAN INVADE INTACT IVDS

It has been suggested that bacteria detected in human discs may reach structurally damaged discs via haematogenous spread from distant infections, or from the skin or other epithelial surfaces through the bloodstream after minor injuries [259,260]. However, bacteria have been identified in non-herniated human discs (Chapter 3), normal discs from organ donors [147], as well as in intact bovine discs within this chapter, indicating that bacteria can invade undamaged IVDs. In our bovine model, the detection rate of *S. aureus* was higher and showed a smaller standard deviation in the infected group compared to the non-culture control group, particularly in the CEP and outer AF. This supports the hypothesis that bacteria can penetrate an intact disc and leads to the assumption that the primary entry point may be through the CEP and outer AF, the only vascularised structures of the IVD [298]. However, initially, the infection protocol was thought to be of a pure *S. aureus* culture, and therefore immunohistochemical staining was conducted exclusively for *S. aureus*. However, following 16s sequencing it was shown that a considerable proportion of other *Staphylococci* species, unintentionally introduced into the media for the bovine explants, these species may have gone undetected during the IHC analysis due to the targeted staining approach and thus it would be beneficial to complete IHC for a broad-spectrum *Staph* antibody.

4.4.4 CONCLUSION

This study adds further evidence to the hypothesis that IVDs may harbour their own microbiome. The immunohistochemical detection of *C. acnes* and *S. aureus* within non-cultured, directly isolated bovine IVDs strongly supports the presence of bacteria in intact discs. The higher immunopositivity staining for *S. aureus* observed in the CEP and outer AF of cultured discs spiked with *Staph.* species, compared to control discs, suggests that bacterial invasion of the IVD may occur via blood circulation.

Correlations, both positive and negative, between bacterial presence and matrix-degrading enzymes or catabolic factors highlight the need for further research to fully understand the impact bacteria can have on disc cells. Moreover, the influence of bacterial phylotypes should be investigated, as different strains and species may elicit varied cellular responses.

Lastly, 16S rRNA sequencing identified environmental and gut-related bacteria in the media, indicating that bacterial growth may not stem from laboratory processing, but rather from the tissue itself or its surrounding environment. This finding underscores the importance of considering potential external sources of bacterial abundance when studying the IVD microbiome.

ACKNOWLEDGEMENTS

We are grateful for the financial support provided by the Marie Skłodowska Curie International Training Network (ITN) "Disc4All." We would also like to express our thanks to Dr. Junhua Wang (University of Bern) for facilitating our introduction to the microbiology lab in Bern. Additionally, we extend our appreciation to Oliver Heaney (University of Sheffield) for his guidance on 16S rRNA sequencing. Furthermore, we would like to thank the Slaughterhouse in Interlaken for providing us with the bovine tails.

ROLE OF THE FUNDING SOURCE

Financial support was received from the Marie Skłodowska Curie International Training Network (ITN) “disc4all” (https://disc4all.upf.edu, accessed on 10 May 2022) grant agreement #955735 (https://cordis.europa.eu/project/id/955735, accessed on 26 Sept 2024).

CHAPTER 5

GENERAL DISCUSSION AND FUTURE DIRECTIONS

GENERAL DISCUSSION AND FUTURE DIRECTIONS

5.1 SUMMARY OF RESULTS

This thesis aimed to explore the presence and role of bacteria in IVD tissue, distinguishing between perioperative contamination and true *in vivo* bacterial colonisation. A particular focus was placed on the correlations between bacterial presence and catabolic factors, as well as the potential signalling pathways activated upon bacterial exposure. Chapter one as an introduction summarised existing studies suggesting the presence of a microbiome within the IVD, highlighting the need for further investigation into bacterial colonisation in discs. Chapter 2 introduced a semi-automatic quantification method for analysing immunohistochemically stained slides of low-cellularity tissues to improve accuracy and consistency. This chapter also evaluated inter-rater reliability by comparing results from multiple groups performing immunohistochemistry and benchmarking these results against manual counting. In Chapter 3, immunohistochemical evidence of *in vivo* presence of *C. acnes* and *S. aureus* in IVD tissue was presented. Additionally, *C. acnes* presence correlated with the positivity rate of NOD2, MMP3, and GSDMD, with NOD2 not previously shown to be expressed in the disc. Utilisation of a co-culture experiment, where inhibition of NOD2 and TLRs was deployed, suggested that TLRs may not be the sole receptors in bacterial recognition within the IVD. Instead, other PRRs, such as NLRP3, may play a crucial role although these other receptors require investigation. These results underscore the complex interplay of multiple receptors and pathways in the disc's response to bacterial presence, providing a foundation for further research. In Chapter 4, we demonstrated that not only human IVDs but also healthy bovine discs harbour bacteria, with regional differences in bacterial distribution observed within the IVD. Evidence was also presented supporting the hypothesis that bacterial invasion of the IVD may occur through the endplates and annulus fibrosus. Collectively, these findings support the hypothesis that the IVD harbours a microbiome and provide valuable insights into bacterial presence and its influence on IVD tissue. They also highlight the need for further investigation into the underlying mechanisms of bacterial action within the disc, and particularly investigation into what bacteria may represent normal flora and which may be involved in the pathogenesis of disc degeneration and Modic change.

5.2 FUTURE DIRECTIONS

5.2.1 THEORETICAL PATHWAYS OF BACTERIAL ENTRY INTO THE INTERVERTEBRAL DISC

There are two theoretical possibilities for how bacteria might enter the IVD; either they are present from birth, inherited from the mother, or they infiltrate the disc later in life. In the case of the gut microbiome, for example, an initial microbiome is formed *in utero* [299]. Upon birth, additional bacteria are acquired from the mother's vaginal or skin microbiome, depending on the type of delivery [300,301] as well as via mothers' milk [302]. Throughout life, environmental factors, such as diet and antibiotic use, play a greater role in shaping the gut microbiome than host genetics [303]. However, unlike the gut, vaginal, and other epithelial microbiomes, the disc lies behind the body's epithelial barriers, suggesting that the mechanism of microbiome development in the disc may differ.

The second possibility is that bacteria invade the disc later in life. Bacteria may translocate from the gut across the epithelial barrier into the bloodstream and subsequently into other tissues. This translocation has been linked to gut dysbiosis, which can lead to a "leaky gut" and has been implicated in various non-infectious diseases, including osteoarthritis [304] and multiple sclerosis [305]. A gut-disc axis has been proposed [306], and comparative metagenomic analyses of the disc, skin, and gut microbiomes show a significant overlap of bacterial species between the disc and gut, but only a small overlap with the skin. This further supports the idea of crosstalk between the disc and the gut [147].

Findings from Chapters 3 and 4 indicate the presence of bacteria within intact IVDs, but it remains unclear whether these bacteria have been present since birth or colonised the discs later in life. The detection of gut-related bacteria in the media of bovine samples raises the possibility of bacterial translocation from the gut. Further research is needed to explore the origins and pathways of these bacteria within the IVD. Animal models, including studies on foetuses, could help determine bacterial presence before birth, while models with altered gut microbiomes or diets could examine how specific gut compositions influence the disc microbiome. The effect of mechanical loading also warrants further study. Although the positivity rate of *S. aureus* did not differ between statically loaded and physiologically dynamically loaded discs, this may not fully capture the situation, as a mixture of *Staphylococci* was used, as noted in Chapter 4. The precise role of loading in bacterial invasion remains unclear and requires further investigation.

5.2.2 POTENTIAL ROLE OF MICROBIOME WITHIN THE PATHOGENESIS OF MODIC CHANGE AND DISC DEGENERATION

MC and IVD degeneration are strongly associated with LBP [307–310]; however, their pathogenesis remains poorly understood. As outlined in Chapter 1, the mechanisms behind disc degeneration are complex, involving inflammatory, catabolic, neurotrophic, and pro-angiogenic processes that contribute to both disc degeneration and pain [10,65,79]. Inoculation of *C. acnes* into caudal IVDs has been shown to induce disc degeneration in both rats [143,144] and rabbits [145,146]. However, these studies primarily examined the effects of *C. acnes* on disc degeneration, without exploring whether the bacteria were already present in intact discs or if they could naturally invade healthy IVDs. The aetiology of MC1 is thought to involve bacterial and autoimmune components [132,311–313]. Notably, discs adjacent to MC1 have been found to contain higher levels of *C. acnes* [314,315] compared to degenerated discs without MC, suggesting that *C. acnes* in the disc space may contribute to MC1 development.

The varying bacterial abundance observed across non-degenerate, degenerate, herniated, and MC-associated discs points to disc dysbiosis as a potential factor in both disc degeneration and MC development [138,147]. While our studies focused on staining for specific bacteria, leaving the broader disc microbiome unaddressed, the emerging concept of a disc microbiome and its alterations raises critical questions about which bacteria are commensal, and which are pathogenic. As discussed briefly in Chapter 3, the bacterial phylotype is also important, as different strains may elicit varied responses from disc cells upon stimulation and should be considered in future study designs.

Future research should employ NGS to analyse IVD microbiomes across donor cohorts, including healthy, degenerated, and MC-associated discs. A study comparing NGS results from Swiss and Indian IVD donors revealed discrepancies in the detected microbes [138], highlighting the need for standardised protocols in sample preparation and bioinformatic analysis. These findings also suggest the possibility of biological and environmental differences, underscoring the importance of reporting donors' geographical location, lifestyle, and diet in future studies.

Results from our bovine study, discussed in Chapter 4, revealed regional differences in the positivity rate of *C. acnes*, suggesting that the microbiome composition within the IVD may vary slightly by region. These differences could be attributed to variations in oxygen concentration and nutrient supply across the disc. This should be considered in future studies, as samples from different regions may yield distinct results.

5.2.3 IMMUNE SURVEILLANCE IN THE IVD

The IVD is traditionally viewed as an immune-privileged organ, meaning it generally lacks immune cells. However, native NP cells have been shown to take on immune-like functions, such as phagocytosis. Jones *et al*. (2008) demonstrated that bovine NP cells are capable of efficiently ingesting latex beads and apoptotic cells, a task typically performed by phagocytic cells [111]. In Chapters 3 and 4, immunohistochemical staining revealed that bacteria were primarily detected within cells. Additionally, in Chapter 3, we showed that after just one hour of co-culturing NP cells with *S. aureus*, the bacteria could be detected intracellularly. This observation aligns with previous studies where *C. acnes* was co-cultured with disc cells *in vitro*, leading to an inflammatory response, the release of neurotrophic factors, and bacterial internalisation [316]. The exact mechanism behind this internalisation process is not yet fully understood and warrants further investigation through controlled *in vitro* experiments.

As discussed in Chapter 1, PRRs have primarily been studied in dendritic cells, macrophages, epithelial cells, endothelial cells, and fibroblasts [317]. However, the downstream signalling pathways of PRRs in disc cells are not yet fully understood. Within IVD cells, only TLRs and NLRP3 have been identified and studied in more detail to date [151,318].

In Chapter 3, we reported the expression of NOD2 in human IVD tissue and demonstrated its correlation with the presence of *C. acnes*. Additionally, we found a link between *C. acnes* positivity and the pyroptosis marker GSDMD, which is associated with NLRP3 activation. These findings suggest that TLRs may not be the dominant receptors in response to bacterial stimulation. Furthermore, inhibiting TLR2 and NOD2 did not significantly reduce the catabolic response upon bacterial stimulation, indicating that multiple receptors may be involved.

To gain a deeper understanding of PRRs in the disc, further research is necessary. Immuno-histochemical staining should be employed to investigate the presence and distribution of PRRs in disc cells as well as their correlation to bacterial presence within the tissue, while *in vitro* studies combining receptor stimulation and inhibition could help clarify the roles of different receptors in disc cell responses to bacterial exposure.

5.2.4 ANTIBIOTICS TREATMENT

Several clinical trials examining the impact of oral antibiotic treatment in patients with MC1 have yielded inconsistent results. Some studies found no significant advantages of antibiotic treatment over placebo [141,142], while others reported notable benefits when compared to the placebo group [139,140,319]. However, antibiotic therapy can negatively impact gut microbiota diversity, disrupting host-microbe interactions, immune system balance, and colonisation resistance against new pathogens [320]. In fact, antibiotic treatments can exacerbate conditions like inflammatory bowel disease by interfering with TLR signalling, leading to changes in gut microbiome diversity that have been linked to long-term health issues, such as obesity and diabetes [321–323].

Administering antibiotics to all patients with LBP and signs of MC without a clear understanding of which pathological disc changes to target, which bacteria to treat, and how the treatment affects both the gut and disc microbiomes is imprudent. While there may be potential benefits, antibiotic treatment could also eliminate beneficial disc bacteria and increase the risk of antibiotic resistance. Therefore, further investigation into the disc microbiome and a more targeted approach to treatment are essential before considering the widespread use of oral antibiotics in these patients.

5.3 CONCLUSION STATEMENT

In conclusion, this thesis provides strong evidence for the presence of *C. acnes* and *S. aureus* within non-herniated human and bovine IVDs, supporting the hypothesis that discs harbour their own microbiome. The immunohistochemical detection of bacteria within NP cells, along with correlations between *C. acnes* and catabolic markers like MMP-3, GSDMD, and NOD2, suggests an active immune role for NP cells in bacterial surveillance. Notably, the expression of NOD2 by native disc cells highlights previously unrecognised intracellular mechanisms of bacterial detection and inflammation. Although low bacterial loads did not induce significant MAPK or NFkB pathway activation, prior studies indicate that higher bacterial burdens may elicit stronger cellular responses, emphasising the importance of bacterial load and exposure time in disc pathology. Furthermore, different bacterial strains might induce different cellular responses. In bovine IVDs, the increased presence of *S. aureus* in the CEP and outer AF of spiked cultured and loaded discs supports the notion of bacterial invasion through blood circulation. Furthermore, the identification of environmental and gut-related bacteria through 16S rRNA sequencing points to potential non-laboratory sources of bacterial contamination, underscoring the complexity of the disc microbiome. The observed correlations between bacterial presence and matrix-degrading enzymes and other catabolic factors suggest a multifaceted interaction between bacteria and disc cells, opening avenues for future research on how different bacterial strains influence disc health.

SECTION 6 REFERENCES

REFERENCES

1. Bermudez-Lekerika, P. *et al.* Immuno-Modulatory Effects of Intervertebral Disc Cells. **10**, 924692 (2022).

2. James, S. L. *et al.* Global, regional, and national incidence, prevalence, and years lived with disability for 354 Diseases and Injuries for 195 countries and territories, 1990-2017: A systematic analysis for the Global Burden of Disease Study 2017. *The Lancet* **392**, 1789–1858 (2018).

3. Adams, M. A., Freeman, B. J. C., Morrison, H. P., Nelson, I. W. & Dolan, P. Mechanical initiation of intervertebral disc degeneration. *Spine (Phila Pa 1976)* **25**, 1625–1636 (2000).

4. Battié, M. C. *et al.* 1991 volvo award in clinical sciences: Smoking and lumbar intervertebral disc degeneration: An MRI study of identical twins. *Spine (Phila Pa 1976)* **16**, 1015–1021 (1991).

5. Hangai, M. *et al.* Factors associated with lumbar intervertebral disc degeneration in the elderly. *Spine Journal* **8**, 732–740 (2008).

6. Battié, M. C., Videman, T. & Parent, E. Lumbar disc degeneration: Epidemiology and genetic influences. *Spine (Phila Pa 1976)* **29**, 2679–2690 (2004).

7. Battié, M. C. & Videman, T. Lumbar disc degeneration: Epidemiology and genetics. *Journal of Bone and Joint Surgery* **88**, 3–9 (2006).

8. Feng, Y., Egan, B. & Wang, J. Genetic factors in intervertebral disc degeneration. *Genes Dis* **3**, 178–185 (2016).

9. Smith, L. J., Nerurkar, N. L., Choi, K., Harfe, B. D. & Elliott, D. M. Degeneration and regeneration of the intervertebral disc : lessons from development. *Disease Models & Mechanism* **41**, 31–41 (2011).

10. Raj, P. P. Intervertebral disc: anatomy-physiology-pathophysiology-treatment. *Pain Practice* **8**, 18–44 (2008).

11. Urban, J. P. G. The role of the physicochemical environment in determining disc cell behaviour. *Biochem Soc Trans* **30**, 858–864 (2002).

12. Yao, Y. *et al.* General regulatory effects of hypoxia on human cartilage endplate-derived stem cells: A genome-wide analysis of differential gene expression and alternative splicing events. *Mol Med Rep* **16**, 3001–3009 (2017).

13. Lama, P. *et al.* Significance of cartilage endplate within herniated disc tissue. *Eur Spine J* **23**, 1869–1877 (2014).

14. Roberts, S., Menage, J. & Urban, J. P. Biochemical and structural properties of the cartilage endplate and its relation to the intervertebral disc. *Spine (Phila Pa 1976)* **14**, 166–174 (1989).

15. Berg-Johansen, B. *et al.* Cartilage Endplate Thickness Variation Measured by Ultrashort Echo-Time MRI is Associated with Adjacent Disc Degeneration. *Spine (Phila Pa 1976)* **43**, E592–E600 (2018).

16. Roberts, S., Evans, H., Trivedi, J. & Menage, J. Histology and Pathology of the Human Intervertebral Disc. *Journal of Bone and Joint Surgery* **88**, 10–14 (2006).

17. Oda, J., Tanaka, H. & Tsuzuki, N. Intervertebral disc changes with aging of human cervical vertebra from the neonate to the eighties. *Spine (Phila Pa 1976)* **13**, 1205–1211 (1988).

18. Moore, R. J. The vertebral endplate: disc degeneration, disc regeneration. *Eur Spine J* 333–337 (2006) doi:10.1007/S00586-006-0170-4.

19. Zhao, F. D., Pollintine, P., Hole, B. D., Adams, M. A. & Dolan, P. Vertebral fractures usually affect the cranial endplate because it is thinner and supported by less-dense trabecular bone. *Bone* **44**, 372–379 (2009).

20. DeLucca, J. F. *et al.* Human cartilage endplate permeability varies with degeneration and intervertebral disc site. *J Biomech* **49**, 550–557 (2016).

21. Wallace, A. L., Wyatt, B. C., McCarthy, D. & Hughes, S. P. Humoral regulation of blood flow in the vertebral endplate. *Spine (Phila Pa 1976)* **19**, 1324–1328 (1994).

22. Wong, J. *et al.* Nutrient supply and nucleus pulposus cell function: effects of the transport properties of the cartilage endplate and potential implications for intradiscal biologic therapy. *Osteoarthritis Cartilage* **27**, 956–964 (2019).

23. Shirazi-Adl, A., Taheri, M. & Urban, J. P. G. Analysis of cell viability in intervertebral disc: Effect of endplate permeability on cell population. *J Biomech* **43**, 1330–1336 (2010).

24. Roberts, S., Urban, J. P. G., Evans, H. & Eisenstein, S. M. Transport properties of the human cartilage endplate in relation to its composition and calcification. *Spine (Phila Pa 1976)* **21**, 415–420 (1996).

25. Hodgkinson, T., Kelly, D. C., Curtin, C. M. & O'Brien, F. J. Mechanosignalling in cartilage: an emerging target for the treatment of osteoarthritis. *Nat Rev Rheumatol* **18**, 67–84 (2022).

26. Fearing, B. V., Hernandez, P. A., Setton, L. A. & Chahine, N. O. Mechanotransduction and cell biomechanics of the intervertebral disc. *JOR Spine* **1**, (2018).

27. Stokes, I. A. F. & Iatridis, J. C. Mechanical conditions that accelerate intervertebral disc degeneration: Overload versus immobilization. *Spine (Phila Pa 1976)* **29**, 2724–2732 (2004).

28. Sampson, S. L., Sylvia, M. & Fields, A. J. Effects of dynamic loading on solute transport through the human cartilage endplate. *J Biomech* **83**, 273–279 (2019).

29. Molladavoodi, S., McMorran, J. & Gregory, D. Mechanobiology of annulus fibrosus and nucleus pulposus cells in intervertebral discs. *Cell Tissue Res* **379**, 429–444 (2020).

30. Torre, O. M., Mroz, V., Bartelstein, M. K., Huang, A. H. & Iatridis, J. C. Annulus fibrosus cell phenotypes in homeostasis and injury: implications for regenerative strategies. *Ann N Y Acad Sci* **1442**, 61–78 (2019).

31. Stein, D. *et al.* 3D virtual reconstruction and quantitative assessment of the human intervertebral disc's annulus fibrosus: a DTI tractography study. *Sci Rep* **11**, (2021).

32. Tavakoli, J., Elliott, D. M. & Costi, J. J. Structure and mechanical function of the inter-lamellar matrix of the annulus fibrosus in the disc. *J Orthop Res* **34**, 1307–1315 (2016).

33. Berg-Johansen, B., Fields, A. J., Liebenberg, E. C., Li, A. & Lotz, J. C. Structure-function relationships at the human spinal disc-vertebra interface. *Journal of Orthopaedic Research* **36**, 192–201 (2018).

34. Bron, J. L., Helder, M. N., Meisel, H. J., Van Royen, B. J. & Smit, T. H. Repair, regenerative and supportive therapies of the annulus fibrosus: achievements and challenges. *Eur Spine J* **18**, 301–313 (2009).

35. Nedresky, D., Reddy, V. & Singh, G. Anatomy, Back, Nucleus Pulposus. *StatPearls* (2023).

36. Kibble, M. J., Domingos, M., Hoyland, J. A. & Richardson, S. M. Importance of Matrix Cues on Intervertebral Disc Development, Degeneration, and Regeneration. *International Journal of Molecular Sciences 2022, Vol. 23, Page 6915* **23**, 6915 (2022).

37. Roughley, P. J., Melching, L. I., Heathfield, T. F., Pearce, R. H. & Mort, J. S. The structure and degradation of aggrecan in human intervertebral disc. *European Spine Journal* **15**, 326–332 (2006).

38. Agrawal, A. *et al.* Normoxic stabilization of HIF-1alpha drives glycolytic metabolism and regulates aggrecan gene expression in nucleus pulposus cells of the rat intervertebral disk. *Am J Physiol Cell Physiol* **293**, (2007).

39. Williams, S., Alkhatib, B. & Serra, R. Development of the axial skeleton and intervertebral disc. *Curr Top Dev Biol* **133**, 49–90 (2019).

40. 6 Biology, Mechanics, and Genetics of the Disk: State of the Art. *AOSpine Masters Series* (2017) doi:10.1055/B-0036-139142.

41. Dimaraki, A. *et al.* Bioprinting of a zonal-specific cell density scaffold: A biomimetic approach for cartilage tissue engineering. *Applied Sciences (Switzerland)* **11**, 7821 (2021).

42. Alkhatib, B., Ban, G. I., Williams, S. & Serra, R. IVD Development: Nucleus Pulposus Development and Sclerotome Specification. *Curr Mol Biol Rep* **4**, 132–141 (2018).

43. Salisbury, J. R. The pathology of the human notochord. *J Pathol* **171**, 253–255 (1993).

44. Mccann, M. R., Séguin, C. A., Dettman, R. W. & Wessels, A. Notochord Cells in Intervertebral Disc Development and Degeneration. *Journal of Developmental Biology 2016, Vol. 4, Page 3* **4**, 3 (2016).

45. Yamada, T., Placzek, M., Tanaka, H., Dodd, J. & Jessell, T. M. Control of Cell Pattern in the Developing Nervous System: Polarizing Activity of the Floor Plate and Notochord. *Cell* **64**, 635–647 (1991).

46. Fan, C. M. & Tessier-Lavigne, M. Patterning of mammalian somites by surface ectoderm and notochord: Evidence for sclerotome induction by a hedgehog homolog. *Cell* **79**, 1175–1186 (1994).

47. Loh, K. M. M. *et al.* Mapping the Pairwise Choices Leading from Pluripotency to Human Bone, Heart, and Other Mesoderm Cell Types. *Cell* **166**, 451–467 (2016).

48. Stockdale, F. E., Nikovits, W. & Christ, B. Molecular and cellular biology of avian somite development. *Dev Dyn* **219**, 304–321 (2000).

49. Capdevila, J., Tabin, C. & Johnson, R. L. Control of dorsoventral somite patterning by Wnt-1 and beta-catenin. *Dev Biol* **193**, 182–194 (1998).

50. Peters, H. *et al.* Pax1 and Pax9 synergistically regulate vertebral column development. *Development* **126**, 5399–5408 (1999).

51. Risbud, M. V., Schaer, T. P. & Shapiro, I. M. Toward an understanding of the role of notochordal cells in the adult intervertebral disc: from discord to accord. *Dev Dyn* **239**, 2141–2148 (2010).

52. Hemanta, D., Jiang, X. xing, Feng, Z. zhou, Chen, Z. xian & Cao, Y. wu. Etiology for Degenerative Disc Disease. *Chinese Medical Sciences Journal* **31**, 185–191 (2016).

53. Mayer, J. E. *et al.* Genetic polymorphisms associated with intervertebral disc degeneration. *Spine Journal* **13**, 299–317 (2013).

54. Adams, M. A., McMillan, D. W., Green, T. P. & Dolan, P. Sustained loading generates stress concentrations in lumbar intervertebral discs. *Spine (Phila Pa 1976)* **21**, 434–438 (1996).

55. Wuertz, K. *et al.* Influence of extracellular osmolarity and mechanical stimulation on gene expression of intervertebral disc cells. *Journal of Orthopaedic Research* **25**, 1513–1522 (2007).

56. Dudli, S., Fields, A. J., Samartzis, D., Karppinen, J. & Lotz, J. C. Pathobiology of Modic changes. *Eur Spine J* **25**, 3723–3734 (2016).

57. Buckwalter, J. A. Spine update: Aging and degeneration of the human intervertebral disc. *Spine (Phila Pa 1976)* **20**, 1307–1314 (1995).

58. Vergroesen, P. P. A. *et al.* Mechanics and biology in intervertebral disc degeneration: A vicious circle. *Osteoarthritis Cartilage* **23**, 1057–1070 (2015).

59. Knudson, C. B. & Knudson, W. Cartilage proteoglycans. *Semin Cell Dev Biol* **12**, 69–78 (2001).

60. Crump, K. B. *et al.* Cartilaginous endplates: A comprehensive review on a neglected structure in intervertebral disc research. *JOR Spine* **6**, e1294 (2023).

61. Nachemson, A., Lewin, T., Maroudas, A. & Freeman, M. A. R. In vitro diffusion of DYE through the end-plates and the annulus fibrosus of human lumbar inter-vertebral discs. *Acta Orthop* **41**, 589–607 (1970).

62. Le Maitre, C. L., Hoyland, J. A. & Freemont, A. J. Open Access Catabolic cytokine expression in degenerate and herniated human intervertebral discs: IL-1β and TNFα expression profile. (2007) doi:10.1186/ar2275.

63. Le Maitre, C. L., Freemont, A. J. & Hoyland, J. A. The role of interleukin-1 in the pathogenesis of human intervertebral disc degeneration. *Arthritis Res Ther* **7**, (2005).

64. Purmessur, D. *et al.* A role for TNFα in intervertebral disc degeneration: A non-recoverable catabolic shift. *Biochem Biophys Res Commun* **433**, 151–156 (2013).

65. Makarand V. Risbud, Irving. M Shapiro (Department of Orthopedic Surgery, and Graduate Program in Cell and Developmental Biology, Jefferson Medical College, Philadelphia, P. Role of Cytokines in Intervertebral Disc Degeneration: Pain and Disc-content Disc-content. *NIH Public Access* **10**, 44–56 (2015).

66. Hoyland, J. A., Le Maitre, C. & Freemont, A. J. Investigation of the role of IL-1 and TNF in matrix degradation in the intervertebral disc. *Rheumatology* **47**, 809–814 (2008).

67. Andrade, P. *et al.* Elevated levels of tumor necrosis factor-α and TNFR1 in recurrent herniated lumbar discs correlate with chronicity of postoperative sciatic pain. *Spine Journal* **16**, 243–251 (2016).

68. Andrade, P. *et al.* Elevated IL-1β and IL-6 levels in lumbar herniated discs in patients with sciatic pain. *Eur Spine J* **22**, 714–720 (2013).

69. Studer, R. K., Vo, N., Sowa, G., Ondeck, C. & Kang, J. Human nucleus pulposus cells react to IL-6: independent actions and amplification of response to IL-1 and TNF-α. *Spine (Phila Pa 1976)* **36**, 593–599 (2011).

70. Wei, X. H. *et al.* The up-regulation of IL-6 in DRG and spinal dorsal horn contributes to neuropathic pain following L5 ventral root transection. *Exp Neurol* **241**, 159–168 (2013).

71. Murata, Y., Nannmark, U., Rydevik, B., Takahashi, K. & Olmarker, K. The role of tumor necrosis factor-alpha in apoptosis of dorsal root ganglion cells induced by herniated nucleus pulposus in rats. *Spine (Phila Pa 1976)* **33**, 155–162 (2008).

72. Baumgartner, L. *et al. Multiscale Regulation of the Intervertebral Disc: Achievements in Experimental, in Silico, and Regenerative Research*. *International Journal of Molecular Sciences* vol. 22 1–42 (MDPI AG, 2021).

73. Le Maitre, C. L., Pockert, A., Buttle, D. J., Freemont, A. J. & Hoyland, J. A. Matrix synthesis and degradation in human intervertebral disc degeneration. *Biochem Soc Trans* **35**, 652–655 (2007).

74. LA Binch, A. *et al.* Expression and regulation of neurotrophic and angiogenic factors during human intervertebral disc degeneration. *Arthritis Res Ther* **16**, (2014).

75. Kepler, C. K. *et al.* Substance p stimulates production of inflammatory cytokines in human disc cells. *Spine (Phila Pa 1976)* **38**, (2013).

76. Krock, E. *et al.* Painful, degenerating intervertebral discs up-regulate neurite sprouting and CGRP through nociceptive factors. *J Cell Mol Med* **18**, 1213–1225 (2014).

77. Lama, P., Le Maitre, C. L., Harding, I. J., Dolan, P. & Adams, M. A. Nerves and blood vessels in degenerated intervertebral discs are confined to physically disrupted tissue. *J Anat* **233**, 86–97 (2018).

78. Phillips, K., Cullen, K., Chiverton, N., … A. M.-O. and & 2015, undefined. Potential roles of cytokines and chemokines in human intervertebral disc degeneration: interleukin-1 is a master regulator of catabolic processes. *Elsevier*.

79. Farshad-Amacker, N. A., Hughes, A., Herzog, R. J., Seifert, B. & Farshad, M. The intervertebral disc, the endplates and the vertebral bone marrow as a unit in the process of degeneration. *Eur Radiol* **27**, 2507–2520 (2017).

80. Modic, M. T., Steinberg, P. M., Ross, J. S., Masaryk, T. J. & Carter, J. R. Degenerative disk disease: assessment of changes in vertebral body marrow with MR imaging. *Radiology* **166**, 193–199 (1988).

81. Dudli, S. *et al.* CD90-positive stromal cells associate with inflammatory and fibrotic changes in modic changes. *Osteoarthr Cartil Open* **4**, 100287 (2022).

82. Perilli, E. *et al.* Modic (endplate) changes in the lumbar spine: bone micro-architecture and remodelling. *Eur Spine J* **24**, 1926–1934 (2015).

83. Wang, Y., Videman, T. & Battié, M. C. Modic changes: prevalence, distribution patterns, and association with age in white men. *Spine J* **12**, 411–416 (2012).

84. Jensen, T. S. *et al.* Characteristics and natural course of vertebral endplate signal (Modic) changes in the Danish general population. *BMC Musculoskelet Disord* **10**, 1–9 (2009).

85. Kuisma, M. *et al.* Modic changes in vertebral endplates: A comparison of MR imaging and multislice CT. *Skeletal Radiol* **38**, 141–147 (2009).

86. Kjaer, P., Korsholm, L., Bendix, T., Sorensen, J. S. & Leboeuf-Yde, C. Modic changes and their associations with clinical findings. *European Spine Journal* **15**, 1312–1319 (2006).

87. De Roos, A., Kressel, H., Spritzer, C. & Dalinka, M. MR imaging of marrow changes adjacent to end plates in degenerative lumbar disk disease. *AJR Am J Roentgenol* **149**, 531–534 (1987).

88. Jensen, T. S. *et al.* Characteristics and natural course of vertebral endplate signal (Modic) changes in the Danish general population. *BMC Musculoskelet Disord* **10**, (2009).

89. Karchevsky, M. *et al.* Reactive endplate marrow changes: a systematic morphologic and epidemiologic evaluation. *Skeletal Radiol* **34**, 125–129 (2005).

90. Jensen, T. S., Karppinen, J., Sorensen, J. S., Niinimäki, J. & Leboeuf-Yde, C. Vertebral endplate signal changes (Modic change): a systematic literature review of prevalence and association with non-specific low back pain. *Eur Spine J* **17**, 1407–1422 (2008).

91. Määttä, J. H., Wadge, S., MacGregor, A., Karppinen, J. & Williams, F. M. K. ISSLS Prize Winner: Vertebral Endplate (Modic) Change is an Independent Risk Factor for Episodes of Severe and Disabling Low Back Pain. *Spine (Phila Pa 1976)* **40**, 1187–1193 (2015).

92. Määttä, J. H. *et al.* Strong association between vertebral endplate defect and Modic change in the general population. *Scientific Reports 2018 8:1* **8**, 1–8 (2018).

93. Takahashi, K., Miyazaki, T., Ohnari, H., Takino, T. & Tomita, K. Schmorl's nodes and low-back pain. Analysis of magnetic resonance imaging findings in symptomatic and asymptomatic individuals. *Eur Spine J* **4**, 56–59 (1995).

94. Albert, H. B. *et al.* Modic changes, possible causes and relation to low back pain. *Med Hypotheses* **70**, 361–368 (2008).

95. Kaneyama, S. *et al.* Fas ligand expression on human nucleus pulposus cells decreases with disc degeneration processes. *J Orthop Sci* **13**, 130–135 (2008).

96. Geiss, A., Larsson, K., Junevik, K., Rydevik, B. & Olmarker, K. Autologous nucleus pulposus primes T cells to develop into interleukin-4-producing effector cells: an experimental study on the autoimmune properties of nucleus pulposus. *J Orthop Res* **27**, 97–103 (2009).

97. Virri, J. *et al.* Comparison of the prevalence of inflammatory cells in subtypes of disc herniations and associations with straight leg raising. *Spine (Phila Pa 1976)* **26**, 2311–2315 (2001).

98. Shamji, M. F. *et al.* Gait abnormalities and inflammatory cytokines in an autologous nucleus pulposus model of radiculopathy. *Spine (Phila Pa 1976)* **34**, 648–654 (2009).

99. Park, J. B., Chang, H. & Kim, Y. S. The pattern of interleukin-12 and T-helper types 1 and 2 cytokine expression in herniated lumbar disc tissue. *Spine (Phila Pa 1976)* **27**, 2125–2128 (2002).

100. The stimulation of lymphocytes by nucleus pulposus in patients with degenerative disk disease of the lumbar spine - PubMed. https://pubmed.ncbi.nlm.nih.gov/852173/.

101. MOORE, W. E. & CATO, E. P. VALIDITY OF PROPIONIBACTERIUM ACNES (GILCHRIST) DOUGLAS AND GUNTER COMB. NOV. *J Bacteriol* **85**, 870 (1963).

102. Stirling, A., Worthington, T., Rafiq, M., Lambert, P. A. & Elliott, T. S. J. Association between sciatica and Propionibacterium acnes. *Lancet* **357**, 2024–2025 (2001).

103. Transient bacteremia induced by toothbrushing a comparison of the Sonicare toothbrush with a conventional toothbrush - PubMed. https://pubmed.ncbi.nlm.nih.gov/12212870/.

104. Malandrino, A., Noailly, J. & Lacroix, D. The Effect of Sustained Compression on Oxygen Metabolic Transport in the Intervertebral Disc Decreases with Degenerative Changes. *PLoS Comput Biol* **7**, e1002112 (2011).

105. Heggli, I. *et al.* Low back pain patients with Modic type 1 changes exhibit distinct bacterial and non-bacterial subtypes. *Osteoarthr Cartil Open* **6**, (2024).

106. Johnson, W. E. B. *et al.* Human intervertebral disc aggrecan inhibits nerve growth in vitro. *Arthritis Rheum* **46**, 2658–2664 (2002).

107. Johnson, W. E. B., Caterson, B., Eisenstein, S. M. & Roberts, S. Human intervertebral disc aggrecan inhibits endothelial cell adhesion and cell migration in vitro. *Spine (Phila Pa 1976)* **30**, 1139–1147 (2005).

108. Binch, A. L. A. *et al.* Class 3 semaphorins expression and association with innervation and angiogenesis within the degenerate human intervertebral disc. *Oncotarget* **6**, 18338–18354 (2015).

109. Tolofari, S. K., Richardson, S. M., Freemont, A. J. & Hoyland, J. A. Expression of semaphorin 3A and its receptors in the human intervertebral disc: potential role in regulating neural ingrowth in the degenerate intervertebral disc. *Arthritis Res Ther* **12**, (2010).

110. Sun, Z., Liu, B. & Luo, Z. J. The Immune Privilege of the Intervertebral Disc: Implications for Intervertebral Disc Degeneration Treatment. *Int J Med Sci* **17**, 685–692 (2020).

111. Jones, A. C. & Wilcox, R. K. Finite element analysis of the spine: towards a framework of verification, validation and sensitivity analysis. *Med Eng Phys* **30**, 1287–1304 (2008).

112. Phillips, K. L. E. *et al.* The cytokine and chemokine expression profile of nucleus pulposus cells: implications for degeneration and regeneration of the intervertebral disc. *Arthritis Res Ther* **15**, (2013).

113. Phillips, K. L. E. *et al.* Potential roles of cytokines and chemokines in human intervertebral disc degeneration: Interleukin-1 is a master regulator of catabolic processes. *Osteoarthritis Cartilage* **23**, 1165–1177 (2015).

114. Weiler, C., Nerlich, A. G., Bachmeier, B. E. & Boos, N. Expression and distribution of tumor necrosis factor alpha in human lumbar intervertebral discs: a study in surgical specimen and autopsy controls. *Spine (Phila Pa 1976)* **30**, 44–53 (2005).

115. Ye, F., Lyu, F. J., Wang, H. & Zheng, Z. The involvement of immune system in intervertebral disc herniation and degeneration. *JOR Spine* **5**, (2022).

116. Daniels, J., Binch, A. A. L. & Le Maitre, C. L. Inhibiting IL-1 signaling pathways to inhibit catabolic processes in disc degeneration. *Journal of Orthopaedic Research* **35**, 74–85 (2017).

117. Suyama, K. *et al.* Effects of interleukin-17A in nucleus pulposus cells and its small-molecule inhibitors for intervertebral disc disease. *J Cell Mol Med* **22**, 5539–5551 (2018).

118. Baumgartner, L. *et al.* Multiscale Regulation of the Intervertebral Disc: Achievements in Experimental, In Silico, and Regenerative Research. *Int J Mol Sci* **22**, 1–42 (2021).

119. Lee, J. M. *et al.* Interleukin-1β induces angiogenesis and innervation in human intervertebral disc degeneration. *Journal of Orthopaedic Research* **29**, 265–269 (2011).

120. Gorth, D. J., Shapiro, I. M. & Risbud, M. V. A New Understanding of the Role of IL-1 in Age-Related Intervertebral Disc Degeneration in a Murine Model. *Journal of Bone and Mineral Research* **34**, 1531–1542 (2019).

121. Fadok, V. A. Clearance: The Last and Often Forgotten Stage of Apoptosis. *J Mammary Gland Biol Neoplasia* **4**, 203–211 (1999).

122. Pattappa, G. *et al.* CCL5/RANTES is a key chemoattractant released by degenerative intervertebral discs in organ culture. *Eur Cell Mater* **27**, 124–136 (2014).

123. Leung, L. & Cahill, C. M. TNF-alpha and neuropathic pain--a review. *J Neuroinflammation* **7**, (2010).

124. Leung, L. & Cahill, C. M. TNF-α and neuropathic pain - a review. *J Neuroinflammation* **7**, 1–11 (2010).

125. Albert, H. B. *et al.* Does nuclear tissue infected with bacteria following disc herniations lead to Modic changes in the adjacent vertebrae? *Eur Spine J* **22**, 690–696 (2013).

126. Capoor, M. N. *et al.* Prevalence of propionibacterium acnes in intervertebral discs of patients undergoing lumbar microdiscectomy: A prospective cross-sectional study. *PLoS One* **11**, (2016).

127. Capoor, M. N. *et al.* Propionibacterium acnes biofilm is present in intervertebral discs of patients undergoing microdiscectomy. *PLoS One* **12**, (2017).

128. Dudli, S. *et al.* Propionibacterium acnes infected intervertebral discs cause vertebral bone marrow lesions consistent with Modic changes. *J Orthop Res* **34**, 1447–1455 (2016).

129. Heggli, I. *et al.* Low back pain patients with Modic type 1 changes exhibit distinct bacterial and non-bacterial subtypes. *Osteoarthr Cartil Open* **6**, (2024).

130. Manniche, C. & O'Neill, S. New insights link low-virulent disc infections to the etiology of severe disc degeneration and Modic changes. *Future Sci OA* **5**, (2019).

131. Tang, G. *et al.* Latent infection of low-virulence anaerobic bacteria in degenerated lumbar intervertebral discs. *BMC Musculoskelet Disord* **19**, (2018).

132. Rajasekaran, S. *et al.* ISSLS PRIZE IN CLINICAL SCIENCE 2017: Is infection the possible initiator of disc disease? An insight from proteomic analysis. *European Spine Journal* **26**, 1384–1400 (2017).

133. Singh, S. *et al.* Correlation Between Modic Changes and Bacterial Infection: A Causative Study. *Int J Spine Surg* **14**, 832–837 (2020).

134. Fritzell, P. *et al.* Bacteria: back pain, leg pain and Modic sign—a surgical multicentre comparative study. *European Spine Journal* **28**, 2981–2989 (2019).

135. Mayslich, C., Grange, P. A. & Dupin, N. Cutibacterium acnes as an Opportunistic Pathogen: An Update of Its Virulence-Associated Factors. *Microorganisms* **9**, 1–21 (2021).

136. Shanmuganathan, R. *et al.* Comparative metagenomic analysis of human intervertebral disc nucleus pulposus and cartilaginous end plates. *Front Cardiovasc Med* **9**, 927652 (2022).

137. Rajasekaran, S. *et al.* 'Are we barking up the wrong tree? Too much emphasis on Cutibacterium acnes and ignoring other pathogens'- a study based on next-generation sequencing of normal and diseased discs. *Spine J* **23**, 1414–1426 (2023).

138. Mengis, T. *et al.* Intervertebral disc microbiome in Modic changes: Lack of result replication underscores the need for a consensus in low-biomass microbiome analysis. *JOR Spine* **7**, e1330 (2024).

139. Albert, H. B., Sorensen, J. S., Christensen, B. S. & Manniche, C. Antibiotic treatment in patients with chronic low back pain and vertebral bone edema (Modic type 1 changes): A double-blind randomized clinical controlled trial of efficacy. *European Spine Journal* **22**, 697–707 (2013).

140. Bråten, L. C. H. *et al.* Efficacy of antibiotic treatment in patients with chronic low back pain and Modic changes (the AIM study): double blind, randomised, placebo controlled, multicentre trial. *BMJ* **367**, (2019).

141. Bråten, L. C. H. *et al.* Efficacy of antibiotic treatment in patients with chronic low back pain and Modic changes (the AIM study): double blind, randomised, placebo controlled, multicentre trial. *The BMJ* **367**, l5654 (2019).

142. Palazzo, C. *et al.* Lack of effectiveness of antibiotics in chronic low back pain with Modic 1 changes. *Joint Bone Spine* **84**, 507–508 (2017).

143. Lin, Y. *et al.* Propionibacterium acnes Induces Intervertebral Disc Degeneration by Promoting iNOS/NO and COX-2/PGE2 Activation via the ROS-Dependent NF- κ B Pathway. *Oxid Med Cell Longev* **2018**, (2018).

144. Zamora, T. *et al.* Effect of Propionibacterium acnes (PA) injection on intervertebral disc degeneration in a rat model: Does it mimic modic changes? *Orthopaedics & Traumatology: Surgery & Research* **103**, 795–799 (2017).

145. Chen, Z. *et al.* Modic Changes and Disc Degeneration Caused by Inoculation of Propionibacterium acnes inside Intervertebral Discs of Rabbits: A Pilot Study. *Biomed Res Int* **2016**, (2016).

146. Shan, Z. *et al.* Propionibacterium acnes Incubation in the Discs Can Result in Time-Dependent Modic Changes: A Long-Term Rabbit Model. *Spine (Phila Pa 1976)* **42**, 1595–1603 (2017).

147. Rajasekaran, S. *et al.* Human intervertebral discs harbour a unique microbiome and dysbiosis determines health and disease. *European Spine Journal* **29**, 1621–1640 (2020).

148. Gajewski, T. F., Schreiber, H. & Fu, Y. X. Innate and adaptive immune cells in the tumor microenvironment. *Nat Immunol* **14**, 1014 (2013).

149. Akira, S., Uematsu, S. & Takeuchi, O. Pathogen recognition and innate immunity. *Cell* **124**, 783–801 (2006).

150. Mengis, T. *et al.* The Expression of Toll-like Receptors in Cartilage Endplate Cells: A Role of Toll-like Receptor 2 in Pro-Inflammatory and Pro-Catabolic Gene Expression. *Cells* **13**, (2024).

151. Klawitter, M. *et al.* Expression and regulation of toll-like receptors (TLRs) in human intervertebral disc cells. *Eur Spine J* **23**, 1878–1891 (2014).

152. Pulendran, B. & Ahmed, R. From Innate Immunity to Immunological Memory. **311**, (2006).

153. Jacobsen, T. D., Hernandez, P. A. & Chahine, N. O. INHIBITION OF TOLL-LIKE RECEPTOR 4 PROTECTS AGAINST INFLAMMATION-INDUCED MECHANOBIOLOGICAL ALTERATIONS TO INTERVERTEBRAL DISC CELLS. *Eur Cell Mater* **41**, 576 (2021).

154. Midwood, K. *et al.* Tenascin-C is an endogenous activator of Toll-like receptor 4 that is essential for maintaining inflammation in arthritic joint disease. *Nat Med* **15**, 774–780 (2009).

155. Schaefer, L. *et al.* The matrix component biglycan is proinflammatory and signals through Toll-like receptors 4 and 2 in macrophages. *J Clin Invest* **115**, 2223–2233 (2005).

156. Steidl, C. *et al.* MHC class II transactivator CIITA is a recurrent gene fusion partner in lymphoid cancers. *Nature 2011 471:7338* **471**, 377–381 (2011).

157. Steiner, A. *et al.* Recessive NLRC4-Autoinflammatory Disease Reveals an Ulcerative Colitis Locus. *J Clin Immunol* **42**, 325–335 (2022).

158. Swanberg, M. *et al.* MHC2TA is associated with differential MHC molecule expression and susceptibility to rheumatoid arthritis, multiple sclerosis and myocardial infarction. *Nature Genetics 2005 37:5* **37**, 486–494 (2005).

159. McGovern, D. P. B. *et al.* Association between a complex insertion/deletion polymorphism in NOD1 (CARD4) and susceptibility to inflammatory bowel disease. *Hum Mol Genet* **14**, 1245–1250 (2005).

160. Berrington, W. R. *et al.* Common Polymorphisms in the NOD2 Gene Region Are Associated with Leprosy and Its Reactive States. *J Infect Dis* **201**, 1422–1435 (2010).

161. Inohara, N. *et al.* Host recognition of bacterial muramyl dipeptide mediated through NOD2. Implications for Crohn's disease. *J Biol Chem* **278**, 5509–5512 (2003).

162. Girardin, S. E. *et al.* Nod2 is a general sensor of peptidoglycan through muramyl dipeptide (MDP) detection. *J Biol Chem* **278**, 8869–8872 (2003).

163. Girardin, S. E. *et al.* Nod1 detects a unique muropeptide from gram-negative bacterial peptidoglycan. *Science* **300**, 1584–1587 (2003).

164. Chamaillard, M. *et al.* An essential role for NOD1 in host recognition of bacterial peptidoglycan containing diaminopimelic acid. *Nature Immunology 2003 4:7* **4**, 702–707 (2003).

165. Elinav, E., Strowig, T., Henao-Mejia, J. & Flavell, R. A. Regulation of the antimicrobial response by NLR proteins. *Immunity* **34**, 665–679 (2011).

166. Franchi, L., Eigenbrod, T., Muñoz-Planillo, R. & Nuñez, G. The inflammasome: a caspase-1-activation platform that regulates immune responses and disease pathogenesis. *Nat Immunol* **10**, 241–247 (2009).

167. Lamkanfi, M., Walle, L. Vande & Kanneganti, T. D. Deregulated inflammasome signaling in disease. *Immunol Rev* **243**, 163–173 (2011).

168. Tang, G. *et al.* Propionibacterium acnes Accelerates Intervertebral Disc Degeneration by Inducing Pyroptosis of Nucleus Pulposus Cells via the ROS-NLRP3 Pathway. *Oxid Med Cell Longev* **2021**, (2021).

169. Chao-yang, G., Peng, C. & Hai-hong, Z. Roles of NLRP3 inflammasome in intervertebral disc degeneration. *Osteoarthritis Cartilage* **29**, 793–801 (2021).

170. Mnich, M. E., van Dalen, R. & van Sorge, N. M. C-Type Lectin Receptors in Host Defense Against Bacterial Pathogens. *Front Cell Infect Microbiol* **10**, (2020).

171. Loo, Y. M. & Gale, M. Immune signaling by RIG-I-like receptors. *Immunity* **34**, 680–692 (2011).

172. Nakaya, Y., Lilue, J., Stavrou, S., Moran, E. A. & Ross, S. R. AIM2-like receptors positively and negatively regulate the interferon response induced by cytosolic DNA. *mBio* **8**, (2017).

173. True, L. D. Quality control in molecular immunohistochemistry. *Histochem Cell Biol* **130**, 473–480 (2008).

174. Binch, A., Snuggs, J. & Le Maitre, C. L. Immunohistochemical analysis of protein expression in formalin fixed paraffin embedded human intervertebral disc tissues. *JOR Spine* **3**, (2020).

175. Loughrey, M. B. *et al.* Validation of the systematic scoring of immunohistochemically stained tumour tissue microarrays using QuPath digital image analysis. *Histopathology* **73**, 327–338 (2018).

176. Di Cataldo, S., Ficarra, E., Acquaviva, A. & Macii, E. Automated segmentation of tissue images for computerized IHC analysis. *Comput Methods Programs Biomed* **100**, 1–15 (2010).

177. Bankhead, P. *et al.* QuPath: Open source software for digital pathology image analysis. *Sci Rep* **7**, (2017).

178. Choudhury, K. R., Yagle, K. J., Swanson, P. E., Krohn, K. A. & Rajendran, J. G. A robust automated measure of average antibody staining in immunohistochemistry images. *J Histochem Cytochem* **58**, 95–107 (2010).

179. Thorpe, C. T. & Screen, H. R. C. Tendon Structure and Composition. *Adv Exp Med Biol* **920**, 3–10 (2016).

180. Biewener, A. A. Tendons and Ligaments: Structure, Mechanical Behavior and Biological Function. *Collagen: Structure and Mechanics* 269–284 (2008) doi:10.1007/978-0-387-73906-9_10.

181. Sophia Fox, A. J., Bedi, A. & Rodeo, S. A. The basic science of articular cartilage: Structure, composition, and function. *Sports Health* **1**, 461–468 (2009).

182. Whatley, B. R. & Wen, X. Intervertebral disc (IVD): Structure, degeneration, repair and regeneration. *Materials Science and Engineering: C* **32**, 61–77 (2012).

183. Ferri, M. P. Processing Scanning Data. *https://mapoferri/processscanningdata* (2024).

184. Nüesch, A. & Ferri, M. P. QuPath Guide for Semi-Automatic Quantification of Immunohistochemically stained Slides- Processing Package Tutorial Gitbook. *https://disc4all-qupath.gitbook.io/qupath-project/result-analysis-docs/processing-package-tutorial* (2024).

185. Taylor, C. R. & Levenson, R. M. Quantification of immunohistochemistry—issues concerning methods, utility and semiquantitative assessment II. *Histopathology* **49**, 411–424 (2006).

186. Nüesch, A. & Ferri, M. P. QuPath Guide for Semi-Automatic Quantification of Immunohistochemically stained Slides. *https://disc4all-qupath.gitbook.io/qupath-project* (2024).

187. Nüesch, A. & Ferri, M. P. QuPath Guide for Semi-Automatic Quantification of Immunohistochemically stained Slides- Estimating Staining Vectors. *https://app.gitbook.com/o/kAkxf5RLoV6dm2APAW3P/s/SleK316zl0BYwa7DfK2J/qupath-h-dab-docs/qupath-h-dab-tutorial/estimating-stain-vectors* (2024).

188. Bankhead, P. *et al.* QuPath: Open source software for digital pathology image analysis. *Sci Rep* **7**, (2017).

189. Nüesch, A. & Ferri, M. P. QuPath Guide for Semi-Automatic Quantification of Immunohistochemically stained Slides- Training Image Creation. *https://app.gitbook.com/o/kAkxf5RLoV6dm2APAW3P/s/SleK316zl0BYwa7DfK2J/qupath-h-dab-docs/qupath-h-dab-tutorial/training-image-creation* (2024).

190. Nüesch, A. & Ferri, M. P. QuPath Guide for Semi-Automatic Quantification of Immunohistochemically stained Slides- Cell Detection. *https://disc4all-*

qupath.gitbook.io/qupath-project/qupath-h-dab-docs/qupath-h-dab-tutorial/cell-detection (2024).

191. Nüesch, A. & Ferri, M. P. QuPath Guide for Semi-Automatic Quantification of Immunohistochemically stained Slides- Object Classifier. *https://app.gitbook.com/o/kAkxf5RLoV6dm2APAW3P/s/SleK316zl0BYwa7DfK2J/qupath-h-dab-docs/qupath-h-dab-tutorial/object-classifier* (2024).

192. Nüesch, A. & Ferri, M. P. QuPath Guide for Semi-Automatic Quantification of Immunohistochemically stained Slides- Tissue Detection. *https://app.gitbook.com/o/kAkxf5RLoV6dm2APAW3P/s/SleK316zl0BYwa7DfK2J/qupath-h-dab-docs/qupath-h-dab-tutorial/tissue-detection* (2024) doi:https://app.gitbook.com/o/kAkxf5RLoV6dm2APAW3P/s/SleK316zl0BYwa7DfK2J/qupath-h-dab-docs/qupath-h-dab-tutorial/tissue-detection.

193. Nüesch, A. H-DAB Batch Analysis Script. *https://github.com/anuesch/Disc4All_QuPath_H-DAB_Script* (2024).

194. Nüesch, A. & Ferri, M. P. QuPath Guide for Semi-Automatic Quantification of Immunohistochemically stained Slides- Batch Analysis Script. *https://app.gitbook.com/o/kAkxf5RLoV6dm2APAW3P/s/SleK316zl0BYwa7DfK2J/qupath-h-dab-docs/qupath-script*.

195. Harris, C. R. *et al.* Array programming with NumPy. *Nature 2020 585:7825* **585**, 357–362 (2020).

196. McKinney, W. Data Structures for Statistical Computing in Python. *Proceedings of the 9th Python in Science Conference* 56–61 (2010) doi:10.25080/MAJORA-92BF1922-00A.

197. Hunter, J. D. Matplotlib: A 2D graphics environment. *Comput Sci Eng* **9**, 90–95 (2007).

198. Pearson, K. VII. Note on regression and inheritance in the case of two parents. *Proceedings of the Royal Society of London* **58**, 240–242 (1895).

199. Spearman, C. The Proof and Measurement of Association between Two Things. *Am J Psychol* **15**, 72 (1904).

200. Kendall, M. G. A New Measure of Rank Correlation. *Biometrika* **30**, 81 (1938).

201. De Gramont, A. *et al.* Pragmatic issues in biomarker evaluation for targeted therapies in cancer. *Nat Rev Clin Oncol* **12**, 197–212 (2015).

202. Aeffner, F. *et al.* The Gold Standard Paradox in Digital Image Analysis: Manual Versus Automated Scoring as Ground Truth. *Arch Pathol Lab Med* **141**, 1267–1275 (2017).

203. Hein, A. L. *et al.* QuPath Digital Immunohistochemical Analysis of Placental Tissue. *J Pathol Inform* **12**, 40 (2021).

204. Bankhead, P. Developing image analysis methods for digital pathology. *J Pathol* **257**, 391–402 (2022).

205. Koo, T. K. & Li, M. Y. A Guideline of Selecting and Reporting Intraclass Correlation Coefficients for Reliability Research. *J Chiropr Med* **15**, 155–163 (2016).

206. Mirzaeipoueinak, M. *et al.* Structure-function characterization of the transition zone in the intervertebral disc. *Acta Biomater* **160**, 164–175 (2023).

207. Ferreira, M. L. *et al.* Global, regional, and national burden of low back pain, 1990-2020, its attributable risk factors, and projections to 2050: a systematic analysis of the Global Burden of Disease Study 2021. *Lancet Rheumatol* **5**, e316–e329 (2023).

208. Stirling, A., Worthington, T., Rafiq, M., Lambert, P. A. & Elliott, T. S. J. Association between sciatica and Propionibacterium acnes. *Lancet* **357**, 2024–2025 (2001).

209. Agarwal, V., Golish, S. R. & Alamin, T. F. Bacteriologic culture of excised intervertebral disc from immunocompetent patients undergoing single level primary lumbar microdiscectomy. *J Spinal Disord Tech* **24**, 397–400 (2011).

210. Aghazadeh, J. *et al.* Modic changes in the adjacent vertebrae due to disc material infection with Propionibacterium acnes in patients with lumbar disc herniation. *European Spine Journal* **26**, 3129–3134 (2017).

211. Arndt, J., Charles, Y. P., Koebel, C., Bogorin, I. & Steib, J. P. Bacteriology of degenerated lumbar intervertebral disks. *J Spinal Disord Tech* **25**, (2012).

212. Bivona, L. J. *et al.* The Prevalence of Bacterial Infection in Patients Undergoing Elective ACDF for Degenerative Cervical Spine Conditions: A Prospective Cohort Study With Contaminant Control. *Global Spine J* **11**, 13–20 (2021).

213. Chen, Y. *et al.* Low virulence bacterial infections in cervical intervertebral discs: a prospective case series. *European Spine Journal* **27**, 2496–2505 (2018).

214. Coscia, M. F., Denys, G. A. & Wack, M. F. Propionibacterium acnes, coagulase-negative staphylococcus, and the '"biofilm-like"' intervertebral disc. *Spine (Phila Pa 1976)* **41**, 1860–1865 (2016).

215. Drago, L. *et al.* Are Modic type 2 disc changes associated with low-grade infections? A pilot study. *J Neurosurg Sci* **64**, 243–246 (2020).

216. Allhorn, M., Arve, S., Brüggemann, H. & Lood, R. A novel enzyme with antioxidant capacity produced by the ubiquitous skin colonizer Propionibacterium acnes. *Sci Rep* **6**, (2016).

217. Christensen, G. J. M. & Brüggemann, H. Bacterial skin commensals and their role as host guardians. *Benef Microbes* **5**, 201–215 (2014).

218. Achermann, Y., Goldstein, E. J. C., Coenye, T. & Shirtliffa, M. E. Propionibacterium acnes: from commensal to opportunistic biofilm-associated implant pathogen. *Clin Microbiol Rev* **27**, 419–440 (2014).

219. Aubin, G. G., Portillo, M. E., Trampuz, A. & Corvec, S. Propionibacterium acnes, an emerging pathogen: From acne to implant-infections, from phylotype to resistance. *Med Mal Infect* **44**, 241–250 (2014).

220. Jevons, M. P., Coe, A. W. & Parker, M. T. Methicillin resistance in staphylococci. *Lancet* **1**, 904–907 (1963).

221. Rehwinkel, J. & Gack, M. U. RIG-I-like receptors: their regulation and roles in RNA sensing. *Nature Reviews Immunology 2020 20:9* **20**, 537–551 (2020).

222. Franchi, L., Warner, N., Viani, K. & Nuñez, G. Function of Nod-like receptors in microbial recognition and host defense. *Immunol Rev* **227**, 106–128 (2009).

223. Sameer, A. S. & Nissar, S. Toll-Like Receptors (TLRs): Structure, Functions, Signaling, and Role of Their Polymorphisms in Colorectal Cancer Susceptibility. *Biomed Res Int* **2021**, (2021).

224. Mengis, T. *et al.* The Expression of Toll-like Receptors in Cartilage Endplate Cells: A Role of Toll-like Receptor 2 in Pro-Inflammatory and Pro-Catabolic Gene Expression. *Cells* **13**, (2024).

225. Schmid, B., Hausmann, O., Hitzl, W., Achermann, Y. & Wuertz-Kozak, K. The role of Cutibacterium acnes in intervertebral disc inflammation. *Biomedicines* **8**, (2020).

226. Bisson, D. G., Mannarino, M., Racine, R. & Haglund, L. For whom the disc tolls: Intervertebral disc degeneration, back pain and toll-like receptors. *Eur Cell Mater* **41**, 355–369 (2021).

227. Strober, W. & Watanabe, T. NOD2, an intracellular innate immune sensor involved in host defense and Crohn's disease. *Mucosal Immunol* **4**, 484–495 (2011).

228. Le Maitre, C. L. *et al.* Development of a standardized histopathology scoring system for human intervertebral disc degeneration: an Orthopaedic Research Society Spine Section Initiative. *JOR Spine* **4**, e1167–e1167 (2021).

229. Binch, A., Snuggs, J. & Le Maitre, C. L. Immunohistochemical analysis of protein expression in formalin fixed paraffin embedded human intervertebral disc tissues. **3**, (2020).

230. Basatvat, S. *et al.* Harmonization and standardization of nucleus pulposus cell extraction and culture methods. *JOR Spine* **6**, e1238 (2023).

231. Snuggs, J., Basatvat, S. & Le Maitre, C. Understanding the physiological behaviour of disc cells in an in vitro imitation of the healthy and degenerated disc niche. *In Preparation* (2024).

232. Poussin, C. *et al.* The species translation challenge—A systems biology perspective on human and rat bronchial epithelial cells. *Scientific Data 2014 1:1* **1**, 1–14 (2014).

233. Granville Smith, I. *et al.* Evidence for infection in intervertebral disc degeneration: a systematic review. *European Spine Journal* vol. 31 414–430 Preprint at https://doi.org/10.1007/s00586-021-07062-1 (2022).

234. Ahmed-Yahia, S. *et al.* Is the discopathy associated with Modic changes an infectious process? Results from a prospective monocenter study. *PLoS One* **14**, (2019).

235. Fritzell, P. *et al.* Bacteria: back pain, leg pain and Modic sign-a surgical multicentre comparative study. *Eur Spine J* **28**, 2981–2989 (2019).

236. Ohrt-Nissen, S. *et al.* Bacterial biofilms: a possible mechanism for chronic infection in patients with lumbar disc herniation – a prospective proof-of-concept study using fluorescence in situ hybridization. *APMIS* **126**, 440–447 (2018).

237. Jones, P., Gardner, L., Menage, J., Williams, G. T. & Roberts, S. Intervertebral disc cells as competent phagocytes in vitro: Implications for cell death in disc degeneration. *Arthritis Res Ther* **10**, (2008).

238. Nerlich, A. G., Weiler, C., Zipperer, J., Narozny, M. & Boos, N. Immunolocalization of phagocytic cells in normal and degenerated intervertebral discs. *Spine (Phila Pa 1976)* **27**, 2484–2490 (2002).

239. Antonio Simões Quaresma, J. *et al.* Microbicidal Phagocytosis of Nucleus Pulposus Cells Against Staphylococcus aureus via the TLR2/MAPKs Signaling Path. *Front Immunol* 1132 (2019) doi:10.3389/fimmu.2019.01132.

240. Capoor, M. N. *et al.* Pro-inflammatory and neurotrophic factor responses of cells derived from degenerative human intervertebral discs to the opportunistic pathogen cutibacterium acnes. *Int J Mol Sci* **22**, 1–16 (2021).

241. Ellman, M. B. *et al.* Toll-like receptor adaptor signaling molecule MyD88 on intervertebral disk homeostasis: In vitro, ex vivo studies. *Gene* **505**, 283–290 (2012).

242. Krock, E. *et al.* Toll-like Receptor Activation Induces Degeneration of Human Intervertebral Discs. *Sci Rep* **7**, 17184 (2017).

243. Caruso, R., Warner, N., Inohara, N. & Núñez, G. NOD1 and NOD2: signaling, host defense, and inflammatory disease. *Immunity* **41**, 898–908 (2014).

244. Proell, M., Riedl, S. J., Fritz, J. H., Rojas, A. M. & Schwarzenbacher, R. The Nod-Like Receptor (NLR) Family: A Tale of Similarities and Differences. *PLoS One* **3**, e2119 (2008).

245. Thakker, P. *et al.* XIAP promotes the expansion and limits the contraction of CD8 T cell response through cell extrinsic and intrinsic mechanisms respectively. *PLoS Pathog* **19**, (2023).

246. Yan, X. *et al.* Acrylamide induces the activation of BV2 microglial cells through TLR2/4-mediated LRRK2-NFATc2 signaling cascade. *Food and Chemical Toxicology* **176**, 113775 (2023).

247. Patterson, B. K. *et al.* Susceptibility to human immunodeficiency virus-1 infection of human foreskin and cervical tissue grown in explant culture. *Am J Pathol* **161**, 867–873 (2002).

248. van der Vlist, M. *et al.* Human Langerhans cells capture measles virus through Langerin and present viral antigens to CD4+ T cells but are incapable of cross-presentation. *Eur J Immunol* **41**, 2619–2631 (2011).

249. Raes, G. *et al.* Macrophage galactose-type C-type lectins as novel markers for alternatively activated macrophages elicited by parasitic infections and allergic airway inflammation. *J Leukoc Biol* **77**, 321–327 (2005).

250. Geijtenbeek, T. B. H. *et al.* Identification of DC-SIGN, a Novel Dendritic Cell–Specific ICAM-3 Receptor that Supports Primary Immune Responses. *Cell* **100**, 575–585 (2000).

251. Han, S. *et al.* Single-Cell RNA Sequencing of the Nucleus Pulposus Reveals Chondrocyte Differentiation and Regulation in Intervertebral Disc Degeneration. *Front Cell Dev Biol* **10**, 824771 (2022).

252. Lin, Y. *et al.* Propionibacterium acnes induces intervertebral disc degeneration by promoting nucleus pulposus cell apoptosis via the TLR2/JNK/mitochondrial-mediated pathway article. *Emerg Microbes Infect* **7**, (2018).

253. Paugam, C. *et al.* Propionibacterium acnes phylotypes and acne severity: an observational prospective study. *Journal of the European Academy of Dermatology and Venereology* **31**, e398–e399 (2017).

254. McDowell, A., Nagy, I., Magyari, M., Barnard, E. & Patrick, S. The Opportunistic Pathogen Propionibacterium acnes: Insights into Typing, Human Disease, Clonal Diversification and CAMP Factor Evolution. *PLoS One* **8**, e70897 (2013).

255. McDowell, A. *et al.* An Expanded Multilocus Sequence Typing Scheme for Propionibacterium acnes: Investigation of 'Pathogenic', 'Commensal' and Antibiotic Resistant Strains. *PLoS One* **7**, e41480 (2012).

256. Tomida, S. *et al.* Pan-genome and comparative genome analyses of Propionibacterium acnes reveal its genomic diversity in the healthy and diseased human skin microbiome. *mBio* **4**, (2013).

257. Lan, W., Wang, X., Tu, X., Hu, X. & Lu, H. Different phylotypes of Cutibacterium acnes cause different modic changes in intervertebral disc degeneration. *PLoS One* **17**, (2022).

258. Cheung, G. Y. C., Bae, J. S. & Otto, M. Pathogenicity and virulence of Staphylococcus aureus. *Virulence* **12**, 547–569 (2021).

259. Urquhart, D. M. *et al.* Could low grade bacterial infection contribute to low back pain? A systematic review. *BMC Med* **13**, (2015).

260. Fritzell, P. *et al. Detection of Bacterial DNA in Painful Degenerated Spinal Discs in Patients without Signs of Clinical Infection*. *Eur Spine J* vol. 13 https://link.springer.com/article/10.1007/s00586-004-0719-z (2004).

261. Coscia, E. C. *et al.* Sheep as a Potential Model of Intradiscal Infection by the Bacterium Cutibacterium acnes. *Vet Sci* **8**, (2021).

262. Chan, S. C. W. & Gantenbein-Ritter, B. Preparation of intact bovine tail intervertebral discs for organ culture. *Journal of Visualized Experiments* 1–7 (2012) doi:10.3791/3490.

263. Chan, S. C. W., Ferguson, S. J. & Gantenbein-Ritter, B. The effects of dynamic loading on the intervertebral disc. *Eur Spine J* **20**, 1796–1812 (2011).

264. Chan, S. C. W. & Gantenbein-Ritter, B. Preparation of intact bovine tail intervertebral discs for organ culture. *J Vis Exp* 1–7 (2012) doi:10.3791/3490.

265. Federal Food Safety and Veterinary Authority Verantwortlichkeiten in der Lebensmittelsicherheit.

266. Department for Environment, Food & Rural Affairs. Veterinary Medicines Guidance Notes (VMGNs): Using Medicines.

267. U.S. Food and Drug Administration. Guidance for Industry. https://www.fda.gov/animal-veterinary/guidance-regulations/guidance-industry.

268. Lyons, J. A. *et al.* Isolation of Propionibacterium acnes from a case of placentitis and abortion in a cow. *Journal of Veterinary Diagnostic Investigation* **21**, 274–277 (2009).

269. Campos, B. *et al.* Diversity and pathogenesis of Staphylococcus aureus from bovine mastitis: current understanding and future perspectives. *BMC Veterinary Research 2022 18:1* **18**, 1–16 (2022).

270. Gomes, F. & Henriques, M. Control of Bovine Mastitis: Old and Recent Therapeutic Approaches. *Curr Microbiol* **72**, 377–382 (2016).

271. Fagundes, H., Barchesi, L., Filho, A. N., Ferreira, L. M. & Oliveira, C. A. F. Occurrence of Staphylococcus aureus in raw milk produced in dairy farms in São Paulo state, Brazil. *Brazilian Journal of Microbiology* **41**, 376–380 (2010).

272. Lin, Y. *et al.* Propionibacterium acnes Induces Intervertebral Disc Degeneration by Promoting iNOS/NO and COX-2/PGE 2 Activation via the ROS-Dependent NF-κ B Pathway. *Oxid Med Cell Longev* **2018**, (2018).

273. Saxena, A. K., Kumar, M., Chakdar, H., Anuroopa, N. & Bagyaraj, D. J. Bacillus species in soil as a natural resource for plant health and nutrition. *J Appl Microbiol* **128**, 1583–1594 (2020).

274. Ganji, L. *et al.* Dysbiosis of fecal microbiota and high frequency of Citrobacter, Klebsiella spp., and Actinomycetes in patients with irritable bowel syndrome and gastroenteritis. *Gastroenterol Hepatol Bed Bench* **9**, 325 (2016).

275. Kus, J. V. Infections due to Citrobacter and Enterobacter☆. *Reference Module in Biomedical Sciences* (2014) doi:10.1016/B978-0-12-801238-3.05089-3.

276. Owoseni, A. A. *et al.* Presence of Antibiotic Resistance Genes in Bacteria Isolated from Raw Cow Milk obtained from Bowen University Dairy Farm. *IOP Conf Ser Earth Environ Sci* **1219**, 012004 (2023).

277. De Witte, C. *et al.* Presence of Broad-Spectrum Beta-Lactamase-Producing Enterobacteriaceae in Zoo Mammals. *Microorganisms* **9**, (2021).

278. Thomson, N. M. *et al.* Remarkable genomic diversity among Escherichia isolates recovered from healthy chickens. *PeerJ* **10**, e12935 (2022).

279. Ocejo, M., Tello, M., Oporto, B., Lavín, J. L. & Hurtado, A. Draft Genome Sequence of Escherichia marmotae E690, Isolated from Beef Cattle. *Microbiol Resour Announc* **9**, (2020).

280. Baldani, J. I. *et al.* Emended description of Herbaspirillum; inclusion of [Pseudomonas] rubrisubalbicans, a milk plant pathogen, as Herbaspirillum rubrisubalbicans comb. nov.; and classification of a group of clinical isolates (EF group 1) as Herbaspirillum species 3. *Int J Syst Bacteriol* **46**, 802–810 (1996).

281. Ding, L. & Yokota, A. Proposals of Curvibacter gracilis gen. nov., sp. nov. and Herbaspirillum putei sp. nov. for bacterial strains isolated from well water and reclassification of [Pseudomonas] huttiensis, [Pseudomonas] lanceolata, [Aquaspirillum] delicatum and [Aquaspirillum] autotrophicum as Herbaspirillum huttiense comb. nov., Curvibacter lanceolatus comb. nov., Curvibacter delicatus comb. nov. and Herbaspirillum autotrophicum comb. nov. *Int J Syst Evol Microbiol* **54**, 2223–2230 (2004).

282. Liu, C. *et al.* Septicemia Caused by Herbaspirillum huttiense Secondary to Pneumonia. *Ann Lab Med* **39**, 340–342 (2019).

283. Regunath, H., Kimball, J., Smith, L. P. & Salzer, W. Severe Community-Acquired Pneumonia with Bacteremia Caused by Herbaspirillum aquaticum or Herbaspirillum huttiense in an Immune-Competent Adult. *J Clin Microbiol* **53**, 3086–3088 (2015).

284. Li, X. *et al.* First Study of Bacteremia Caused by Herbaspirillum huttiense in China: A Brief Research Report and Literature Review. *Front Cell Infect Microbiol* **12**, 882827 (2022).

285. Ruiz de Villa, A., Alok, A., Oyetoran, A. E. & Fabara, S. P. Septic Shock and Bacteremia Secondary to Herbaspirillum huttiense: A Case Report and Review of Literature. *Cureus* **15**, (2023).

286. Johnson, A. P. & Duckworth, G. J. The emergence of Stenotrophomonas maltophilia. *BMJ* **336**, 1322 (2008).

287. Said, M. S., Tirthani, E. & Lesho, E. Stenotrophomonas Maltophilia. *StatPearls* (2024).

288. Nagpal, R. & Yadav, H. Bacterial Translocation from the Gut to the Distant Organs: An Overview. *Ann Nutr Metab* **71 Suppl 1**, 11–16 (2017).

289. Rajasekaran, S. *et al.* Does the gut microbiome influence disc health and disease? The interplay between dysbiosis, pathobionts, and disc inflammation: a pilot study. *Spine J* **24**, 1952–1963 (2024).

290. Choma, C. *et al.* Effect of temperature on growth characteristics of Bacillus cereus TZ415. *Int J Food Microbiol* **55**, 73–77 (2000).

291. Jabeen, I., Islam, S., Hassan, A. K. M. I., Tasnim, Z. & Shuvo, S. R. A brief insight into Citrobacter species - a growing threat to public health. *Frontiers in Antibiotics* **2**, 1276982 (2023).

292. Reimer, L. C. *et al.* BacDive in 2022: the knowledge base for standardized bacterial and archaeal data. *Nucleic Acids Res* **50**, D741–D746 (2022).

293. Berg, G. & Martinez, J. L. Friends or foes: Can we make a distinction between beneficial and harmful strains of the Stenotrophomonas maltophilia complex? *Front Microbiol* **6**, 120479 (2015).

294. Bressuire-Isoard, C., Broussolle, V. & Carlin, F. Sporulation environment influences spore properties in Bacillus: evidence and insights on underlying molecular and physiological mechanisms. *FEMS Microbiol Rev* **42**, 614–626 (2018).

295. Plotz, P. H. & Davis, B. D. Synergism between streptomycin and penicillin: a proposed mechanism. *Science* **135**, 1067–1068 (1962).

296. Smith, C. J. & Osborn, A. M. Advantages and limitations of quantitative PCR (Q-PCR)-based approaches in microbial ecology. *FEMS Microbiol Ecol* **67**, 6–20 (2009).

297. Jian, C., Luukkonen, P., Yki-Järvinen, H., Salonen, A. & Korpela, K. Quantitative PCR provides a simple and accessible method for quantitative microbiota profiling. *PLoS One* **15**, e0227285 (2020).

298. Fournier, D. E., Kiser, P. K., Shoemaker, J. K., Battié, M. C. & Séguin, C. A. Vascularization of the human intervertebral disc: A scoping review. *JOR Spine* **3**, (2020).

299. Aagaard, K. *et al.* The placenta harbors a unique microbiome. *Sci Transl Med* **6**, (2014).

300. Bokulich, N. A. *et al.* Antibiotics, birth mode, and diet shape microbiome maturation during early life. *Sci Transl Med* **8**, (2016).

301. Korpela, K. *et al.* Selective maternal seeding and environment shape the human gut microbiome. *Genome Res* **28**, 561–568 (2018).

302. Palmer, D. J., Metcalfe, J. & Prescott, S. L. Preventing disease in the 21st century: the importance of maternal and early infant diet and nutrition. *J Allergy Clin Immunol* **130**, 733–734 (2012).

303. Rothschild, D. *et al.* Environment dominates over host genetics in shaping human gut microbiota. *Nature 2018 555:7695* **555**, 210–215 (2018).

304. Boer, C. G. *et al.* Intestinal microbiome composition and its relation to joint pain and inflammation. *Nature Communications 2019 10:1* **10**, 1–9 (2019).

305. Dunalska, A., Saramak, K. & Szejko, N. The Role of Gut Microbiome in the Pathogenesis of Multiple Sclerosis and Related Disorders. *Cells* **12**, (2023).

306. Li, W. *et al.* Gut-disc axis: A cause of intervertebral disc degeneration and low back pain? *European Spine Journal* vol. 31 917–925 Preprint at https://doi.org/10.1007/s00586-022-07152-8 (2022).

307. Saukkonen, J. *et al.* Association Between Modic Changes and Low Back Pain in Middle Age: A Northern Finland Birth Cohort Study. *Spine (Phila Pa 1976)* **45**, 1360–1367 (2020).

308. Mera, Y. *et al.* Association between types of Modic changes in the lumbar region and low back pain in a large cohort: the Wakayama spine study. *Eur Spine J* **30**, 1011–1017 (2021).

309. Mertimo, T. *et al.* Association of lumbar disc degeneration with low back pain in middle age in the Northern Finland Birth Cohort 1966. *BMC Musculoskelet Disord* **23**, (2022).

310. Luoma, K., Vehmas, T., Kerttula, L., Grönblad, M. & Rinne, E. Chronic low back pain in relation to Modic changes, bony endplate lesions, and disc degeneration in a prospective MRI study. *Eur Spine J* **25**, 2873–2881 (2016).

311. Dudli, S., Fields, A. J., Samartzis, D., Karppinen, J. & Lotz, J. C. *Pathobiology of Modic Changes*. *European spine journal : official publication of the European Spine Society, the European Spinal Deformity Society, and the European Section of the Cervical Spine Research Society* vol. 25 3723–3734 (Eur Spine J, 2016).

312. Magnitsky, S. *et al.* Quantification of Propionic Acid in the Bovine Spinal Disk After Infection of the Tissue With Propionibacteria acnes Bacteria. *Spine (Phila Pa 1976)* **43**, E634–E638 (2018).

313. Albert, H. B. *et al.* Does nuclear tissue infected with bacteria following disc herniations lead to Modic changes in the adjacent vertebrae? *European Spine Journal* **22**, 690–696 (2013).

314. Heggli, I. *et al.* Low back pain patients with Modic type 1 changes exhibit distinct bacterial and non-bacterial subtypes. **6**, 100434 (2024).

315. da Rocha, V. M. *et al.* Would Cutibacterium acnes Be the Villain for the Chronicity of Low Back Pain in Degenerative Disc Disease? Preliminary Results of an Analytical Cohort. *J Pers Med* **13**, (2023).

316. Capoor, M. N. *et al.* Pro-Inflammatory and Neurotrophic Factor Responses of Cells Derived from Degenerative Human Intervertebral Discs to the Opportunistic Pathogen Cutibacterium acnes. *Int J Mol Sci* **22**, 1–16 (2021).

317. Marion, J. Pattern Recognition Receptors: Evolution, Redundancy, and Cross Talk. *Molecular Life Sciences* 1–7 (2014) doi:10.1007/978-1-4614-6436-5_369-1.

318. Mannarino, M. *et al.* Toll-like receptor 2 induced senescence in intervertebral disc cells of patients with back pain can be attenuated by o-vanillin. *Arthritis Res Ther* **23**, 1–14 (2021).

319. Herger, N. *et al.* Should Degenerated Intervertebral Discs of Patients with Modic Type 1 Changes Be Treated with Mesenchymal Stem Cells? *International Journal of Molecular Sciences* vol. 23 Preprint at https://doi.org/10.3390/ijms23052721 (2022).

320. Dahiya, D. & Nigam, P. S. Antibiotic-Therapy-Induced Gut Dysbiosis Affecting Gut Microbiota-Brain Axis and Cognition: Restoration by Intake of Probiotics and Synbiotics. *Int J Mol Sci* **24**, (2023).

321. Lee, C. J., Sears, C. L. & Maruthur, N. Gut microbiome and its role in obesity and insulin resistance. *Ann N Y Acad Sci* **1461**, 37–52 (2020).

322. Lazar, V. *et al.* Gut microbiota, host organism, and diet trialogue in diabetes and obesity. *Front Nutr* **6**, 341830 (2019).

323. Sikalidis, A. K. & Maykish, A. The Gut Microbiome and Type 2 Diabetes Mellitus: Discussing A Complex Relationship. *Biomedicines 2020, Vol. 8, Page 8* **8**, 8 (2020).

SECTION 7 APPENDIX

APPENDIX

Appendix 1 | Survey

P1
What institution are you from?
University of Bern
University of Sheffield
Icahn School of Medicine at Mount Sinai
University of Sheffield
University of Arizona College of Medicine
The University of Sheffield
P2
What is your highest degree?
Postgraduate degree
Doctoral degree
Undergraduate degree
Doctoral degree
Undergraduate degree
Doctoral degree
P3
What is your role in the institution?
PhD Student
Professor/PI
Other please state:
PostDoc
Other please state:
PostDoc
P4
How familiar are you with immunohistochemical analysis?
Moderately familiar
Extremely familiar
Slightly familiar
Moderately familiar
Slightly familiar
Extremely familiar

P5
Have you ever used QuPath previously?
Never
Never
Never
Sometimes
Never
Never
GB1_4
Please rate your experience with the QuPath H-DAB tutorial provided. - I frequently use QuPath and know the platform
9
5
9
4
GB1_1
Please rate your experience with the QuPath H-DAB tutorial provided. - The installation process of QuPath was clear
10
9
7
8
10
9
GB1_2
Please rate your experience with the QuPath H-DAB tutorial provided. - The QuPath tutorial was clear and easy to follow.
10
9
8
10
8
7
GB1_3
Please rate your experience with the QuPath H-DAB tutorial provided. - No additional QuPath instruction was necessary
8
7
3
10
6
8

GB1.1
What was unclear about the installation?
Some steps were difficult to translate from windows to mac.
GB1.3
What else would have been needed?
Mac-specific instructions would have been great!
Maybe instructions for mac vs. PC
GB2_1
Please rate your experience with the QuPath H-DAB script - It was clear how to open the Script editor
10
10
9
10
10
8
GB2_2
Please rate your experience with the QuPath H-DAB script - The downloading and copying of the script was clear
10
9
8
10
10
7
GB2_3
Please rate your experience with the QuPath H-DAB script - It was clear which lines in the script needed replacing
10
9
9
10
10
7
GB2.2
What was unclear?
How to change some of the scripts and how to use them
GB2.3
What else would you have needed?
Clearer instructions on how to use them

GB3_5
Please rate your experience with GitBash and Python - I frequently use python and GitBash and know the platform
5
1
1
1
2
GB3_1
Please rate your experience with GitBash and Python - Installation of GitBash was clear
10
10
3
3
7
10
GB3_2
Please rate your experience with GitBash and Python - Installation of Python was clear
7
10
3
10
3
10
GB3_3
Please rate your experience with GitBash and Python - The information given was sufficiant to run the provided code
10
10
7
10
8
7
GB3_4
Please rate your experience with GitBash and Python - I did not have any issues running the code
8
8
7
8
6
6

GB3.1.2
What was unclear?
1)During Cell Classifier step it took me a bit to realise how to choose NoCell/PositiveCell/NegativeCell option while I was classifying 2) I missed the info of installing certain Python packages
Like previous steps, mac-specific instructions would have been great.
GB3.4
What was the error message?
Most issues were regarding the installation process, not running the script within QuPath
E1
What kind of tissue did you use for the analysis?
Human IVD tissue
IVD & Cartilage
Rat spine
Osteochondral tissue
IVD
Intervertebral disc
Q35
How many slides have you analysed
20-30
50+
20-30
20-30
20-30
E3
How satisfied were you with the detection and classification of the script?
Extremely satisfied
Extremely satisfied
Extremely satisfied
Extremely satisfied
Extremely satisfied
Somewhat satisfied

Batch Y N
Did you perform the analysis on the provided training batch?
Yes
Yes
No
Yes
Yes
No
E3.1
Does anything need to be improved regarding the detection and classification of the script?
No :)
no
No
E4
Will you use the QuPath script and analysis package in the future?
Definitely yes
Definitely yes
Probably yes
Definitely yes
Definitely yes
Probably yes
E5
Will you recommend the QuPath script and analysis package to a friend or colleague?
Definitely yes
Definitely yes
Definitely yes
Definitely yes
Definitely yes
Definitely yes
Q36
Do you have any furhter suggestions or comments?
Further is spelt incorrectly on this question.
None, thank you!
No
No, thank you!
Make instructions slightly clearer for each step and how to put the correct codes into Git Bash

Appendix 2 | Donors used for immunohistochemical staining

HD	Age	Sex	Deg. Score	MC	Diagnosis	Disc Level	Reason for surgery	Operation Title	Previous Surgery	Intact
2	42	Female	5.5			L5/S1	Root Pain			Attenuated Annulus but Intact
4	50	Female	5	0	Disc Protrusion	L4/L5	Root Pain			Annular Bulge
5	33	Female	7	2	Disc Prolapse	L5/S1	Root Pain			Attenuated Annulus but Intact
8	70	Female	7	1	Disc Protrusion	L4/L5	Root Pain	Microdisectomy		Attenuated Annulus but Intact
9	32	Male			Radiculopathy	L5/S1	Root Pain	Right S1 Nerve root decompression and		
12	40	Female		0	Disc Protrusion	L5/S1	Root Pain	Microdisectomy	Yes	Annular Bulge
15	34	Female	5	2	Disc Protrusion	L4/L5	Root Pain	Disc Protrustion	Yes	Annular Bulge
21	25	Female		2	Disc Protrusion	L4/L5	Root Pain	Microdisectomy		Attenuated Annulus but Intact
22	23	Male		0	Disc Prolapse	L4/L5	Root Pain	Microdisectomy		Annular Bulge
29	37	Male		1		L4/L5	Root Pain	L4/L5 Decompression and Discectomy	Yes	Annular Bulge
36	33	Female		2	Disc Protrusion	L5/S1	Cauda Equina Symptoms	Microdisectomy		Attenuated Annulus but Intact
37		Female			Post Mortem	L5/S1	other			Intact Post Morten

38		Female	9		Post Mortem	L4/5	other			Intact Post Morten
39		Female	5.5		Post Mortem	L3/4	other			Intact Post Morten
40		Female	5		Post Mortem	L2/3	other			Intact Post Morten
41		Female	3		Post Mortem	L1/2	other			Intact Post Morten
44	41	Male	4		Disc Protrusion	L5/S1	Root Pain	Microdisectomy		Attenuated Annulus but Intact
45	35	Female	5	1	Disc Protrusion	L5/S1	Root Pain	Microdisectomy		Annular Bulge
51	52	Female	5	1	Disc Protrusion	L4/L5	Root Pain	Microdisectomy	Yes	Annular Bulge
54	28	Female	2	1	Disc Protrusion	L4/L5	Root Pain	Microdisectomy		Annular Bulge
57	43	Female	4.5	0	Disc Protrusion	L5/S1	Root Pain	Microdisectomy		Annular Bulge
59	36	Male	4.5	0	Disc Protrusion	L5/S1	Root Pain	Microdisectomy		Annular Bulge
60	38	Female	6	2	Disc Protrusion	L5/S1	Root Pain	Microdisectomy		Annular Bulge
64	47	Male		0	L5/S1 Disc	L5/S1	Root Pain	Microdisectomy		
66	63	Male		2	Disc Prolapse	L3/L4	Myelopathy	Anterior Cervical Discectomy and Fusion		Annular Bulge
128	44	Male			Disc Prolapse	C5/C6	Root and Spinal Pain	Anterior Cervical Discectomy and Fusion	Yes	
166	33	Male		2	Disc Prolapse	L4/L5	Root and Spinal Pain	Microdisectomy		

173	30	Male		0	Disc Prolapse	L4/L5	Root Pain	Microdisectomy		Attenuated Annulus but Intact
175	37	Female	6	2	Radicular Pain	L5/S1	Root Pain	Microdisectomy		Attenuated Annulus but Intact
177	51	Male	7	2	Disc Prolapse	L4/L5	Root and Spinal Pain	Microdisectomy	Yes	
178	56	Male	5.5		Radicularpathy	C6/C7	Root Pain	Anterior Cervical Discectomy and Fusion		
184	49	Female	4	1	Disc Protrusion	L4/L5	Root Pain	Microdisectomy	Yes	
193	46	Male		0	Disc prolapse	L4/L5	Root and Spinal Pain	Microdisectomy		Attenuated Annulus but Intact
196	26	Male	3		Disc Prolapse	C5/6	Root Pain	Anterior Cervical Discectomy and Fusion		Attenuated Annulus but Intact
200	59	Female		2	Disc Protrusion	L5/S1	Root Pain	Disc Protrustion	Injection	Attenuated Annulus but Intact
203	45	Male		2	Radicular Pain	L5/S1	Root Pain	Microdisectomy		Attenuated Annulus but Intact
346	46	Male			radiculopathy and myelopathy	C5/6	other	Anterior Cervical Discectomy and Fusion		Attenuated Annulus but Intact
349	17	Female		0		L5/S1	Root Pain	Microdisectomy		Attenuated Annulus but Intact
370	50	Male	5		Disc Protrusion	L5/S1	Root Pain	Microdisectomy		Annular Bulge
371	53	Female		1	Spinal Stenosis	L3/L4	Root and Spinal Pain	Transforaminal lumbar Interbody Fusion		Attenuated Annulus but Intact
376	18	Female		0	Disc Protrusion	L5/S1	Root Pain	Microdisectomy		Annular Bulge
382	48	Male	3.5	2	Disc Protrusion	L5/S1	Root Pain	Microdisectomy	Yes	

386	77	Male								
391	44	Female	5	1	Radiculopathy	C5/6 C 6/7	Root Pain	Anterior Cervical Discectomy and Fusion		Attenuated Annulus but Intact
393		Female	4		Myelopathy	C4/5	other			
394	44	Female	6	0	Disc Protrusion	C6/7	Root Pain	Anterior Cervical Discectomy and Fusion	Yes	
398	73	Female	4	1	Scoliosis	L2/3	Root Pain	Anterior release L2/3	Yes	
399	56	Male	4	0	Stenosis	L3/4	Root and Spinal Pain	Transforaminal lumbar Interbody Fusion	Yes	
400	52	Male	4.5	0	Radiculopathy	C6/7	Root Pain	Anterior Cervical Discectomy and Fusion		
402	53	Female	4	1,2	Root Stenosis	C4/5 C 5/6	Root Pain	Anterior Cervical Discectomy and Fusion	Yes	
404	49	Female		2	Radiculopathy	L5/S1	Root Pain	Microdisectomy		Annular Bulge
405	17	Female	4	0	Scoliosis	T11/12 -, L2/3	other	Anterior Scoliosis Correction		
409	40	Female	6		Radicular pain	L4/5	Root Pain	Microdisectomy		Attenuated Annulus but Intact
414	48	Female		1,2	Cervical Radiculopathy	C5/6 C 6/7	Root Pain	Anterior Cervical Discectomy and Fusion		Attenuated Annulus but Intact
423	22	Female	6.5	0	Scoliosis	T11/12 - L2/3	other	Anterior Scoliosis Correction		
426		Male	5	1,2	Radiculopathy	C5/6 C 6/7	Root Pain	Anterior Cervical Discectomy and Fusion		Attenuated Annulus but Intact
435	53	Female	4	0	Radiculopathy	C6/7	Root Pain	Anterior Cervical Discectomy and Fusion		

440		Female	4.5	2	Myelopathy	C4/5	other	Anterior Cervical Discectomy and Fusion		Attenuated Annulus but Intact
441	51	Female	8	0	Fusion	L4/5	Root and Spinal Pain	Transforaminal lumbar Interbody Fusion	Yes	Attenuated Annulus but Intact
444	73	Male	3		Spondylolisthesis	L2/3 L3/4 L4/5	Spinal Pain	Transforaminal lumbar Interbody Fusion		Attenuated Annulus but Intact
445	35	Female	7	2	Disc Prolapse	L5/S1	Root and Spinal Pain	Microdisectomy		
448	60	Male				C5/6 C6/7	Root Pain	Anterior Cervical Discectomy and Fusion		
455	53	Female	8		Disc Prolapse	L5/S1	Root and Spinal Pain	Microdisectomy		
461	50	Female			Disc Prolapse	L5/S1	Root and Spinal Pain	Microdisectomy	Yes	
462	34	Male	7		Disc Prolapse	L5/S1	Root and Spinal Pain	Microdisectomy	Yes	Attenuated Annulus but Intact
463	43	Male	4	2	Disc Prolapse	L4/5	Root and Spinal Pain	Microdisectomy		Attenuated Annulus but Intact
465	44	Male	5	2	Disc Prolapse	L5/S1	Spinal Pain	Microdisectomy		Annular Bulge
468	25	Male	6		Leg Pain	L5/S1	Root Pain	Microdisectomy		Attenuated Annulus but Intact
469	42	Female	4	2	Radicular Pain	L5/S1	Root Pain	Microdisectomy		Attenuated Annulus but Intact
470	43	Male		2		L4/L5	Root Pain	Microdisectomy		
472	25	Female	6	0	Cauda Equina Compression	L4/L5	Root Pain	Microdisectomy		Attenuated Annulus but Intact

473	44	Female		0	Right S1 Root Pai n	L5/S1	Root Pain	Microdisectomy		Annular Bulge
475	52	Male	5	2	Disc Prolapse	L4/5	Root Pain	Nerve Root Decompression		
477	51	Female	4	2	Cervical Radiculo pathy	C6/7	Root Pain	Anterior Cervical Discectomy and Fusion		Annular Bulge
482	43	Female	4	2	Radicular Pain	L5/S1	Root Pain	Microdisectomy		Attenuated Annulus but Intact
534	29	Male			Radicular Pain	L5/S1	Root Pain	Microdisectomy		Attenuated Annulus but Intact
536	66	Female	4	0	Stenosis	L4/5	Root and Spin al Pain	Posterior decompression		
551	29	Female	4	2	Disc Protrusion	L4/5	Root and Spin al Pain	Microdisectomy		Annular Bulge
575	32	Male		0	Pain	L5/S1	Root Pain	Microdisectomy		Annular Bulge
576	49	Male			Pain	L5/S1	Root Pain	Microdisectomy		Annular Bulge
577	72	Female	4	1		L3/4	Root Pain	Direct Lateral Interbody Fusion	Yes	
588	49	Male	6	2	Disc Prolapse	L5/S1	Root Pain	Microdisectomy	Yes	Attenuated Annulus but Intact
593	47	Female			Radicular Pain	L4/5	Root Pain	Microdisectomy		Attenuated Annulus but Intact
594	39	Female	5		Disc Prolapse	L5/S1	Root Pain	Microdisectomy		Attenuated Annulus but Intact
597	54	Female	8		Radiculopathy	L4/5	Root Pain	Microdisectomy		Attenuated Annulus but Intact

601	52	Male	9		Radiculopathy	C6/7	Root Pain	Anterior Cervical Discectomy and Fusion		Attenuated Annulus but Intact
615	44	Female	9		Disc Protrusion	L4/5	Root Pain	Microdisectomy		Attenuated Annulus but Intact

Appendix 3 | Donors for *in vitro* experiments

ID	Sex	Age	Diagnosis	Surgery	Disc Level	Nucleus intact/extrusion	Experiment
612	F	23	R S1 Pain	Microdisectomy	L5/S1	Attenuated annulus but intact	2D PGN/LPS
627	F			Microdisectomy		Extrusion of nucleus material from the annulus	2D PGN/LPS
636	F	77	Radiculopathy	Microdisectomy	L4/L5	Extrusion of nucleus material from the annulus	2D PGN/LPS
D645	F	40	Radiculopathy	Microdisectomy	L5/S1	Attenuated annulus but intact	3D PGN/LPS
648	M	49	Radiculopathy	Microdisectomy		Extrusion of nucleus material from the annulus	3D PGN/LPS
659	M		Cauda Equina Syndrome	Microdisectomy	L3/4	Extrusion of nucleus material from the annulus	3D PGN/LPS
735	M	29	Eadicular pain	Microdisectomy	L5/S1	Attenuated annulus but intact	Inhibition
743	M	49	Left L5 pain	Microdisectomy	L4/5	Extrusion of nucleus material from the annulus	Inhibition
746	F	48	Radiculopathy	Microdisectomy	L5/S1	Extrusion of nucleus material from the annulus	Inhibition

Appendix 4 | Bovine donor list

ID_Sample	Processing date	Collection Date	Days of Culture	Height [mm]	Diameter [mm]	A [mm^2]	Mass [kg]	Treatment	Media collected
BD322_1	*24/07/2023*	*27/07/2023*	*3*	9.755	15.945	199.58	**2.03**	static infected	x
BD322_2	*24/07/2023*	*27/07/2023*	*3*	11.82	18.28	262.31	**2.67**	static infected	x
BD322_3	*24/07/2023*	*27/07/2023*	*3*	13.755	21.69	369.31	**3.76**	static infected	
BD322_4	*24/07/2023*	*27/07/2023*	*3*	13.035	23.305	426.35	**4.35**	static infected	
BD323_1	*07/08/2023*	*10/08/2023*	*3*	13.76	20.355	325.25	**3.32**	static control	x
BD323_2	*07/08/2023*	*08/08/2023*	*1*	13.15	19.26	291.19	**2.97**	visible bacterial growth	x
BD323_3	*07/08/2023*	*09/08/2023*	*2*	12.735	17.25	233.59	**2.38**	visible bacterial growth	x
BD323_4	*07/08/2023*	*10/08/2023*	*3*	12.035	16.765	220.64	**2.25**	dynamic control	x
BD323_5	*07/08/2023*	*10/08/2023*	*3*	11.315	14.82	172.41	**1.76**	dynamic infected	x
BD323_6	*07/08/2023*	*10/08/2023*	*3*	10.435	14.12	156.51	**1.60**	static infected	x
BD326_1	*14/08/2023*	*15/08/2023*	*1*	11.8	14.2	158.29	**1.61**	visible bacterial growth	x
BD326_2	*14/08/2023*	*15/08/2023*	*1*	14.72	14.755	170.90	**1.74**	visible bacterial growth	x
BD326_3	*14/08/2023*	*15/08/2023*	*1*	13.34	15.785	195.60	**1.99**	visible bacterial growth	x
BD326_4	*14/08/2023*	*15/08/2023*	*1*	14.07	17.53	241.23	**2.46**	visible bacterial growth	x
BD326_5	*14/08/2023*	*15/08/2023*	*1*	15.2	17.8	248.72	**2.54**	visible bacterial growth	x
BD326_6	*14/08/2023*	*15/08/2023*	*1*	16.465	18.265	261.88	**2.67**	visible bacterial growth	x
BD326_7	*14/08/2023*	*14/08/2023*	*0*					*control*	
BD328_1	*21/08/2023*	*23/08/2023*	*2*	10.43	13.69	147.12	**1.50**	visible bacterial growth	x
BD328_2	*21/08/2023*	*23/08/2023*	*2*	13.685	15.095	178.87	**1.82**	visible bacterial growth	x
BD328_3	*21/08/2023*	*23/08/2023*	*2*	14.34	17.81	249.00	**2.54**	visible bacterial growth	x
BD328_4	*21/08/2023*	*23/08/2023*	*2*	15.81	19.06	285.18	**2.91**	visible bacterial growth	x
BD328_5	*21/08/2023*	*23/08/2023*	*2*	16.465	21.47	361.85	**3.69**	visible bacterial growth	x

BD328_6	*21/08/2023*	*21/08/2023*	*0*					*control*	
BD328_7	*21/08/2023*	*21/08/2023*	*0*					*control*	
BD329_1	*28/08/2023*	*31/08/2023*	*3*	10.85	14.575	166.76	**1.70**	dynamic control	x
BD329_2	*28/08/2023*	*31/08/2023*	*3*	10.14	16.165	205.13	**2.09**	dynamic infected	x
BD329_3	*28/08/2023*	*31/08/2023*	*3*	12.05	18.17	259.17	**2.64**	static infected	x
BD329_4	*28/08/2023*	*30/08/2023*	*2*	12.415	17.92	252.08	**2.57**	visible bacterial growth	x
BD329_5	*28/08/2023*	*31/08/2023*	*3*	11.725	19.15	287.88	**2.93**	static control	x
BD329_6	*28/08/2023*	*30/08/2023*	*2*	13.075	20.43	327.65	**3.34**	visible bacterial growth	x
BD329_7	*28/08/2023*	*28/08/2023*	*0*					*control*	
BD330_1	*04/09/2023*	*07/09/2023*	*3*	10.253	14.53	128.92	1.31	Static infected	x
BD330_2	*04/09/2023*	*05/09/2023*	*1*	11.135	15.88	197.96	**2.02**	visible bacterial growth	x
BD330_3	*04/09/2023*	*06/09/2023*	*2*	12.725	15.765	195.10	**1.99**	visible bacterial growth	x
BD330_4	*04/09/2023*	*07/09/2023*	*3*	13.255	18.95	281.90	**2.87**	dynamic control	x
BD330_5	*04/09/2023*	*07/09/2023*	*3*	14.63	17.735	246.91	**2.52**	dynamic infected	x
BD330_6	*04/09/2023*	*07/09/2023*	*3*	15.28	22.33	391.42	**3.99**	static control	x
BD330_7	*04/09/2023*	*04/09/2023*	*0*					*control*	
BD330_8	*04/09/2023*	*04/09/2023*	*0*					*control*	
BD331_1	*04/09/2023*	*05/09/2023*	*1*	11.12	12.995	132.56	**1.35**	visible bacterial growth	x
BD331_2	*04/09/2023*	*05/09/2023*	*1*	14.47	16.61	216.58	**2.21**	visible bacterial growth	x
BD331_3	*04/09/2023*	*05/09/2023*	*1*	15.14	18.885	279.96	**2.85**	visible bacterial growth	x
BD331_4	*04/09/2023*	*05/09/2023*	*1*	16.945	19.16	288.18	**2.94**	visible bacterial growth	x
BD331_5	*04/09/2023*	*05/09/2023*	*1*	15.72	19.27	291.50	**2.97**	visible bacterial growth	x
BD331_6	*04/09/2023*	*05/09/2023*	*1*	16.42	20.475	329.09	**3.35**	visible bacterial growth	x
BD331_7	*04/09/2023*	*04/09/2023*	*0*					*control*	

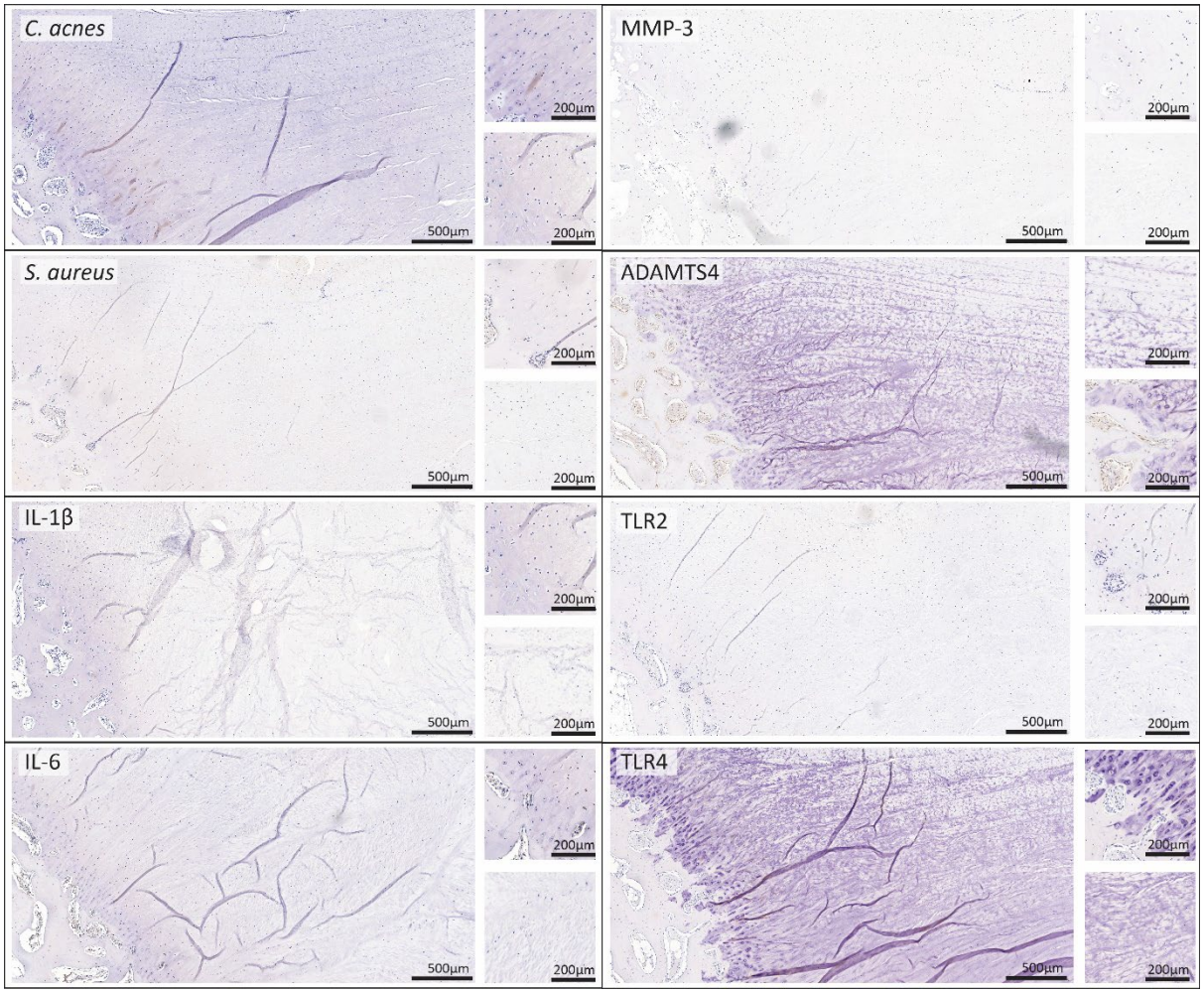

Appendix 5| IgG controls for immunohistochemical staining

IgG controls used to test unspecific binding do not show any brown staining, indicating specificity of the antibody to its target. Scalebars are 500 µm in the wide range pictures and 200 µm in the zoomed in squares.